Measurement of the Longitudinal Spin Asymmetry of the Deuteron in the Resonance Region

Kangkang Li Kovacs
Charlottesville, Virginia

B.S., Peking University, 2002
M.A., University of Virginia, 2010

A Dissertation presented to the Graduate Faculty
of the University of Virginia in Candidacy for the Degree of
Doctor of Philosophy

Department of Physics

University of Virginia
December, 2010

Table of Contents

Abstract

The first moment of the spin structure function g_1, Γ_1, goes through a rapid transition from the photon limit ($Q^2 = 0$) where it is constrained by the Gerasimov-Drell-Hearn(GDH) sum rule to the deep inelastic region. The "EG4" experiment at the Jefferson Lab (E-03-006) which took place in early 2006 was aimed to measure these observables and to calculate the GDH sum rule at low Q^2 in the resonance region.

The experiment used a longitudinally polarized electron beam and longitudinally polarized ND_3 and NH_3 ammonia targets. The CEBAF Large Acceptance Spectrometer (CLAS) was used to accumulate the scattering events. In this thesis, we present results for the virtual photon asymmetry $A_1(x)$ and will talk about future analysis on the longitudinal spin structure function for the deuteron $g_1^d(x, Q^2)$ as well as the first moment Γ_1^d. The extracted results complement the existing data for deuteron spin structure in the resonance region. These results are important in the study of Q^2 evolution of nucleon structure from the hadronic to partonic degrees of freedom.

Acknowledgements

First of all I thank my advisors Don Crabb and Donal Day for their guidance. I thank all the past and present members of the Polarized Target Group at the University of Virginia and the EG4 Experiment Group at Jefferson Lab. I thank Karl Slifer at the University of New Hampshire for dedicating his time helping me with software programming problems. I thank Peter Bosted and Sebastian Kuhn for providing resource of analysis programs. Finally, I thank my parents Shaohua Li, Cuiying Wang who live all the way in China and my husband Mark Kovacs, who has been by my side the entire time, for their unfaltering support, which kept me motivated and fulfilled throughout my PhD years.

Introduction

One of the first experiments to probe the hadronic structure of the proton and deuterium targets were carried out at the Stanford Linear Accelerator Center (SLAC) in the 1960s, in which high energy electrons were scattered, at large momentum transfer and large energy loss(Deep Inelastic Scattering (DIS)), from protons. This observation suggested that the proton consisted of discrete scattering centers. Later experiments at SLAC and CERN confirmed these observation, and it became widely accepted that the proton and neutron are not elementary but are made of 'partons' [1]. The partons were classified in two types: electrically neutral massless vector particles with spin 1, called gluons, and spin $\frac{1}{2}$ fractionally charged fermions called quarks. There are six known flavors of quarks, which are listed in Table 1, with their

	Q	T	T_3	S
u	2/3	1/2	1/2	0
d	-1/3	1/2	-1/2	0
s	-1/3	0	0	-1
c	2/3	0	0	0
s	2/3	0	0	0
s	-1/3	0	0	0

Table 1: Quark Quantum Numbers

electrical charges, Q, strangeness quantum number, S, and isospin (T, T_3) [1].

The three light quarks u,d and s are identified with the three states in the fundamental representation of the flavor SU(3). hadrons are constructed as flavor SU(3) states and the total symmetry group of the Hadrons is SU(3)$\times$ SU(2) when the spin of the quarks is taken into account.

When the momentum scale changes, what appeared to be a quark reveals an additional quark-antiquark pair. Quantum Chromodynamics (QCD) is a theory that predicts such evolution with Q^2, momentum transfer squared. As nucleon structure is resolved to smaller and smaller distances, more partons are revealed, each with a progressively smaller fraction of initial quark momentum.

The interactions between quarks and antiquarks are mediated by gluons. The gluons as well as quarks and antiquarks carry a color charge. The three types of color charge are called red R, blue B and green G, with the corresponding anticolors $\overline{R}$, $\overline{B}$. $\overline{G}$. The color is not observable, and all colors appear with equal probability. Only 'colorless' quark systems are observed in nature. Color confinement is one of the key features of QCD. It can be explained by the increasing of the color force with the increasing separation. As the separation decreases, the force becomes weaker, so that at very small distances (large momenta), the quarks no longer interact with each other. This phenomenon is called asymptotic freedom.

The strong coupling is defined as a power series. Its first order approximation can be written as:

$$\alpha_s(Q^2) = \frac{12\pi}{33 - 2n_f} \frac{1}{ln(Q^2/\Lambda^2)} \tag{0.0.1}$$

where n_f is the number of active quark flavors, Q^2 is the absolute value of the four momentum squared, and the parameter Λ is determined experimentally.

Lepton-nucleon scattering is a well known method used to probe the nucleons' structure. During the scattering, the electron emits a virtual photon which is absorbed by the nucleon. High energy photons can be absorbed in a process known as the Deep Inelastic Scattering (DIS), while the relatively low energy photons probe the excited states of the nucleon. Richard Feynman in 1969 proposed the parton model [1, 2], as a way to analyze high-energy hadron collisions. Later, with the experimental observation of Bjorken scaling, the validation of the quark model, and the confirmation of asymptotic freedom in quantum chromodynamics, partons were matched to quarks and gluons. The Naive Parton Model (NPM) predicted that 100% of the nucleon spin is carried by the quarks [1].

The spin-dependent structure functions, g_1 and g_2, contain information on the spin carried by the quarks in the nucleon. During the last two decades much progress has been made in polarized beam and target technologies, thus making it possible to experimentally measure these structure variables of the nucleon. In the leading order QCD, using the SU(3) flavor decomposition, the first moment of the spin related structure function of proton, g_1^p, is expressed as

$$\Gamma_1^p = \int_0^1 g_1^p(x)\,dx = \frac{1}{12}[a_3 + \frac{1}{3}a_8 + \frac{4}{3}a_0] \tag{0.0.2}$$

where a_0, a_3 and a_8 are the nucleon axial charges.

Several sum rules predict the value of this integral, in particular, the Ellis-Jaffe sum rule [3]. The Ellis-Jaffe sum rule gives the following numeric prediction for the value of the proton and neutron integrals:

$$\Gamma_1^p = \int_0^1 g_1^p(x)\,dx = \frac{3}{36}a_3 + \frac{1}{36}a_8 + \frac{4}{36}a_0 = 0.186 \pm 0.004, \tag{0.0.3}$$

$$\Gamma_1^n = \int_0^1 g_1^n(x)\,dx = -\frac{3}{36}a_3 + \frac{1}{36}a_8 + \frac{4}{36}a_0 = -0.025 \pm 0.004, \tag{0.0.4}$$

Experiments dedicated to measurements of g_1 have been carried out for more than 3 decades. The Ellis-Jaffe sum rule has been shown to be strongly violated. The first result was obtained by the European Muon Collaboration (EMC) in 1988 [4, 5]. Γ_1^p was found to be much smaller than the predicted value according to the Ellis-Jaffe sum rule. This result had interesting implications for the composition of the proton spin. Contrary to the NPM predictions [2], the EMC results showed that only $12 \pm 17\%$ [5] of the proton spin is carried by quarks, and that the strange quark sea was probably polarized.

The Bjorken sum rule [6] is considered a fundamental sum rule based only on current algebra as well as predicting QCD. The Bjorken sum rule predicts the difference between the proton and neutron first moments:

$$\Gamma_1^p - \Gamma_1^n = \frac{1}{6}[\triangle\mu - \triangle d] = \frac{1}{6}\frac{g_A}{g_V} \tag{0.0.5}$$

where g_A and g_V are the axial and vector weak coupling constants of the nucleon beta decay.

The Bjoken sum rule proved to be a crucial test of QCD. Existing results at the deep inelastic region has verified the Bjorken sum rule and suggest that only about $31 \pm 10\%$ of the nucleon spin is carried by the quarks, the rest of the spin must reside either in gluons or in the orbital angular momentum of its constituents.

At the real photon point($Q^2 = 0$), the Gerasimov-Drell-Hearn(GDH) sum rule [7] relates the difference of total cross section of the polarized photons on polarized nucleons with the anomalous magnetic moment of the nucleon κ:

$$-\frac{\kappa^2}{4} = \frac{M}{8\pi^2\alpha}\int_{\nu_{th}}^{\infty}\frac{\sigma_T^{1/2} - \sigma_T^{3/2}}{\nu}\,d\nu \tag{0.0.6}$$

where ν_{th} is the one pion production threshold. The GDH sum rule is derived in the real photon limit. Assuming that the cross section of the real photon connects smoothly with the cross section of the virtual photon, the GDH sum rule can be generalized for $Q^2 \to 0$ and used to predict the first moment of the spin-related structure function Γ_1:

$$\begin{aligned} &Q^2 \to 0 : \\ &\Gamma_1 \Rightarrow -\frac{Q^2\kappa^2}{8M^2} \end{aligned} \tag{0.0.7}$$

We can conclude from this equation that Γ_1 approaches zero with a negative slope. Since it is positive at the large Q^2 range, Γ_1 should rapidly change sign somewhere in the resonance region $0 < Q^2 < 1GeV$.

The EG4 experiment took place at the Jefferson Lab in early 2006. Its purpose was to measure the helicity-dependent inclusive cross section difference and calculate the first moment of g_1 and determine the generalized GDH sum rule at low Q^2. During the experiment, longitudinally polarized electrons were scattered from polarized proton and deuteron targets at $Q^2 = 0.001 \sim 0.5GeV^2$ over a large W range. The modified CLAS detector was used to detect the scattered electrons. In this thesis, I will present an analysis of the data and a calculation of the longitudinal spin asymmetry for the deuteron A_1^d and compare the result to existing model. The extracted asymmetry at this point is still preliminary, and we have adopted a simplified error analysis.

Chapter 1

Physics overview

1.1 Inclusive Lepton Hadron Scattering

In order to probe the internal structure of the hadrons, a small, penetrating particle is used. Leptons proved to be ideal in such a case. The EG4 experiment at the Jefferson Lab used polarized electron beams to scatter from polarized proton and deuteron targets. The main process of the collision is shown by Figure 1.1.

An incident electron scatters inelastically off a nucleon (in this case, a proton or a deuteron) target. X is the system of hadrons produced through the inelastic scattering. The analysis in this thesis is an inclusive analysis, which means that the X hadron states are not observed. Only the electron momentum is measured in the final states.

During the inelastic scattering, the incoming electron emits a virtual photon of energy ν, momentum q, which is absorbed by the hadron target. Table 1.1 lists the basic kinematic variables for this procedure.

For a given X state, the scattering amplitude is defined as:

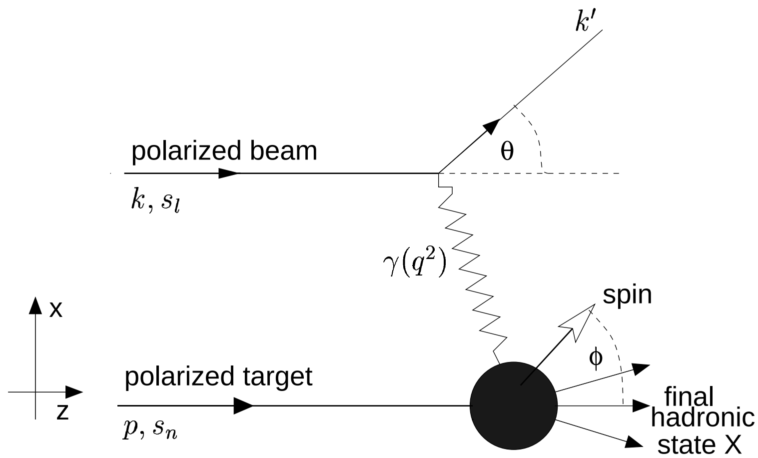

Figure 1.1: Inclusive Inelastic Scattering. k and k' are incoming and outgoing beam direction. θ is the scattering angle, q^2 represents the virtual photon momentum squared. In our case of inclusive analysis, ϕ of the particle of the final states is not analyzed.

Variable	expression	definition
M		mass of the proton
m		mass of the electron
k	(E, k_x, k_y, k_z)	incoming e 4-momentum
k'	(E', k'_x, k'_y, k'_z)	outgoing e 4-momentum
p	(M,0,0,0)	nucleon 4-momentum
q	(ν, q_x, q_y, q_z)	virtual photon 4-momentum
$Q^2 = -q^2$	$2EE'(1 - \cos\theta) = 4EE' \sin^2(\theta/2)$	4-momentum squared
ν	$E - E' = \frac{pq}{M}$	energy of the virtual photon
θ		scattering angle of e^- in the LAB frame
W^2	$(p + q)^2 = M^2 + 2pq + q^2$	Mass of the final hadronic state
x	$\frac{Q^2}{2M\nu}$	Bjorken dimensionless variable

Table 1.1: Kinematic Variables for Inclusive Inelastic Scattering

$$iM = (-ie)^2(\frac{-ig_{\mu\nu}}{q^2}) < k', s'_l|j_l^\mu(0)|k, s_l >< Xs'_X|j_h^\nu(0)|p, s_n > \tag{1.1.1}$$

where j_l^μ and j_h^ν are the electron and hadronic electromagnetic currents, s_l and s'_l are the polarization of the incoming and outgoing electron and s_n and $s'X$ are the polarization of the initial and final hadron target. This can be chosen to be parallel or anti-parallel to the incoming electron beam, yielding a value of $\pm\frac{1}{2}$.

Squaring the scattering amplitude M and multiplying it with phase space factor gives us the double differential cross section, $\frac{d^2\sigma}{d\Omega dE'} = \frac{\alpha^2}{2Mq^4}\frac{E'}{E}L_{\mu\nu}W^{\mu\nu}$, for detecting the outgoing electron in the solid angle $d\Omega$ [8]:

$$\frac{d^2\sigma}{d\Omega dE'} = \frac{\alpha^2}{2Mq^4}\frac{E'}{E}L_{\mu\nu}W^{\mu\nu} \tag{1.1.2}$$

In this equation, α is the fine structure constant characterizing the strength of electromagnetic interaction, its value being $\frac{1}{137}$ (approximately 7.297×10^{-3}), and $L_{\mu\nu}$ and $W^{\mu\nu}$ are respectively the leptonic and hadronic tensor which describe the emission and absorption of the virtual photon.

For a point-like fermion, using properties of the γ matrices the leptonic tensor can be written as:

$$L^{\mu\nu} = 2[(k'^\mu k^\nu + k'^\nu k^\mu) - (k \cdot k')g^{\mu\nu} - i\epsilon^{\mu\nu\rho\sigma}q_\rho s_l^\sigma] \tag{1.1.3}$$

where $g^{\mu\nu} = (1, -1, -1, -1)$ is the metric tensor, $\epsilon^{\mu\nu\rho\sigma}$ is the Levi-Civita's antisymmetric tensor and s_l^σ is the spin 4-vector of the incident electron. This tensor can be separated into two parts: the symmetric (sm) part and antisymmetric (asm) part:

$$L_{sm}^{\mu\nu} = (k'^\mu k^\nu + k'^\nu k^\mu) - (k \cdot k')g^{\mu\nu} \tag{1.1.4}$$

$$L_{asm}^{\mu\nu} = \epsilon^{\mu\nu\rho\sigma} q_\rho s_l^\sigma \tag{1.1.5}$$

Similarly, the hadronic tensor $W_{\mu\nu}$ can be split into symmetric and antisymmetric parts[8]:

$$W_{\mu\nu}(q,p,s) = W_{\mu\nu}^{sm}(q,p,s) + iW_{\mu\nu}^{asm}(q,p,s) \tag{1.1.6}$$

where

$$\frac{1}{2M} W_{\mu\nu}^{sm}(q,p) = (-g_{\mu\nu} + \frac{q_\mu q_\nu}{q^2}) W_1(p\cdot q, q^2) + [(p_\mu - \frac{p\cdot q}{q^2})(p_\nu - \frac{p\cdot q}{q^2} q_\nu)] \frac{W_2(p\cdot q, q^2)}{M^2} \tag{1.1.7}$$

$$\frac{1}{2M} W_{\mu\nu}^{asm}(q,p,s) = \epsilon_{\mu\nu\alpha\beta}[M s^\beta G_1(p\cdot q, q^2) + ((p\cdot q)s^\beta - (s\cdot q)p^\beta) \frac{G_2(p\cdot q, q^2)}{M}] \tag{1.1.8}$$

Here, the coefficients W_1, W_2 are the unpolarized structure functions and G_1, G_2 are the polarized structure functions.

If we want to extract information about the target spin, both the electron beam and the nucleon target need to be polarized. The contraction of $L_{sm}^{\mu\nu}$ and $W_{\mu\nu}^{sm}$ gives the spin independent cross section:

$$\frac{d^2\sigma}{d\Omega dE'} = \frac{4\alpha^2 E'}{Q^4} [\cos^2 \frac{\theta}{2} W_2 + 2\sin^2 \frac{\theta}{2} W_1] \tag{1.1.9}$$

The contraction of $L_{asm}^{\mu\nu}$ and $W_{\mu\nu}^{asm}$, as well as the difference of both cross sections where electrons and hadron targets are polarized parallel ($\sigma^{\uparrow\uparrow}$) or anti-parallel ($\sigma^{\uparrow\downarrow}$) gives the spin dependent cross section:

$$\frac{d^2\triangle\sigma}{d\Omega dE'} = \frac{d^2\sigma\uparrow\downarrow}{d\Omega dE'} - \frac{d^2\sigma\uparrow\downarrow}{d\Omega dE'} \tag{1.1.10}$$

$$\frac{d^2\triangle\sigma}{d\Omega dE'} = \frac{4\alpha^2 E'}{Q^2 E}[MG_1(E + E'\cos\theta) - Q^2 G_2] \tag{1.1.11}$$

According to Bjorken, in DIS scattering defined by large ν and Q^2 but $\frac{Q^2}{\nu}$ finite, the structure functions would only depend on the ratio $\frac{Q^2}{\nu}$ or the so defined Bjorken variable $x = \frac{Q^2}{2M\nu}$ [8]. In the Bjorken limit, the structure functions can be redefined as:

$$\begin{aligned} F_1(x) &= MW_1(\nu, Q^2) \\ F_2(x) &= \nu W_2(\nu, Q^2) \\ g_1(x) &= M^2\nu G_1(\nu, Q^2) \\ g_2(x) &= M\nu^2 G_2(\nu, Q^2) \end{aligned} \tag{1.1.12}$$

Now the longitudinally and transversely polarized cross section differences can be expressed in terms of these variables as functions of x and Q^2:

$$\frac{d^2\sigma^{\uparrow\downarrow} - d^2\sigma^{\uparrow\uparrow}}{d\Omega dE'} = \frac{4\alpha^2 E'}{Q^2 M E\nu}[(E + E'\cos\theta)g_1(x, Q^2) - 2xMg_2(x, Q^2)] \tag{1.1.13}$$

$$\frac{d^2\sigma^{\uparrow\leftharpoondown} - d^2\sigma^{\downarrow\rightharpoonup}}{d\Omega dE'} = \frac{4\alpha^2 E'^2}{Q^2 M E\nu}\sin\theta[g_1(x, Q^2) + \frac{4xME}{Q^2}g_2(x, Q^2)] \tag{1.1.14}$$

Later on in this thesis, longitudinal and transverse scattering asymmetries will be constructed from these cross sections:

$$A_{\parallel} = \frac{d^2\sigma^{\upharpoonleft\downharpoonright} - d^2\sigma^{\upharpoonleft\upharpoonright}}{d^2\sigma^{\upharpoonleft\downharpoonright} + d^2\sigma^{\upharpoonleft\upharpoonright}} \tag{1.1.15}$$

$$A_{\perp} = \frac{d^2\sigma^{\upharpoonleft\leftharpoonup} - d^2\sigma^{\downharpoonleft\rightharpoonup}}{d^2\sigma^{\upharpoonleft\leftharpoonup} + d^2\sigma^{\downharpoonleft\rightharpoonup}} \tag{1.1.16}$$

1.2 Spin Structure Functions g_1

The structure of the hadron we observe, by probing it with leptons, depends on the Q^2 of the virtual photon. In the deep inelastic scattering (DIS) region, Q^2 is very large, thus according to the uncertainty principle, the probing distance is very small and parton structure can be readily observed.

The naive parton model interprets the structure functions based on the asymptotic assumption. As $Q^2 \to \infty$, the effective coupling constant for the strong interaction $\alpha_s \to 0$. This is called the asymptotic freedom, where quarks do not interact with each other, they behave like free particles.

At Q^2 very large but not approaching infinity, α_s can no longer be treated as zero. The theory of Quantum Chromo Dynamics (QCD) can be taken perturbatively in this region.

In the parton model frame, the nucleon has a finite momentum. As Figure 1.2 illustrates, in the assumption of asymptotic freedom, the partons (quarks and gluons) each carry of a fraction x of the nucleon 4-momentum and travels in the same direction of the parent hadron. In this perspective, the lepton-hadron cross section can be

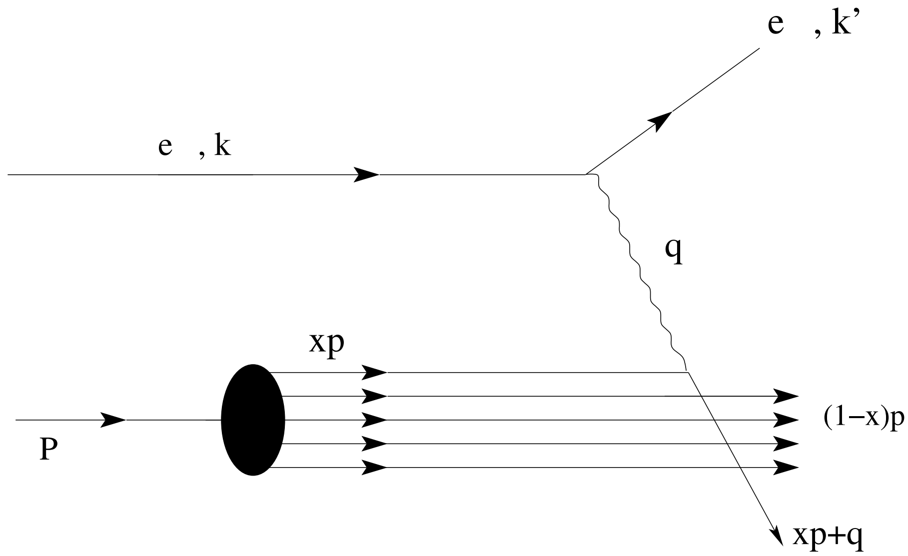

Figure 1.2: Parton Model in the DIS Region

viewed as the sum of all the lepton-parton cross sections. Under the parton model, the structure functions F_1, F_2 and g_1, g_2 can be expressed in term of the parton distribution functions $q_i(x)$, which gives the probability of finding a quark of flavor i that carries the momentum fraction x, charge e_i and spin.

$$\begin{aligned} F_1(x) &= \frac{1}{2}\sum_i e_i^2 q_i(x) \\ F_2(x) = x\sum_i e_i^2 q_i(x) &= 2xF_1(x) \\ g_1(x) &= \frac{1}{2}\sum_i e_i^2 \triangle q_i(x) \\ g_2(x) &= 0 \end{aligned} \tag{1.2.1}$$

where $\triangle q_i = q_i^{\uparrow\uparrow} - q_i^{\uparrow\downarrow}$, $q_i^{\uparrow\uparrow}$ is the distribution function with parton helicity parallel with that of the nucleon and $q_i^{\uparrow\downarrow}$ is the distribution function with parton helicity anti-parallel with that of the nucleon.

According to the parton model, the structure functions are independent of Q^2, they are only functions of x, the momentum fraction a parton carries of the parent hadron. However, structure functions have shown a significant Q^2 dependence during various experiments done in the past. Figure 1.3 shows the Q^2 dependence of g_1^p for different x.

At finite Q^2, the asymptotic freedom is no longer valid and the Bjorken limit is broken, the parton distribution function starts to show a slow logarithmic dependence on Q^2. Perturbative QCD theory can be used to compute these higher order QCD terms.

The gluons participate in the following transitions:

$$\begin{aligned} q &\rightarrow q + g \\ g &\rightarrow q + \bar{q} \\ \bar{q} &\rightarrow \bar{q} + g \\ g &\rightarrow g + g \end{aligned} \tag{1.2.2}$$

As Q^2 increases, more partons generate, which results in reduced value of the parton distribution function, $q_i(x)$. Each of these partons carries a momentum that is a fraction ξ' smaller than the original momentum, ξ. The evolution of the distribution functions can be formally described by the Altarelli-Parisi equations [12]. Due to the gluon emission, the results show a logarithmic Q^2 dependence of parton distribution

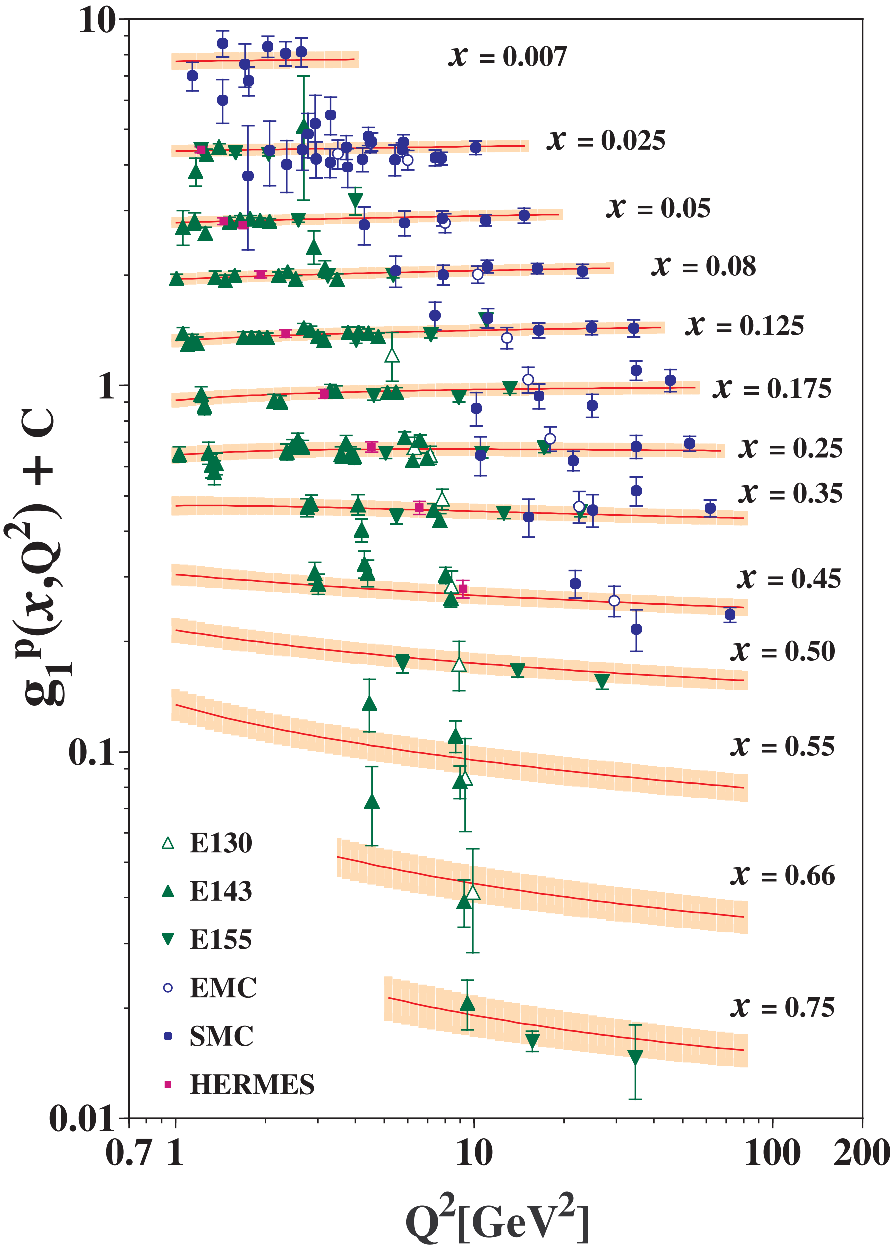

Figure 1.3: Q^2 dependence of the proton structure function g_1 at different x region. The data were collected from the different experiments as shown in the plot [9], [10], [11], [5].

functions.

$$\frac{dq_i(x,Q^2)}{dlnQ^2} = \frac{\alpha_s(Q^2)}{2\pi}\int_z^1 \frac{dy}{y}[P_{qq}(\frac{x}{y})q_i(y,Q^2) + P_{qg}(\frac{x}{y})g(y,Q^2)] \tag{1.2.3}$$

$$\frac{dg_(x,Q^2)}{dlnQ^2} = \frac{\alpha_s(Q^2)}{2\pi}\int_z^1 \frac{dy}{y}[\sum_j P_{gq}(\frac{x}{y})q_i(y,Q^2) + P_{gg}(\frac{x}{y})g(y,Q^2)] \tag{1.2.4}$$

The splitting function, $P_{qq}(\frac{x}{y})$, is the probability for a quark with momentum fraction y to radiate a gluon, leaving the quark with momentum x.

In the low Q^2 region, there are other corrections to the Q^2 dependence of the structure functions so called "higher twist effects"due to the fact that the quarks also possess a momentum component perpendicular to that of the virtual photons. These corrections produce a term proportional to $\frac{1}{Q^2}$, and can be calculated using the Operator Product Expansion [13].

1.3 First momentum of g_1 and the GDH Sum Rule

In the parton model as mentioned earlier, g_1 can be expressed in terms of parton distribution functions:

$$g_1(x,Q^2) = \frac{1}{2}\sum_i e_i^2[q_i^{\uparrow}(x,Q^2) - q_i^{\downarrow}(x,Q^2)] = \frac{1}{2}\sum_i e_i^2[\triangle q_i(x) + \triangle \bar{q}_i(x)] \tag{1.3.1}$$

The first moment of the g_1 is generally given by the Operator Product Expansion, in terms of hadronic matrix element multiplied by calculable coefficient functions. In the assumption of free quark fields, the result simplifies to:

$$\Gamma_1 = \int_0^1 dx g_1(x) = \frac{1}{2}\int_0^1 \sum_i e_1^2 \triangle q_i(x) dx \tag{1.3.2}$$

The first moment Γ_1 can be expressed in terms of the $SU(3)_f$ nucleon axial charges a_j, which are defined as follows:

$$M a_j S_\mu = \langle P, S | J^j_{5\mu} | P, S\rangle; \qquad J^j_{5\mu} = \bar{\Psi}\gamma_\mu\gamma_5\frac{\lambda_j}{2}\psi \tag{1.3.3}$$

$$M a_0 S_\mu = \langle P, S | J^0_{5\mu} | P, S\rangle; \qquad J^0_{5\mu} = \bar{\Psi}\gamma_\mu\gamma_5\psi \tag{1.3.4}$$

Here, $J^j_{5\mu}$ and $J^0_{5\mu}$ are respectively the octet of quark $SU(3)_f$ axial-vector currents and the flavor singlet axial current. λ_j are the Gell-Mann matrices and $S^\mu(\lambda)$ is the proton's spin vector corresponding to a helicity state λ.

Using the parton distribution functions, we can write the nucleon axial charges in terms of the polarized parton distributions. After applying the $SU(3)$ flavor decomposition, the first moment can be expressed as:

$$\Gamma_1 = \int_0^1 dx g_1(x) = \frac{1}{12}[a_3 + \frac{1}{3}a_8 + \frac{4}{3}a_0] \tag{1.3.5}$$

Various sum rules predict the value of this integral. The Ellis-Jaffe sum rule predicts the numeric values of the proton and neutron first moment:

$$\Gamma_1^p = \int_0^1 dx g_1^p(x) = \frac{3}{36}a_3 + \frac{1}{36}a_8 + \frac{4}{36}a_0 = 0.186 \pm 0.004 \tag{1.3.6}$$

$$\Gamma_1^n = \int_0^1 dx g_1^n(x) = -\frac{3}{36}a_3 + \frac{1}{36}a_8 + \frac{4}{36}a_0 = -0.025 \pm 0.004 \tag{1.3.7}$$

under the assumption of $SU(3)$ symmetry an the approximation of massless quarks.

The Bjorken sum rule has been confirmed by experiments over years, however, it is not the case with the Ellis-Jaffe sum rule. The European Muon Collaboration (EMC) in 1988 measured a unexpected low value of Γ_1. At $Q^2 = 10.7GeV^2$, the average value of Γ_1^p obtained by the EMC experiment is $0.128 \pm 0.013 \pm 0.019$. The result is considerably smaller than the value predicted by the Ellis-Jaffe sum rule.

Further more, from the value of Γ_1, we can obtain the matrix element of the flavor singlet:

$$a_0 = \frac{3}{4}[12\Gamma_1^p - a_3 - \frac{1}{3}a_8] = 0.06 \pm 0.12 \pm 0.17 \tag{1.3.8}$$

while in the framework of the parton model, a_0 is expected to be closer to 1.

How much we can trust the theoretical predictions based on the naive parton model becomes a challenging question. In particular, there are experimental acceptance limitations that prevent a single experiment from measuring full x range at a fixed Q^2 for the first moment integral calculation. Theoretical extrapolations are therefore necessary in order to include the full range of x. The large x region is fairly well understood, g_1 approaches 0 as x approaches 1. But there hardly is any clear guidance of the x dependence expected in the low x region.

In QCD, there are two sources of Q^2 dependence, one is the QCD radiated corrections that is due to the hard gluons and the other is the higher twist corrections that takes care of the interactions between the active quark and the rest of the target. After applying the perturbative corrections on the extrapolation of Γ_1, such results were obtained [14]:

$$\begin{aligned} \Gamma_1^p(Q^2) &= \frac{1}{12}[E_{NS}(Q^2)(a_3 + \frac{1}{3}a_8) + E_s(Q^2)\frac{4}{3}a_0] \\ E_{NS}(Q^2) &= 1 - (\frac{\alpha_s}{\pi}) - 3.58(\frac{\alpha_s}{\pi})^2 - 20.22(\frac{\alpha_s}{\pi})^3 \\ E_S(Q^2) &= 1 - 0.333(\frac{\alpha}{\pi}) - 1.10(\frac{\alpha_s}{\pi})^2 \end{aligned} \tag{1.3.9}$$

The corrected value of Γ_1^p is approximately 0.186, which is still too high for the EMC measurement ($\Gamma_1^p = 0.128 \pm 0.013 \pm 0.019$ at $Q^2 = 10.7$ GeV) [8]. Thus we know that the QCD improved corrections do not solve the conflict between the EMC measured first moment and the naive parton model predicted value.

At low 4-momentum transfer ($Q^2 \leq 1$) region, due to the relatively low energy, the incoming lepton does not view the hadron target as simply independent partons, but probes the target at a hadronic level as well. Nucleon resonances and multi-pion states occur as this transition between partonic and hadronic scale takes place. Therefore, the low Q^2 region has been known as the resonance region.

The nucleon resonances can be expressed in terms of the photon helicity amplitudes [15]. Transverse virtual photons have helicity $\lambda = \pm 1$ and correspond to right or left-handed circular polarization, while longitudinal photons have $\lambda = 0$. The polarization vectors are $\varepsilon_\pm^\mu$ for the transverse photons and ε_0^μ for the longitudinally polarized virtual photons.

The corresponding components of the electromagnetic current $J_{\mu\nu}$ are:

$$\begin{aligned} J_{\pm} = \varepsilon^{\mu}_{\pm} J_{\mu\nu} &= \pm \frac{1}{\sqrt{2}} (J_x + iJ_y) \\ J_0 = \varepsilon^{\mu}_{0} J_{\mu\nu} &= \frac{Q}{\nu} J_z \end{aligned} \tag{1.3.10}$$

The helicity amplitudes connect a nucleon $N_{\frac{1}{2},m_s}$ with a spin projection m_s with any nucleon resonance N^*_{j,m_j} of spin j and projection m_j. The three basic helicity-related amplitudes can therefore be constructed for a nucleon of mass M and spin $\frac{1}{2}$ [15]:

$$\begin{aligned} A_{\frac{1}{2}} &= \frac{e}{2M} \sqrt{\frac{M}{W^2 - M^2}} \langle N^*_{j,+\frac{1}{2}} | J_+ | N_{\frac{1}{2},-\frac{1}{2}} \rangle \\ A_{\frac{3}{2}} &= \frac{e}{2M} \sqrt{\frac{M}{W^2 - M^2}} \langle N^*_{j,+\frac{3}{2}} | J_+ | N_{\frac{1}{2},-\frac{1}{2}} \rangle \\ S_{\frac{1}{2}} &= \frac{e}{2M} \sqrt{\frac{M}{W^2 - M^2}} \langle N^*_{j,+\frac{1}{2}} | J_0 | N_{\frac{1}{2},-\frac{1}{2}} \rangle \end{aligned} \tag{1.3.11}$$

The total cross section can thus be constructed with the helicity amplitudes. T stands for transverse, L stands for longitudinal and LT stands for interference cross section:

$$\begin{aligned} \sigma_T(\nu_R, Q^2) &= \frac{2M}{\Gamma_R M_R} [|A_{\frac{1}{2}}|^2 + |A_{\frac{3}{2}}|^2] \\ \sigma_L(\nu_R, Q^2) &= \frac{4M}{\Gamma_R M_R} [|S_{\frac{1}{2}}|^2] \\ \sigma_{LT}(\nu_R, Q^2) &= \frac{2M}{\Gamma_R M_R} [|A_{\frac{1}{2}}|^2 + |S_{\frac{3}{2}}|^2] \end{aligned} \tag{1.3.12}$$

where $\nu_R = \frac{M_R^2 - M^2 + Q^2}{2M}$ and M_R is the invariant mass of the resonance, Γ_R is the decay width.

The same cross sections can be written in terms of the structure functions g_1 and F_1. The transverse and interference cross sections are:

$$\begin{aligned}
\sigma_T^{1/2}(\nu_R, Q^2) &= \frac{4\pi^2\alpha}{MK}(F_1 + g_1 - \frac{2Mx}{\nu}g_2) \\
\sigma_T^{3/2}(\nu_R, Q^2) &= \frac{4\pi^2\alpha}{MK}(F_1 - g_1 + \frac{2Mx}{\nu}g_2) \\
\sigma_{LT}(\nu_R, Q^2) &= \frac{4\pi^2\alpha}{MK}\frac{Q}{\nu}(g_1 + g_2)
\end{aligned} \tag{1.3.13}$$

where K is the photon flux.

Combining the above equations, we can express the structure function g_1 in terms of the two transverse cross sections and the interference cross section:

$$g_1 = \frac{MK}{8\pi^2\alpha(1 + \frac{Q^2}{\nu^2})}[\sigma_T^{\frac{1}{2}} - \sigma_T^{\frac{3}{2}} + \frac{2Q}{\nu}\sigma_{LT}] \tag{1.3.14}$$

The GDH (Gerasimov-Drell-Hearn) Sum Rule relates the difference of the two transverse cross sections to the anomalous magnetic moment of the nucleon κ[7]:

$$-\frac{\kappa^2}{4} = \frac{M}{8\pi^2\alpha}\int_{\nu_{th}}^{\infty} \frac{\sigma_T^{1/2} - \sigma_T^{3/2}}{\nu} d\nu, \tag{1.3.15}$$

ν_{th} is the one pion photoproduction threshold.

The GDH sum rule is derived in the real photon limit, $Q^2 = 0$. Assuming the cross sections at the real photon limit connects smoothly with virtual photon cross sections where Q^2 is very small, we can obtain the generalized GDH sum rule as follows:

$$I_1(Q^2) = \tfrac{2M^2}{Q^2} \textstyle\int_0^{x_0} g_1(x, Q^2)dx$$

$$= \frac{M^2}{8\pi^2\alpha} \int_{\nu_{th}}^{\infty} \frac{1 - Q^2/2m\nu}{1 + Q^2/\nu^2} (\sigma_{1/2}(\nu, Q^2) - \sigma_{3/2}(\nu, Q^2) + \frac{2Q}{\nu}\sigma_{LT}(\nu, Q^2))d\nu/\nu \quad (1.3.16)$$

As $Q^2 \to 0$,

$$\lim_{Q^2 \to 0} I_1(Q^2) \Rightarrow \frac{M^2}{8\pi^2\alpha} \int_{\nu_{th}}^{\infty} (\sigma_{1/2}(\nu, Q^2) - \sigma_{3/2}(\nu, Q^2))\frac{d\nu}{\nu}$$

$$\Gamma_1 = \frac{Q^2}{2M^2} I_1(Q^2) \Rightarrow \frac{Q^2}{16\pi^2\alpha}(-\frac{2\pi^2\alpha\kappa^2}{M^2}) \Rightarrow -\frac{Q^2\kappa^2}{8M^2} \quad (1.3.17)$$

We can see from this expression of Γ_1 that the first moment of the spin related structure function, g_1, approaches zero with a negative slope while obviously being positive in the high Q^2 region. This negative slope is called the GDH slope. One of the goals of our $EG4$ experiment is to measure the GDH slope at very low Q^2 under the real photon approximation for the deuteron target.

There are several phenomenological models that describe the GDH slope in the resonance region. We will discuss two of them now.

1.4 Burkert and Ioffe model

The strong variation of Γ_1^p with Q^2 in the resonance region is caused by the transition from by the resonance-driven coherent scattering to the incoherent scattering of the constituent quarks. The evolution of the sum rule was originally described by Anselmino *et al* [16] through the parameterizations based on the vector meson dominance model. The model was later refined by Burkert and Ioffe [17] by treating explicitly the contributions of individual resonances. The contribution from resonance production has a strong Q^2 dependence for small Q^2 and decreases rapidly as Q^2 increases. At $Q^2 = 0$, approximately 80% of the GDH sum rule comes from the contribution of the Δ resonance, $P_{33}(1232)$. The $\Delta(1232)$ resonance is a spin 3/2 isobar of the nucleon, and is given by the strength of the $A_{3/2}$ amplitude. This amplitude requires a change of helicity and a flip of the quark spin.

The model by Burkert and Ioffe[18] measures the resonance and non-resonance contributions to the quantity $I_1(Q^2)$ separately.

$$\frac{2M^2}{Q^2}\Gamma_1(Q^2) = I_{GDH}(Q^2) = I^{res}(Q^2) + I'(Q^2) \tag{1.4.1}$$

where $\Gamma^{res}(Q^2)$ is the resonance contribution which is modeled up to $W = 1.8GeV$ using meson electroproduction data and the non-resonant part of $I_1(Q^2)$ is parameterized by a smooth function which is a sum of monopole and dipole term [18].

$$I'(Q^2) = 2M^2\Gamma^{as}[\frac{1}{Q^2+\mu^2} - \frac{c\mu^2}{(Q^2+\mu^2)^2}] \tag{1.4.2}$$

where Γ^{as} is the asymptotic value of $\Gamma_p(Q^2)$ at large Q^2, μ is the mass parameter characterizing the model, which is set to $\mu = m_p$ here. The variable c can be determined by the GDH sum rule at the real photon limit:

$$I_0 = I_1^{res}(0) + I_1'(0) = -\frac{1}{4}\kappa^2 \tag{1.4.3}$$

which gives

$$c = 1 + \frac{1}{2}\frac{\mu^2}{M_N^2}\frac{1}{\Gamma^{as}}[\frac{1}{4}\kappa^2 + I^{res}(0)] \tag{1.4.4}$$

The model predicts a change of sign for $\Gamma_p^1(Q^2)$ at $Q^2 \sim 0.8GeV^2$. The sign change is generated by the contribution of the $\Delta(1232)$ resonance, which gives a large negative value at small Q^2. We will show the comparison between the experimental data for Γ_p^1 and prediction by the Burkert and Ioffe model in Figure 1.4.

1.5 Soffer and Teryaev model

Soffer and Teryaev[19] predicts the Γ_1 value by incorporating Γ_2, the first moment of the second spin structure function g_2 into the picture. According to the Burkhardt-Cottingham sum rule, as $Q^2 \to \infty$,

$$\int_0^1 g_2(x)dx = 0 \tag{1.5.1}$$

While at $Q^2 = 0$ I_{1+2} can be calculated using the GDH sum rule,

$$I_{1+2}(0) = \frac{e\kappa}{4} \tag{1.5.2}$$

where e is the nucleon charge in elementary units. Parametrization in the intermediate Q^2 region was made for the total first moment Γ_{1+2} and Γ_1 can be deduced from there. For the proton case, the simplest parametrization was used to interpolate I_{1+2} between $Q^2 = 0$ and large Q^2 [19]:

$$I_{1+2}(Q^2) = \theta(Q_0^2 - Q^2)[\frac{e\kappa_p}{4} - \frac{2m_p^2 Q^2}{Q_0^2}\int_0^1 g_1(x)dx] + \theta(Q^2 - Q_0^2)\frac{2m_p^2}{Q^2}\int_0^1 g_1(x)dx \tag{1.5.3}$$

The resulting crossing point for Γ_p^1 is at $Q^2 \sim 0.2GeV^2$, which is below the resonance region.

Figure 1.4 shows the comparison of the experimental data and Γ_1^d predictions according to the two phenomenological models.

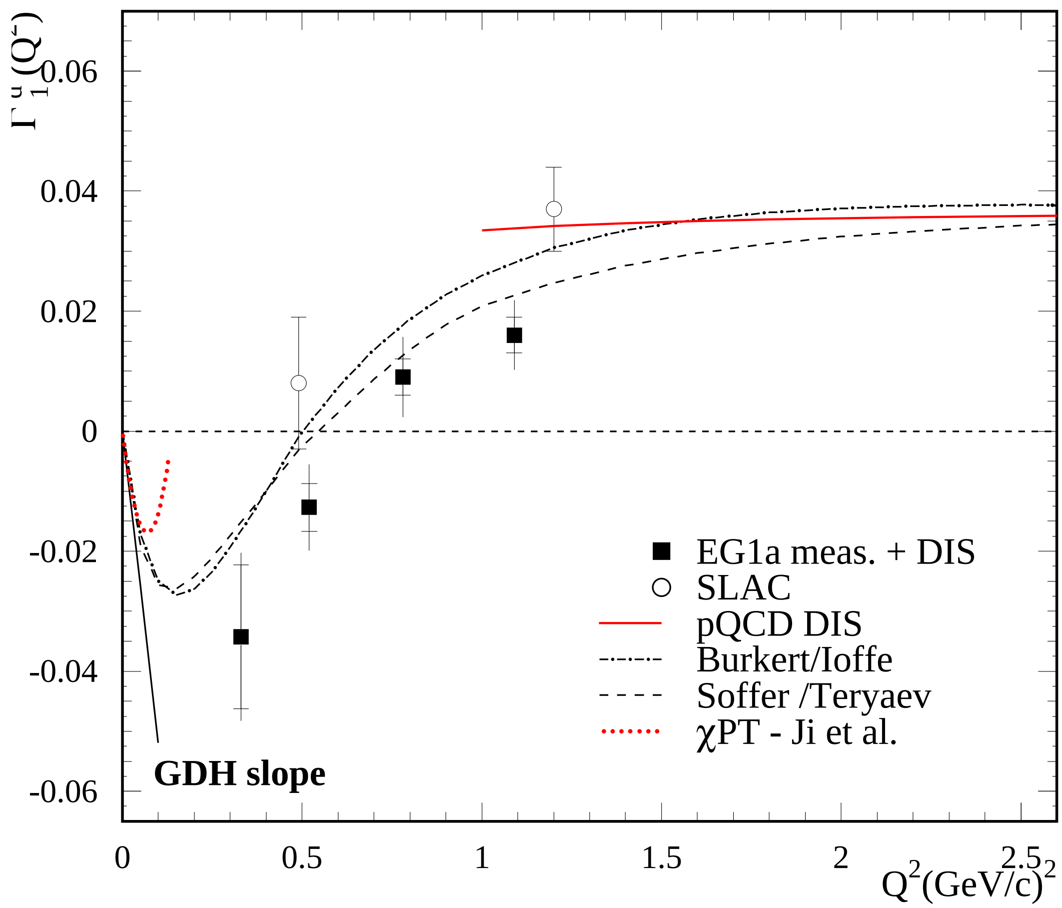

Figure 1.4: Predictions for Γ_1^d. Previous CLAS data and SLAC E143 data are also plotted.

Chapter 2

Experimental Setup

2.1 Electron Beam at TJNAF

The Thomas Jefferson National Acceleration Facility (JLab) operates a continuous wave polarized electron accelerator producing a high luminosity continuous electron beam with energies ranging from 800 MeV to almost 6 GeV. Electrons accelerated by klystrons are propagated through wave guides to superconducting RF accelerating cavities.

The electric field induced in the superconducting RF cavity is parallel to the beam axis. Its maximum value lies on the axis and decays radially to zero at the walls. The CEBAF accelerator consists of a 45 MeV injector capable of producing three beams, two superconducting linac segments connected by re-circulation arcs, a beam switch yard and three experimental halls: A, B and C.

The injector generates a beam with a nominal energy of 45 MeV and a 1.497 GHz bunch structure. The orientation of the electron spin can be selected at the injector by using a Wien filter [20] consisting of perpendicular electric and magnetic fields transverse to the electron momentum. The Wien filter can rotate the polarization of the beam without disturbing the momentum. The electric field is adjusted for a desired spin rotation and the magnetic field is used to counterbalance the Lorentz force on the electron.

The main accelerating structure consists of two superconducting linacs about 240 meters long, connected by the recirculating arcs. Each linac segment contains 25 cryomodules, each with 8 superconducting RF cavities. The cryomodules are separated from each other by a room temperature section which consists of focusing quadrupole magnets, dipole steering magnets, beam diagnostics and vacuum equipment. The dipole steering magnets and focusing quadrupole magnets serve to confine and guide the beam through the accelerator. The linacs are connected by transport lines, composed of sections called "spreaders", recirculating arcs and "recombiners". [21] The electron beams are bent vertically by the spreaders though an angle α which is inversely proportional to the beam energy. Recombiners are magnets that bend each individual beam by an angle -α. The recirculation regions were designed to minimize the synchrotron radiation effects by incorporating sufficiently large bending radii and strong focusing. The energy spread in the beam is $\sim \Delta E/E \sim 10^{-4}$, with the beam current ranging from 100pA to 100μA. Figure 2.1 shows the components of the CEBAF accelerator.

The three beams are separated at the switch yard and delivered to Hall A, B and C with the separation between bunches being 2.04 ns. The three experimental halls are equipped with a variety of spectrometers for different programs. The two spectrometers in Hall A are designed for high resolution experiments with $\Delta p/p \sim 10^{-4}$, solid angle(10msr) and large momentum acceptance $(10 - 15\%)$. Hall B is equipped with the CEBAF Large Acceptance Spectrometer (CLAS) which was designed for

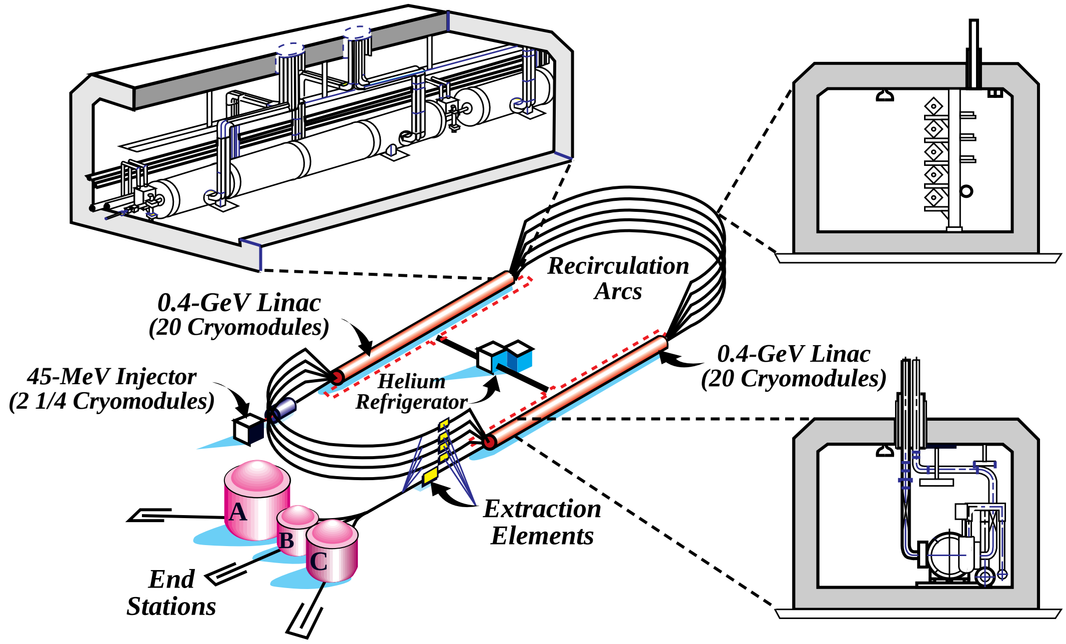

Figure 2.1: CEBAF Accelerator. One of the cryomodules is shown in the upper left corner. A vertical cross section of a cryomodule is shown in the lower right corner. A cross section of the five recirculation arcs is shown in the upper right corner.

photonuclear and electronuclear studies with low luminosity ($10^{34} cm^{-2} sec^{-1}$). CLAS allows multi particle detection and identification within $\sim$ 80% of 4π and 0.1 to 6 GeV/c in momentum. Hall C contains two magnetic spectrometers of medium momentum resolution ($\sim$ 10 MeV). These are the High Momentum Spectrometer (HMS) with a maximum momentum of 7 GeV/c and the Short Orbit Spectrometer (SOS).

The polarized electrons are produced by inducing bandgap photoemission from a strained GaAs cathode. Layers of various GaAs substrates with different lattice spacing together form the cathode. Pure GaAs grows on top of $GaAs_{0.72}P_{0.28}$. The small lattice spacing of $GaAs_{0.72}P_{0.28}$ creates strain on the spacing of GaAs, thus slightly shifts the electron energy levels and breaks the degeneracy [22] as shown in

Figure 2.2, resulting a gap in the $P_{3/2}$ energy levels. In principle, one can achieve a beam polarization of 50% from pure GaAs. If the cathode is illuminated with circularly polarized laser light with the right range of energy, the electrons from the energy level $P_{3/2}, m_j = 3/2$ excite into the conduction band and subsequently escape into the surrounding vacuum. However, because of the energy gap, the electrons from the energy level $P_{3/2}, m_j = 1/2$ are not excited by the laser light. Electrons excited to the conduction band are bound to the surface of the material by $\sim 4eV$ and cannot escape. For this reason the surface of GaAs is treated with the monolayer of cesium and fluorine to lower the work function so that the electrons can escape. The sign of electron polarization is flipped at frequency of 1 Hz by reversing the laser polarization with a pseudo-random sequence.

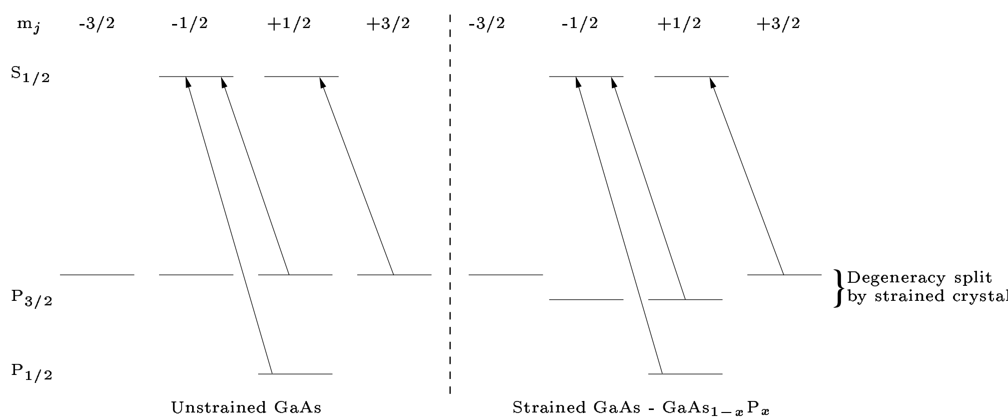

Figure 2.2: The difference in energy levels of GaAs and strained GaAs.

The polarization of the beam is measured initially at the injector using a 5 MeV Mott Polarimeter [23]. The beam polarization is measured again in Hall B by a Moller Polarimeter located upstream of the polarized target. The Hall B Moller polarimeter target is a 25 μm thick magnetized iron foil where a fraction of electrons are polarized. The often scattering electrons are guided by two sets of quadrupole magnets to the two fiber scintillators where they are detected in coincidence. The kinematics of Moller scattering provides a correlation between the energy and the scattering angle of the electron [24]. By measuring the asymmetry in the number of electrons scattered with the beam polarized parallel and anti-parallel to its momentum, with the knowledge of the Moller target polarization, we can thus derive the beam polarization. The typical beam polarization during the Eg4 experiments was ~80%.

Continuous monitoring of the beam delivered to Hall B is done by three beam position monitoring devices (BPM) and three beam current monitors (BCM). These BPMs and BCMs are positioned upstream of the polarized target cells provide the position and intensity of the beam and are read at the rate of 1Hz. The Faraday cup enables precise measurements of the integrated beam charge. A combination of the BCMs and the Faraday cup readings gated to the beam helicity gives us a measurement of the beam charge asymmetry, which arises when there is more current in one helicity state than in another.

2.2 Polarized Target

The theory and technology of producing solid polarized targets consisting of solid diamagnetic materials doped with paramagnetic radicals have been developed over the past 50 years. Solid polarized targets offer some advantages over gas and liquid targets, such as high density and high construction flexibility [25]. The Eg4 experiment in Hall B used solid ammonia targets that were doped with paramagnetic radicals and polarized via the method of Dynamic Nuclear Polarization (DNP) [26].

Because the nucleon has a much smaller magnetic momentum than that of an electron, it is easier to reach high electron polarization than nucleon polarization. Thus the basic idea behind this polarization method is to produce high electron polarization in the sample and then transfer that to the nuclear spins. The dipole-dipole interaction between the electron and the nuclear spin then functions as the media to transfer the polarization from the electron spin to the nuclear spin. Free electrons, lattice holes or free radicals can serve as paramagnetic centers ($NH_2\cdot$) in the target material. As for the target material used in the Eg4 experiment, the paramagnetic centers are introduced by irradiating the ammonia target beads with a low energy electron beam.

For spin 1/2 particles with magnetic moment μ_J in a magnetic field B, the Boltzmann factor $e^{\frac{\mu_J B}{KT}}$ determines the particle population at a specific temperature T. For particles of spin 1/2 the polarization can be expressed as:

$$P_{1/2} = \tanh \frac{\mu B}{KT} \tag{2.2.1}$$

Given the small value of the proton's gyromagnetic ratio, the value of B/T must be at least on the order of $\sim 10^3$ Tesla/Kelvin in order to create a significant nuclear thermal equilibrium polarization [27]. On the other hand, a field of 1 T at the temperature of 1 K is sufficient to polarize free electrons to a value over 30% [**?**]. After the electrons doped in as paramagnetic centers are polarized, Dynamic Nuclear Polarization is then used to transfer the high electron polarization to the nuclear polarization.

The method of DNP is based on the Solid State Effect discovered in 1958, and is observed at low temperature and high magnetic field in a solid that contains atomic nuclei and unpaired atomic electrons [28]. The state of lower Zeeman energy has the electron spin anti-aligned with the magnetic field. Figure 2.3 shows the energy levels in a magnetic field.

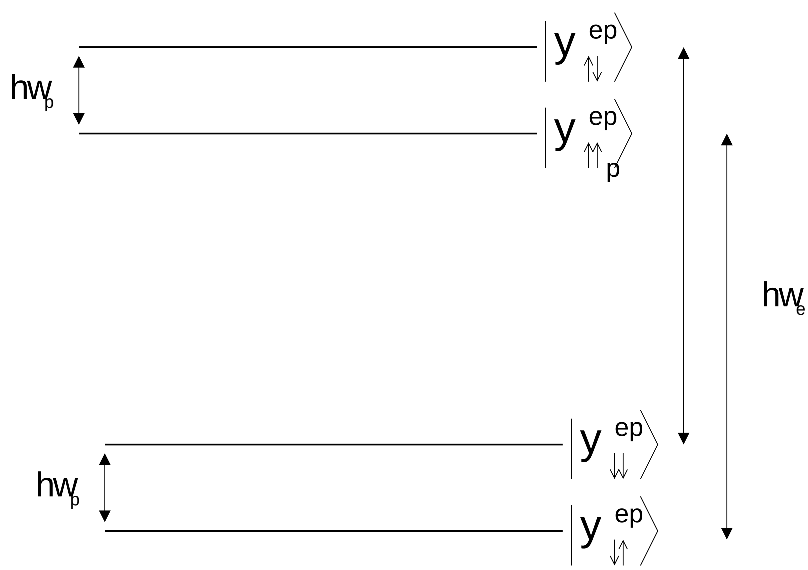

Figure 2.3: Energy levels of e-p spin system placed in a magnetic field. $h\omega_e$ represents the transition between electron spin states, while $h\omega_p$ represents the transition between the proton spin states. The system is described by 4 pure eigenstates without the perturbing Hamiltonian.

The only transitions allowed when the system is irradiated by an rf field are the ones with $\Delta S_z = \pm 1$ or $\Delta I_z = \pm 1$. When the frequency ω is near the electron Larmor frequency $\omega_s = \frac{g_s \mu_s}{B\hbar}$, the corresponding transitions will have $\Delta S_z = \pm 1$. Moreover, there is a dipole-dipole interaction between the proton and electron magnetic moments given by the following Hamiltonian:

$$H_{dip} = \frac{1}{r^3}[\mu_1 \cdot \mu_2 - \frac{3}{r}(\mu_1 \cdot r)(\mu_2 \cdot r)] = \frac{g\mu_B\mu_p/I}{r^3}[I \cdot S - 3r^{-2}(I \cdot r)(S \cdot r)] \quad (2.2.2)$$

where μ_1 and μ_2 are the magnetic moment of the proton and electron and r is the vector joining the positions of the nucleus and the free electron.

This interaction arises from a magnetic field B_S at the nucleus due to the dipole moment of the electron:

$$B_S = \frac{g\mu_B}{r^3} \quad (2.2.3)$$

The field B_S is much smaller than the Zeeman field, but it results in mixing of the "pure" electron states. A modified diagram of the electron proton system is shown in Figure 2.5. The dipole-dipole interaction induces simultaneous spin flips of an electron and a nucleus ($\psi_{\uparrow\uparrow} \rightarrow \psi_{\downarrow\downarrow}$), which is otherwise forbidden. The probability of this transition is labeled V. Although the value of V is much smaller than the allowed transitions, it nonetheless is considerable and it gives rise to the "Solid State Effect".

The Hamiltonian of a system of free electrons and a spin 1/2 nucleon placed in a magnetic field can be expressed as:

$$H = H_0 - \overrightarrow{\mu_e} \cdot \overrightarrow{B} - \overrightarrow{\mu_N} \cdot \overrightarrow{B} + H_{ss} \quad (2.2.4)$$

The term H_0 is the free Hamiltonian for the electrons and the nucleons. The second term describes the interaction between the electron and the magnetic field while the third term describes the interaction between the nucleon and the magnetic field. The final term arises due to dipole-dipole interaction between the electron and the nucleon.

The effects of H_{ss} on the free Hamiltonian is relatively small compared to the second the third term. Therefore the eigenstates of H can first be calculated by treating $-\overrightarrow{\mu_e} \cdot \overrightarrow{B} - \overrightarrow{\mu_N} \cdot \overrightarrow{B}$ as a perturbation to the free Hamiltonian. Figure 2.4 shows the splitting of energy levels, known as the Zeeman effect, due to this perturbation. Four states are resulted shown in figure 2.5.

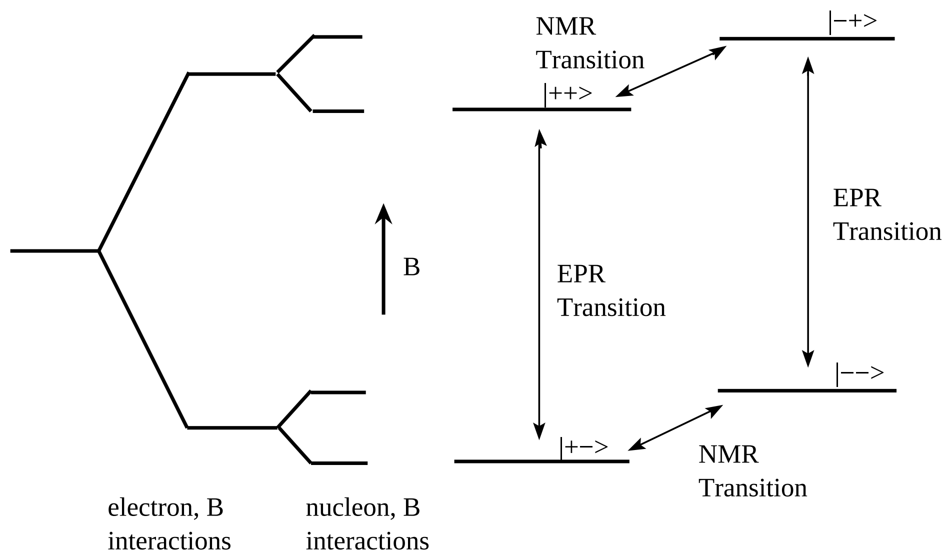

Figure 2.4: The energy level diagram of a spin 1/2 nucleon electron system that is placed in a magnetic field.

When an rf field with the appropriate frequency $\omega_e \pm \omega_p$ is applied to the e-p spin system, it results in a change in both the nuclear and electron spin directions. But because the coupling between the electron spins and the lattice is much stronger than that of the nuclear spins, the electron spin goes quickly back to its lower magnetic energy level, ready to be excited again, while the nuclear spin, with a longer relaxation time, stays in the new state. The spin polarization is thus passed from the free

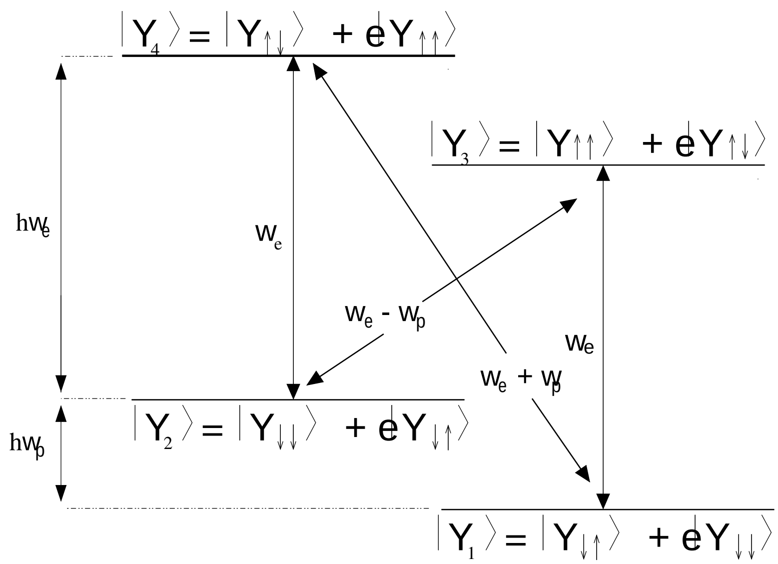

Figure 2.5: Allowed transitions in e-p spin system. The dipole interaction mixes eigenstates, and the transitions where both particles change their state are possible.

electrons to the nucleons. The nuclear polarization is created in the vicinity of the free electrons first, then gradually transmitted to the remote nucleons.

In the case of the deuteron target, the Zeeman splitting of a spin-1 system in a magnetic field has three evenly spaced quantized energy levels. However, in the ND_3 target, as in many other materials which do not have cubic symmetry, there are local electric field gradients that couple to the quadrupole moments of the deuterons causing an asymmetric splitting of the energy levels into two overlapping absorption lines. The quadrupole tensor Q of the deuteron couples to the gradient of the electric field ∇E [29] arising from the atomic electrons in the bonds. The energy levels of such a spin-1 system are written as [28] [30] [31]:

$$E_m = -\hbar\omega_d m + \hbar\omega_q 3\cos^2(\theta) - 1 + \eta\sin^2(\theta)\cos(2\phi)(3m^2 - 2) \tag{2.2.5}$$

where θ is the polar angle between the axis given by the N-D or O-D bond and the magnetic field $\rightharpoonup H_0$, and $m = -1, 0, 1$ is the spin magnetic quantum number. The azimuthal angle ϕ and parameter η are necessary for describing bonds where the electric field gradient is not symmetric about the bond axis. Specific definitions of ϕ and η can be found in References [32] and [28]. The electric field gradient has different values for the two types of bonds, while the quadrupole moment is the same.

For a given value of θ, there are two resonant frequencies in this system which correspond to the positive $E_0 \rightarrow E_1$ transition with energy $\Delta E_+ = E_0 - E_1$ and the negative $E_{-1} \rightarrow E_0$ transition with energy $\Delta E_- = E_{-1} - E_0$. The corresponding two resonant frequencies are no longer equal as in the case of pure Zeeman splitting, thus resulting in the double peak lineshape of the NMR signal for the deuteron target.

The target material used in the Eg4 experiments were polarized $^{15}NH_3$ and $^{15}ND_3$ ammonia beads. The target material is produced by slowly freezing the ammonia gas at 77K in liquid nitrogen, and crushing the frozen ammonia solid into small pieces, approximately 1-3 mm in diameter. Paramagnetic centers in the form of free radicals are introduced into the target beads with an electron beam.

During a scattering experiment, the target material continues to accumulate paramagnetic centers. While the pre-experimental doping takes place at relatively high temperatures, $80 - 90K$, these centers are created and will be stable at 1 K. These low temperature stable atoms can have a g factor different than 2, which would cause their Larmor frequency to be different from the frequency of the polarizing microwave field. As a result of this, the newly created centers do not participate in the DNP process, but they still contribute to the relaxation process via dipolar coupling to the nuclear spins [33]. As the number of new centers increases, the nuclear polarization deteriorates. During the experiment, the beam was rastered in a spiral pattern to avoid overheating local regions in the target. This was done using 2 magnets located upstream of the target. In order to make sure only the electrons scattered from the polarized target, as opposed to the ones scattered from other materials in the beam path are selected, a raster calibration will be performed and a cut on the vertex distribution will be made. Raster calibration will be discussed in detail in a later chapter.

The radiation damage can be repaired by a process called "annealing", which involves heating the target material up to $\sim 80 - 90K$ or higher. Figure 2.6 is a picture of the polarized ammonia target beads in the cell, the purple color is evidence of paramagnetic centers.

The polarization of the NH_3 target reached $\sim 90\%$ during the Eg4 experiment while the ND_3 polarization reached $> 45\%$. The target had to be annealed every 2-3 weeks. The beads change their color after exposure to electron beam, the edge has a lighter color due to less beam exposure.

Figure 2.7 shows the diagram of the target in the Hall B detector. The target includes a superconducting magnet that generates a magnetic field of $\sim 5T$, a helium evaporation refrigerator that can cool the target banjo temperature down to $\sim 1K$, microwave and a Nuclear Magnetic Resonance (NMR) system for monitoring the polarization and an insert housing the target cells.

Figure 2.8 is a detailed diagram of the target insert that houses different target

Figure 2.6: A photo of the target cell after beam exposure.

materials. The upper end of the insert is connected with NMR cables and microwave input. The insert used in Eg4 experiment houses targets cells for a NH_3 target, a ND_3 target, a Carbon target and an empty cell for background correction.

The NMR system [34] was used to monitor the target polarization during the Eg4 experiment. In the NMR technique an oscillating magnetic field B_1 of frequency ω perpendicular to the static field B is appiled. This causes the nucleons to have a spin precession along the field of B_1 at a frequency $\omega_1 = \gamma|\overrightarrow{B_1}|$. At the Larmor frequency $\omega = \omega_0$ and the vicinity area, the system absorbs the energy applied by the signal and flips the spin of the nucleons, resulting in a change of the susceptibility of the

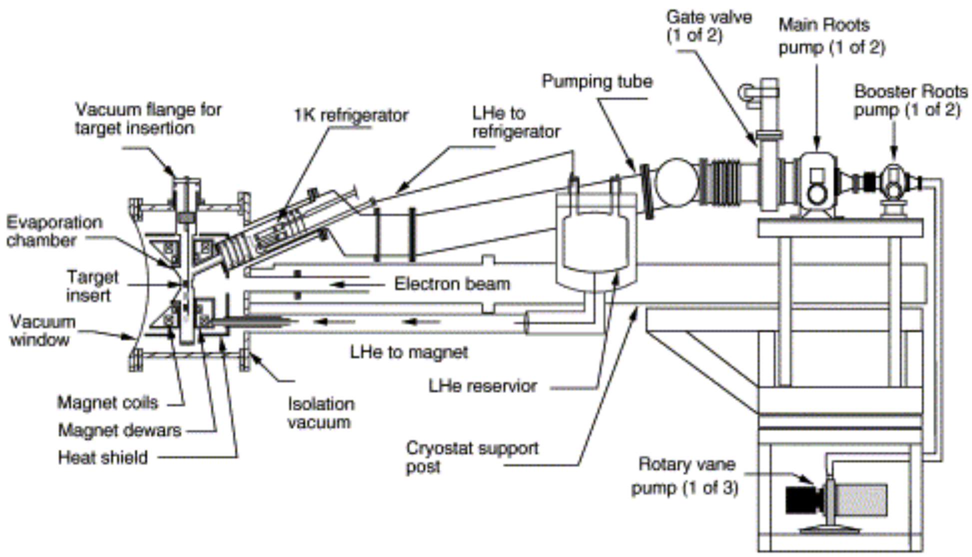

Figure 2.7: Diagram of the target in Hall B.

material:

$$\chi(\omega) = \chi'(\omega) - i\chi''(\omega) \tag{2.2.6}$$

For a given spin type, the absorptive part, $\chi''(\omega)$ of the susceptibility is sensitive to the target polarization [34]:

$$P = \int_0^\infty \chi''(\omega) d\omega \tag{2.2.7}$$

The NMR system shown in Figure 2.9 was designed to apply the oscillating magnetic field and to measure the susceptibility of the target material, thereby obtain the target polarization. The oscillating magnetic field B_1 was generated by a wire coil around the target. The coil also functions as an inductor in an alternating current LRC circuit. The inductance of the coil depends on the susceptibility of the target

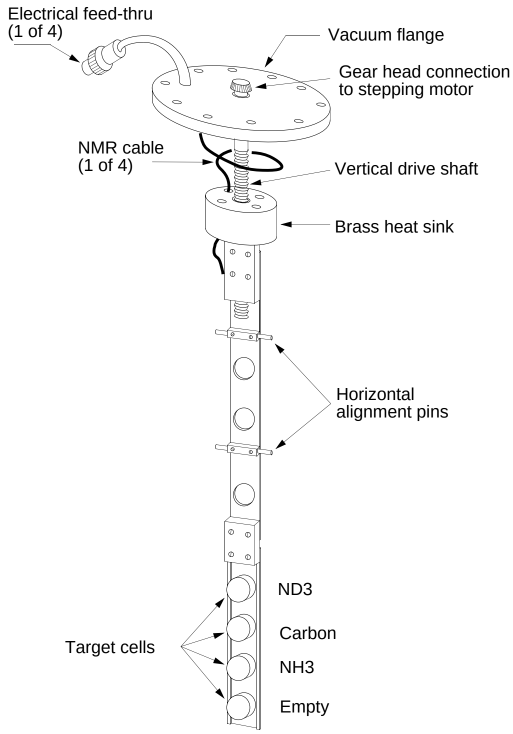

Figure 2.8: Diagram of target insert

material:

$$L(\omega) = L_0(1 + 4\pi\eta\chi(\omega)) \tag{2.2.8}$$

where L_0 is the inductance of the coil when the target material is completely unpolarized and the filling factor η describes the coupling of the material to the coil. The RF frequency is swept through a range of frequencies above and below the Larmor frequency in order to obtain the NMR signal. The calculation of target polarization of deuteron from NMR signals will be discussed in the latter chapters.

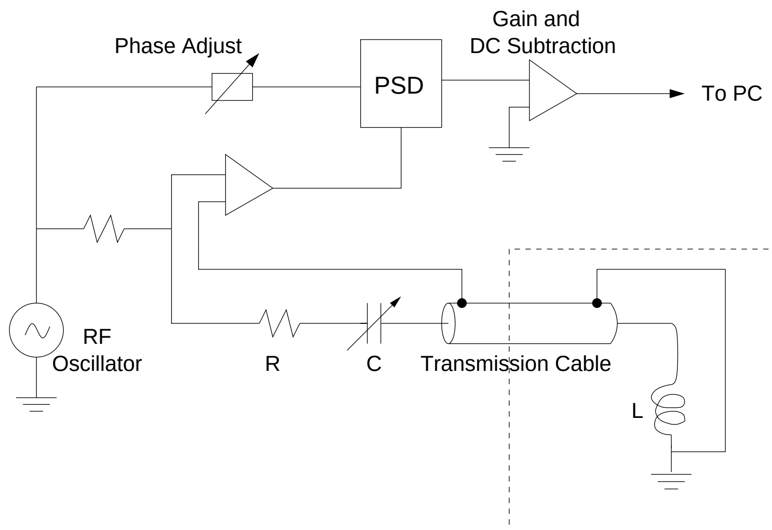

Figure 2.9: Diagram of the NMR circuit

2.3 CLAS

Hall B CLAS has a toroidal magnetic field produced by six superconducting coils which separate the detector into six wedge shaped sectors, each of which covers approximately 60^o degree the scattering sphere. Each sector contains Drift Chamber (DC) for tracking charged particles, Cerenkov Counter (CC) to separate electrons from pions, Scintillation Counters (SC) for determining particle flight time and Electromagnetic Calorimeters (EC) to identify electrons and neutral particles. The CLAS has a large acceptance coverage that ranges from $8°$ to $140°$ in the polar angle. Figure 2.10 illustrates the overall layout of the detector. For the inclusive analysis during Eg4 experiment, sector 6 was the only sector from which we extracted data.

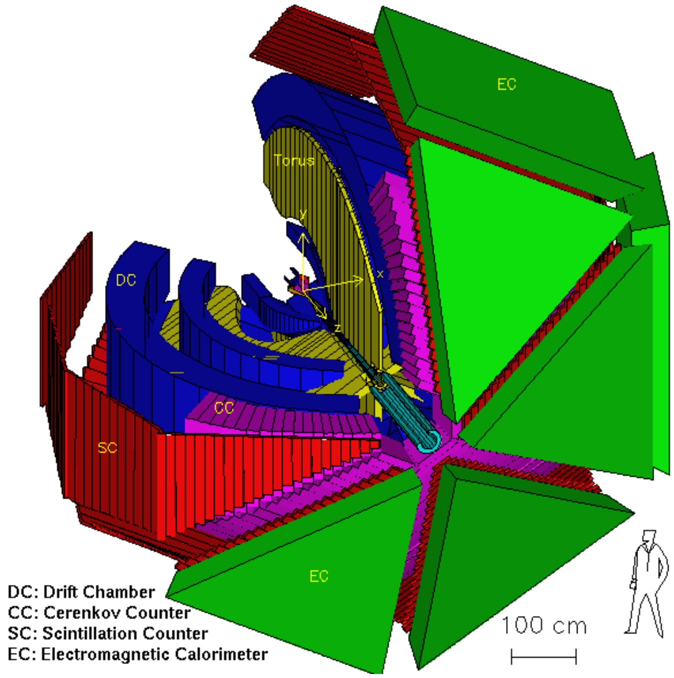

Figure 2.10: A cutaway view of the CLAS. Beam direction is out of the page.

2.4 Torus Magnet

The torus magnet has six superconducting coils that generate a main magnetic field in the ϕ direction circling the beam line. This structure allows homogeneous geometrical coverage of charged particles at large angles as well as providing good momentum and angle resolution and low background from electromagnetic interactions. Particle momentum can thus be measured by inducing a curvature which depends on the charge and momentum of the particle on its path. Figure 2.11 shows the diagram of the coils.

The system is usually described using spherical coordinates, with the z axis along

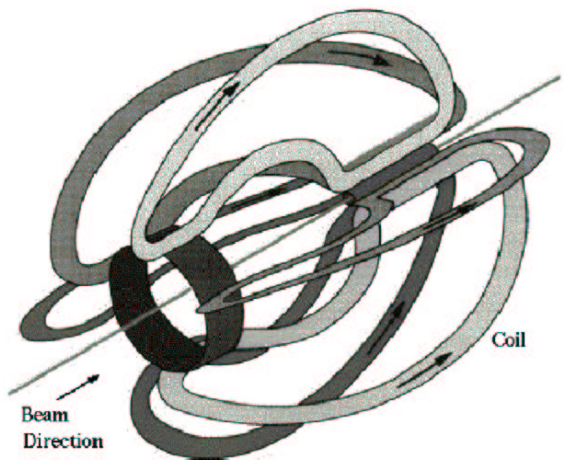

Figure 2.11: Diagram of the six coils of the torus magnet.

the beam direction, the x axis along the horizontal plane and the y axis along the vertical plane normal to the beam. θ is the polar scattering angle and ϕ is the azimuthal angle. Figure 2.12 shows a contour plot of magnetic field for CLAS in the midplane between two coils. The magnet is approximately 5 meters in the diameter and 5 meters in length. Each of its coils consists of 4 layers of 54 turns of aluminum-stablilized NDTi-Cu conductors. [35] The coils are cooled to a superconducting temperature of 4.5K by liquid helium circulating through cooling tubes that are located at the edge of the windings. The heat load is reduced by a liquid nitrogen shield and super-insulation.

The beam passes along the axis undeflected as the field is zero.

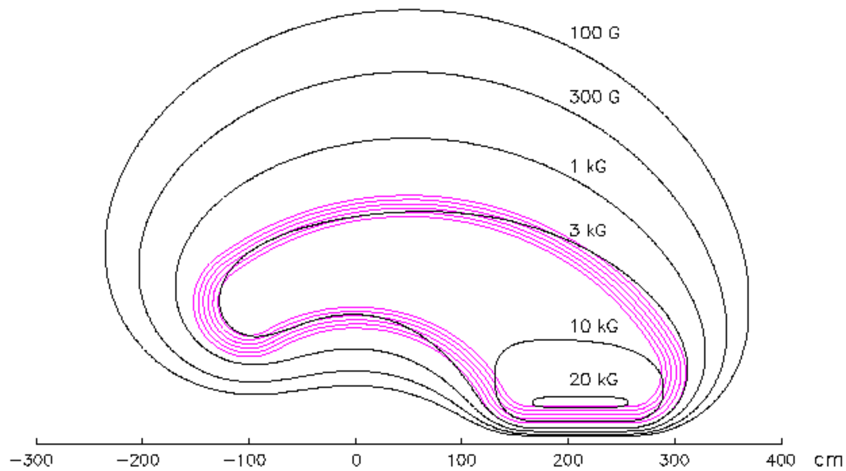

Figure 2.12: A contour plot of magnetic field for CLAS in the midplane between two coils.

2.5 Drift Chamber

The Drift Chamber (DC) in each sector is separated into three regions. Region 1 is the closest to the target and is in a low magnetic field. Region 2 is located in between the torus magnetic coils. Region 3 is the largest and is situated outside the magnetic coils. The relative position of the three regions are shown in Figure 2.13.

The chambers contain wires stretched between two endplates which are tilted at 60° between each other. It uses the drift time of electrons released by the ionization process in a gas to determine the spatial position of an ionizing particle. The chamber is filled with gas and is maintained at an electric field produced by the anode and cathode wires. The particle crossing the chamber ionizes the gas atoms, releasing electrons which drift to the anode wire. The drifting electrons produce more ionization, this creates an amplified signal which can be detected.

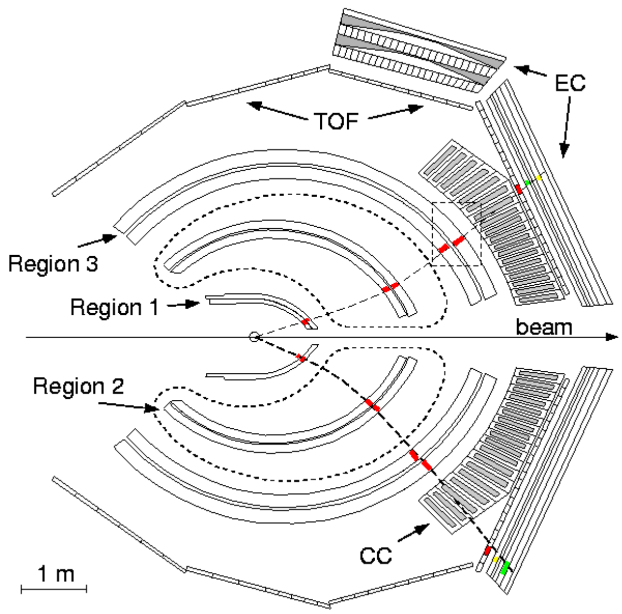

Figure 2.13: Midplane slice of CLAS, showing DC's three regions.

The drift cells are constructed from $20 \mu m$ gold plated tungsten sense wires $140 \mu m$ aluminum field wires. All six sectors are filled with 88% argon and 12% carbon dioxide gas mixtures. The field wires are kept at a negative potential and the sense wires are kept at a positive potential through a high voltage system.

2.6 Time of Flight Counters

The CLAS Time of Flight (TOF) system provides a high resolution timing measurement that can be used to calculate the speed and thus derive information regarding the mass of a charged particle. The CLAS TOF counters consist of 57 scintillators per sector. The last 18 of which are paired into nine logical counters. A photomultiplier tube and a light guide connect them at each end as shown in Figure 2.14.

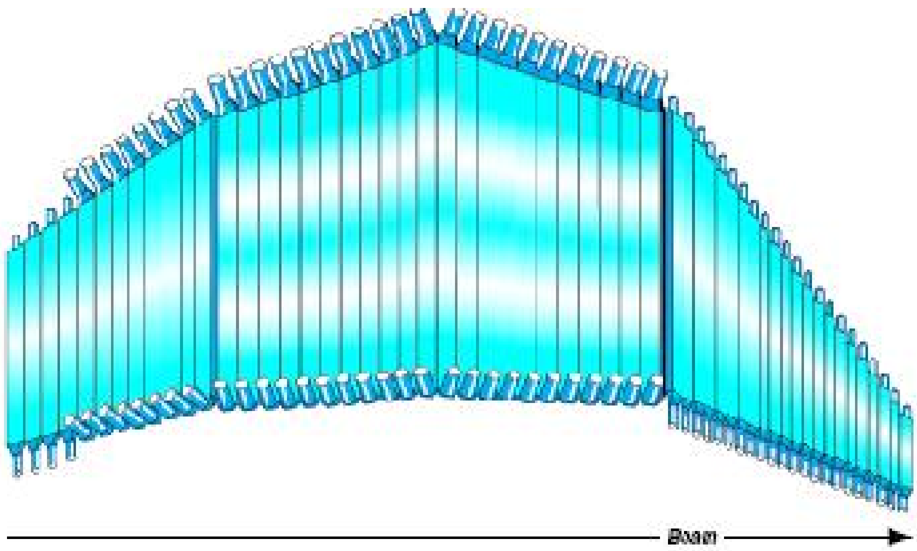

Figure 2.14: Time of Fight counters for one sector.

The scintillators are mounted in 4 panels. The length of the scintillators vary from 30cm to 450cm. The forward angle counters cover up to 45° and are 15cm wide. The rest of them are large angle scintillators, 22cm in width. Each scintillator, with a thickness of 5.08cm, is positioned in a way that it is perpendicular to the particle trajectory. The SC are designed to fit in between the Cerenkov Counters and the Calorimeter, covering large polar and azimuthal angles.

2.7 Cerenkov Counters

The Cerenkov Counters in CLAS are designed to separate electrons from pions. When a particle travels through the dielectric medium at a speed higher than light speed in that medium the Cerenkov light is emitted. The atoms in the vicinity of the charged particle trajectory become polarized and emit photons at a fixed angle θ determined by

$$\cos(\theta) = 1/\beta n \tag{2.7.1}$$

where $\beta = v/c$ and n is the refraction index in that medium. A threshold Cerenkov Counter detects particles whose velocity exceeds $1/n$. Gas radiator counters are often used when detecting particles with $\beta > 0.99$. The CLAS Cerenkov detector is filled with perfluorobutane C_4F_{10} at atmospheric pressure. Its refraction index $n = 1.00153$. The threshold of the particle energy correspondingly is:

$$E = \frac{m}{\sqrt{1-\beta^2}} = \sqrt{\frac{n}{n-1}}m = 18.1m \tag{2.7.2}$$

where m is the mass of the particle. The threshold energy is 9 MeV for electrons and 2.5GeV for pions.

The Cerenkov counter of CLAS consists of six identical Cerenkov optical units. One of these units is shown in Figure 2.15. One Cerenkov unit with 18 segments extends from 8° to 45° in the polar angle direction. Each segment is divided into two optical modules along the symmetry plane of the sector. Each optical modules has three mirrors, elliptical, hyperbolic and cylindrical. One PMT is connected to each module. The mirrors are aligned to optimize the light collection. The purpose of the Winston cone is to maximize the collection of the incoming rays.

Figure 2.16 shows the optical arrangment of one module in the Cerenkov detector. The Cerenkov counters are used to discriminate pions from electrons up to the pion momentum of 2.5 GeV/c. Pions that exceed this momentum can emit Cerenkov

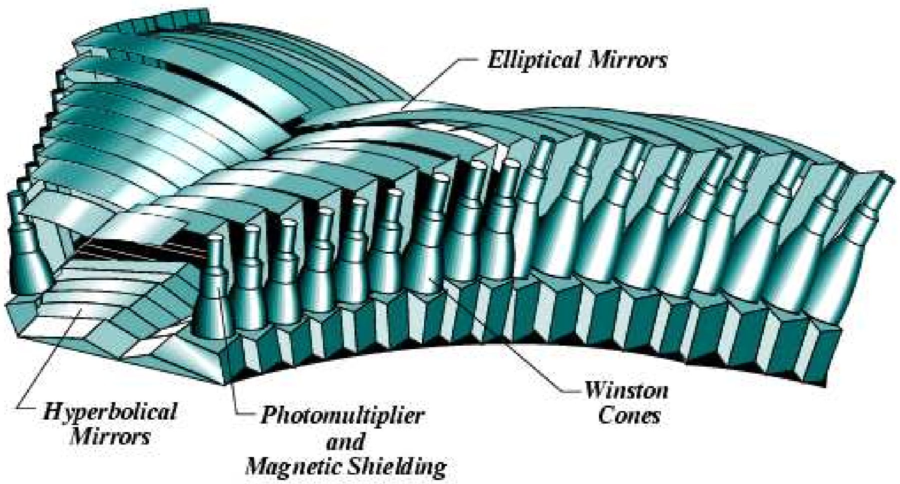

Figure 2.15: Array of CC optical modules in one sector.

radiation that resembles the electron radiation. Thus other detectors have to be used to identify these high energy pions. In addition, pions with a momentum below 2.5 GeV/c can also produce Cerenkov radiation through primary and secondary ionization of atomic electrons in the gas and surrounding environment. This occurs for around 1% pions. The electron efficiency within the fiducial acceptance of the CC exceeds 99%. Outside the fiducial region, the efficiency drops rapidly and varies greatly. Therefore the non-fiducial region is always excluded from the data analysis.

2.8 Electromagnetic Calorimeter

Since the Cerenkov counters are not sufficient in the case of a high momentum pion, the electromagnetic calorimeter is needed for further pion rejection. A calorimeter is a device that measures the total energy deposited by a crossing particle. Calorimeters

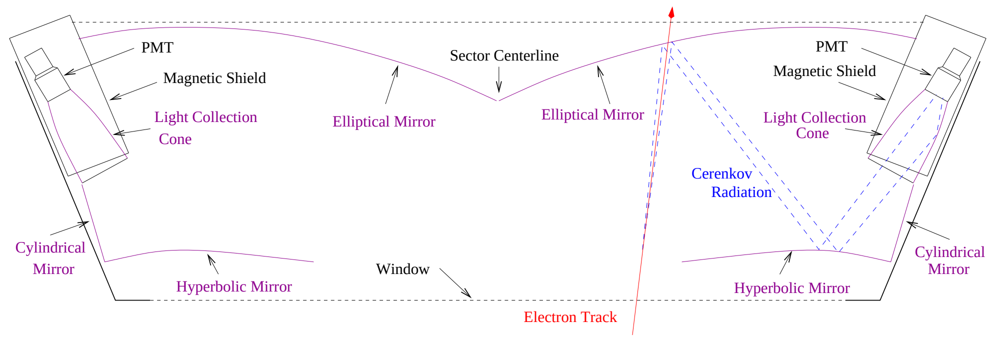

Figure 2.16: A schematic of a Cerenkov Segment.An example of an electron track and how the light produced is collected by the light collection cone is also shown.

are useful in detecting neutral particles and distinguishing between electrons and hadrons. Electrons with a energy higher than 100 MeV lose energy mostly through pair production. Radiated photons produce electron-positron pairs which in turn can radiate photons. This process feeds on itself and creates an electromagnetic shower of electrons and photons. All of the electron's energy is deposited in the Electromagnetic Calorimeter. The pions, on the other hand lose energy primarily through ionization. The total energy deposited in this process is independent of the beam energy, the peak located at the minimum ionizing energy.

The calorimeter of CLAS is made of alternating layers of lead and scintillating material. The lead is a high Z metal that enhances the shower rate and the scintillator material is necessary to sample the energy loss. CLAS has 8 calorimeter units, with one in each sector in the forward region (polar angle of 10° to 45°), and 2 of them at polar angle 50° to 70° in sectors 1 and 2. Figure 2.17 shows the structure of the the forward angle calorimeters.

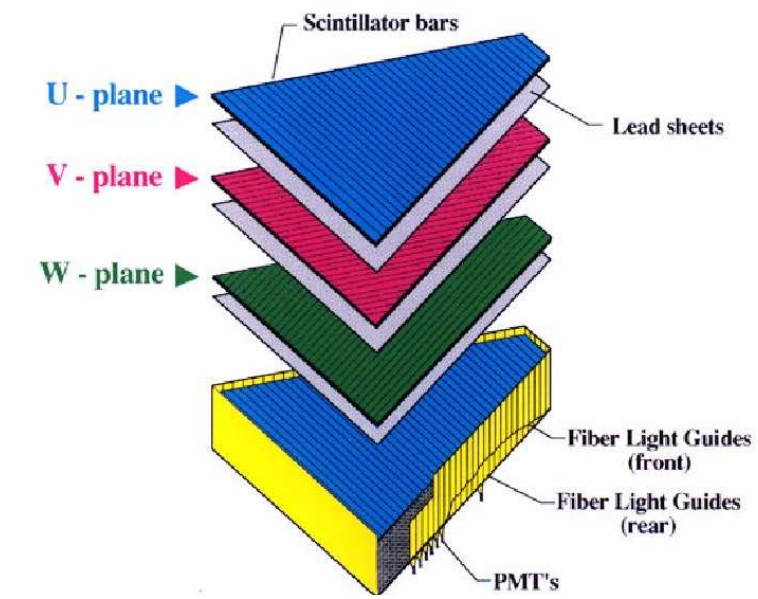

Figure 2.17: One of the six modules of EC.

The forward calorimeter has a lead to scintillator ratio of 1:5 with 40cm of scintillator and 8cm of lead per unit. The lead-scintillator configuration is shaped as a triangle. There are 39 layers of 10mm scintillator and 2.2mm lead in each layer. the ratio of radiation lengths of 10mm scintillator 2.2mm lead is $\sim$ 1:2 so that 1/3 of the energy is deposited in the scintillator and 2/3 of the energy is deposited in the lead.

The scintillator light is transmitted to PMTs. Large angle calorimeter units have similar structures as forward angle ones but have a rectangular shape.

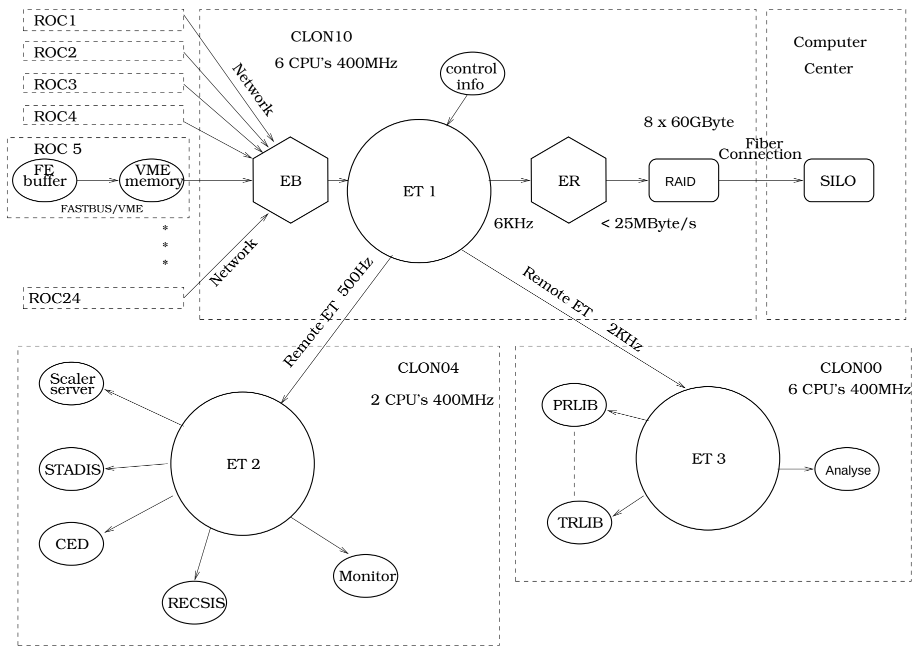

Figure 2.18: A schematic of the CLAS data flow.

2.9 The Trigger System And Data Acquisition System

The CLAS trigger system is built upon a two level system. The level 1 trigger requires a signal above threshold in the CC and EC. The level 2 trigger requires selects good events from those that have passed the level 1 trigger by using the DC track hits and by identifying a preliminary track.

For those events that passed the trigger requirements on energy and timing, information on the events is digitized in 24 FASTBUS and VME crates and are collected by 24 VME Readout Controllers. Figure 2.18 is an illustration of the CLAS data flow.

The digitized data are translated into tables and transferred through fast Ethernet lines to the online data acquisition system. The data acquisition system performs three important functions:

- Event Building. The Event Builder(EB) links together information from all the detectors and builds a complete event. These events are organized in predefined arrays called BOS banks. An event number and a run number for each event is assigned.

- Online Monitoring. The completed events are then transferred to the Event Transport(ET). Some of the ET systems are used for temporary data storage in order to perform online monitoring of the detector performance and event display.

- Event Recording. The Event Recorder performs the final task of data acquisition, permanent data storage. The data is first written to a disk and then transferred onto tape that is located in the control room of the computer center.

The accelerator, the CLAS detectors and the EG4 polarized target together an excellent combination of resources to collect data on polarized electrons scattered off of polarized nucleons. In the next chapter, the first step in the data analysis, the event reconstruction, will be described in detail.

Chapter 3

Event Reconstruction

The Hall B CLAS is able to distinguish between different particles in the multi-particle final states. The standard procedure is to calibrate each detector separately, obtaining reasonable calibration constants, evaluate the quality of the processed data and do another round of calibration if necessary. The reconstruction software combines all the information together to identify the tracks and information for event analysis. The event reconstruction consists of identification of charged and neutral particles and recording their momenta. Identification of an electron requires a matching track in all of the DC, CC, EC and TOF counters. For the Hall B Eg4 experiment, most of the data reconstruction was completed at the INFN Laboratory in Genova, Italy where the author participated in parts of the raster and Faraday cup calibration.

3.1 Track Reconstruction

Matching hits in time and position in the relevant detector components must be identified in order to find a good track. Track reconstruction is treated differently for charged and neutral particles.

- Charged particles

  Drift Chamber

  A possible particle track is preliminarily determined by the hit positions. HBT (Hit Based Tracking) is based on a series of pattern finding algorithms. [**?**]

  Cerenkov Counter

  The way to identify a particle track in CC is to put a restriction to the maximum value of the polar angle between the track projected to the CC plane and the detected position of the hit in the CC.

  Scintillator Counter

  To identify a hit in the TOF counter, the distance between the z position of the projected track and the z position of the hit on the TOF scintillator counter has to be less than 30cm.

  Electromagnetic Calorimeter

  To identify a track that agrees with the other detector components a software cut of 30 mm between the identified hit position and the projected track is required.

- Neutral particles

  Neutral particles are identified by finding clusters in the outer detectors with no charged particle track. They are detected in both EC and SC. The clusters are identified by determining their energy, position and time of the hit.

  The neutrons are detected by identifying a hit in the calorimeter that does not meet the requirements for a charged particle. Neutrons are distinguished from photons by flight time to the EC. The efficiency of neutron detection increases as the neutron momentum goes up, from 5% at 0.6 GeV to about 50% above 2 GeV.

π^0 and η measons are identified by detecting two coincident photon hits in the EC and constructing the mass ($M_{2\gamma}$) (Figure 3.1) of the primary particle that corresponds to the 2γ decay using the measured energy $E_{\gamma 1,2}$ and the polar angle $\Theta_{\gamma 1,2}$ of each photon [36]:

$$M_{2\gamma} = 2E_{\gamma 1}E_{\gamma 2}(1 - cos(\theta_{\gamma 1} + \theta_{\gamma 2})) \tag{3.1.1}$$

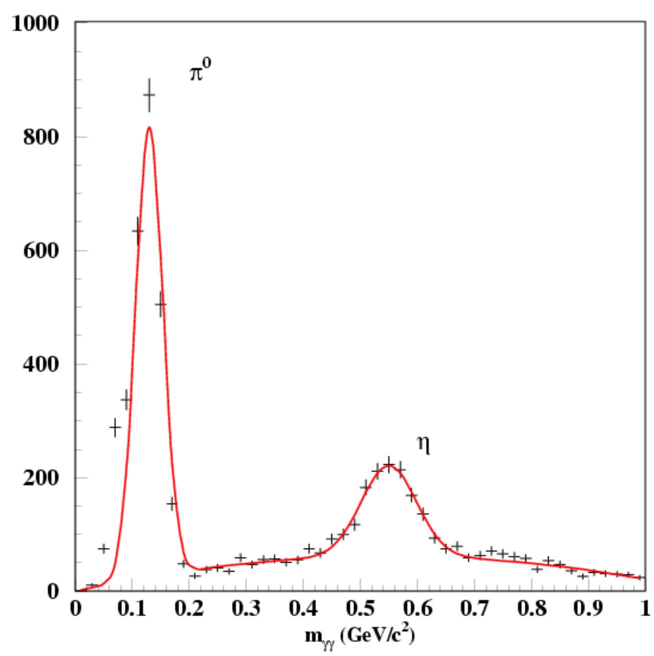

Figure 3.1: Invariant Mass of π^0 and η reconstructed using two photon events recorded in the EC.

3.2 Start Time Reconstruction

The start time of an identified track is determined by the Time of Flight (TOF) counter. The calibration of the TOF includes converting the raw time to digital (TDC) and amplitude to digital (ADC) values to time and energy respectively. The time delays for individual scintillator with respect to each other are adjusted by using the RF-signal from the accelerator as the reference timing signal. Since all electron bunches sent to Hall B are separated by the same time interval ($\delta T \sim 2.0039ns$), it can be used to align the timing of all scintillation counters to the same RF bunch.

The start time T^{el}_{start} of the trigger electrons can be calculated using:

$$T^{el}_{start} = T^{el}_{SC} - \frac{l}{\beta_{el} c} - T_{RFoff} \tag{3.2.1}$$

where T^{el}_{SC} is the time recorded at the TOF counter and c is the speed of light. The term $\frac{l}{\beta_{el} c}$ calculates the start time of using the total length of the electron track by tracing it to the vertex and assuming the particle is traveling at the speed of the light ($\beta_{el} = 1$). The T_{RFoff} can be expressed as:

$$T_{RFoff} = \mod((T^{el}_{SC} - \frac{l_{el}}{\beta_{el} c} - t_{RF}), \delta T) - \frac{\delta T}{2} \tag{3.2.2}$$

where t_{RF} is the RF time used for the alignment. Figure 3.2 shows a histogram analysis for RF offset.

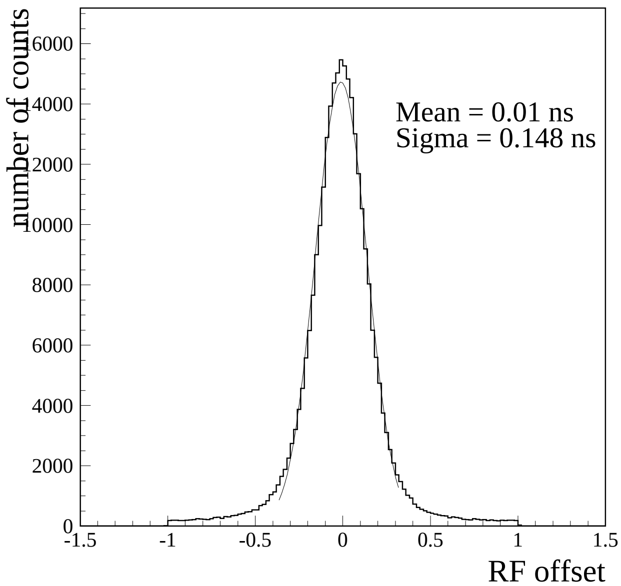

Figure 3.2: The RF offset for one EG1 run. Data are taken at a beam energy of 1.6 GeV.

3.3 Beam Charge Helicity

The helicity of the beam is pseudo-randomly selected at a frequency of 30Hz. Each triggered physics event is labeled with the helicity state in the 'HEAD' bank. The total beam charge is integrated over one helicity state. This information is passed immediately into the data stream after a helicity flip. The Helicity Physics algorithm (HelP) is designed to realign each physics event with the respective helicity information. This is the so called 'online' helicity monitoring. During the Eg4 data analysis, helicity information is also stored in the 'HLS' bank so that we can properly recover the helicity labels for those times when the helicity label failed to latch. This step is the 'offline' helicity analysis, the result of which used to produce the charge asymmetry.

3.4 Electron Identification

During the Eg4 experiment, the event trigger used a combination of the Electromagnetic Calorimeter and the Cerenkov Counter signals and accepted all events above the threshold. The off-line reconstruction code (RECSIS) creates a second filter of events by requiring more strict particle definitions and uses the Simple Event Builder (SEB) to identify particles. The RECSIS identification of the particles is primarily based on the TOF information from the Scintillator Counters and the track reconstruction by the Drift Chamber. This gives us a preliminary source of possible electron events from which we select accurate electron trigger events by applying various cuts and corrections for the inclusive scattering analysis.

The primary contamination for electrons comes from negatively charged pions. The EC and CC detectors were specifically used to separate pions and other negatively charged particles from electrons. After the completion of the reconstruction by the RECSIS code, the list of cuts below were applied for the inclusive analysis to identify electrons:

- Group 1 Cuts:

  $gpart > 0$ requires at least one particle in the SEB summary bank.

  $q > 0$ requires the particle in the SEB summary bank to have a negative charge.

- Group 2 Cuts:

$0 < dc \leq dcpart$ the particle in the SEB summary bank has a sensible pointer to the DC bank information

$0 < ec \leq ecpart$ the particle in the SEB summary bank has a sensible pointer to the EC bank information

$0 < sc \leq scpart$ the particle in the SEB summary bank has a sensible pointer to the SC bank information

$0 < cc \leq ccpart$ the particle in the SEB summary bank has a sensible pointer to the CC bank information

$stat > 0$ the particle in the SEB summary bank has sufficient consistent detector information for the Particle IDentification (PID), including Time Based Tracking (TBT)

$dcstat > 0$ TBT for the first particle in the SEB summary bank was successful

$p \geq 0.3$ reconstructed momentum greater than 0.3 GeV/c

- Group 3 Cuts:

  $90 < v_z < 110$ vertex cut on z postition (in cm)

  $|\phi_{proj}| \leq 10°$ a straight line connecting the CLAS center to the CC hit defines two "projective" angles, θ and ϕ. ϕ has to be within the nominal acceptance, $\pm 10°$.

- Group 4 Cuts (Cuts on EC):

  $E_{tot}/p > 0.0177 * p + 0.16$

  $E_{out}/p > -1.67 * E_{in}/p + 0.266$

E_{tot}, E_{in} and E_{out} are the total, incoming and outgoing energy deposited in EC respectively. p is the reconstructed momentum of the scattered particle.

- Group 5 Cuts (Osipenko Cuts):

  Geometrical matching between hit in the CC and track in the DC.

- Group 6 Cuts:

  Timing difference between SC and CC: $dt(SC - CC) > -3.0(ns)$

  Timing difference between EC and CC: $dt(EC - CC) > -3.0(ns)$

- Group 7 Cut:

  $Nphe > 5$ Cut on Cerenkov number of photo electrons.

The following sections will provide detailed information on some of these cuts.

3.5 Vertex Cuts

In order to make sure that the scattered electrons come from the target instead surrounding materials, it is important to set a boundary to the interaction vertex. In the CLAS coordinate system, the target center is at 100cm. The z vertex range was determined to be $90 < v_z < 110$ cm.

Interactions that come from outside this region are rejected for all particles. Before applying the vertex cut, a raster correction has to be carried out to obtain the proper v_z values. More detailed information concerning the raster correction will be discussed in section 3.10.

3.6 Cerenkov Counter Cuts

Identification of pions in the CC is quite successful as long as the pion energy is below the CC threshold value, in which case the pion peak can easily be distinguished from the electron signal. Figure 3.3 shows a sample signal from CC together with an applied cut at 2 photo electrons to identify the electron events. For the Eg4 experiment analysis at $\sim 1-2$ GeV incoming energies, the minimum photo electron cut was set to be 5. For the preliminary data analysis of Eg4 experiment, before pion contamination is studied closely, a relatively high cut was set to ensure the efficiency of electron identification.

3.7 Electromagnetic Calorimeter Cuts

Electrons and pions can be distinguished in the calorimeter due to their different patterns of energy deposition. Electrons emit photons and produce electromagnetic showers, with the total deposited energy proportional to their momentum. Pions, on the other hand, are minimum ionizing particles (MIP) and lose energy at a rate of ~ 2 MeV/gm/cm^2. The calorimeter is made of 39 layers of 10 mm thick scintillator and 2.2mm thick lead. Traveling through the calorimeter, the pions lose 78 MeV of energy independent of their momentum.

The spatial pattern of the energy deposition can also be exploited. Since the energy deposited by MIPs is related to the detector thickness, it is possible to correlate the energy collected in the inner and outer layers of the calorimeter.

The EC cuts for the low beam energy ND_3 runs during the Eg4 experiment are

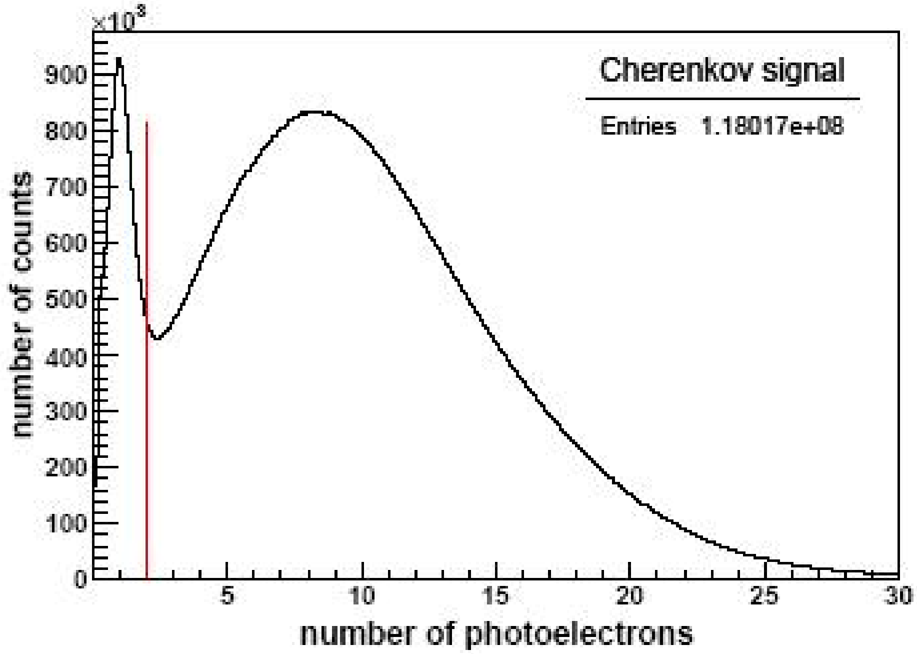

Figure 3.3: Sample Cerenkov counter signal showing the pion peak with a low CC photo electron signal and the cut applied at 2 photo electrons for electron selection.For the preliminary data analysis of Eg4 experiment, before pion contamination is studied closely, a relatively high cut was set to ensure the efficiency of electron identification.

determined to be:

$E_{tot}/p > 0.0177 * p + 0.16$

$E_{out}/p > -1.67 * E_{in}/p + 0.266$

Figure 3.4 shows the total energy deposited divided by momentum versus energy deposited on the inner layers of the calorimeter divided by momentum.

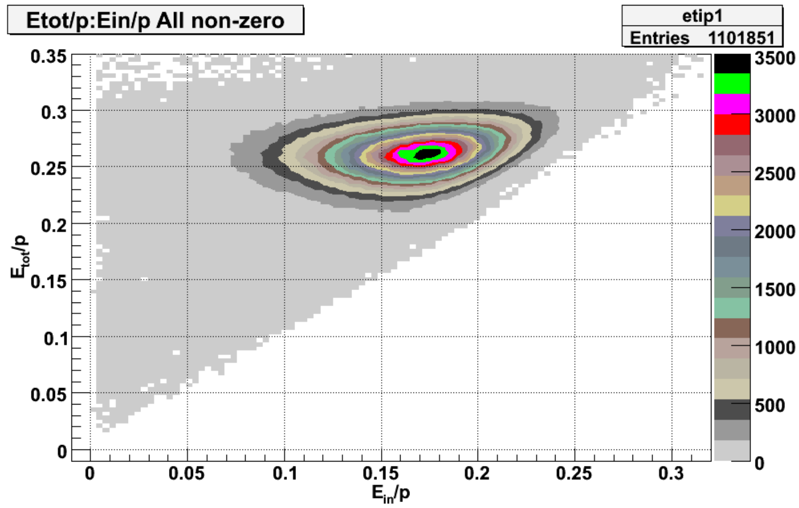

Figure 3.4: Total energy deposited divided by momentum versus energy deposited on the inner layers of the calorimeter divided by momentum

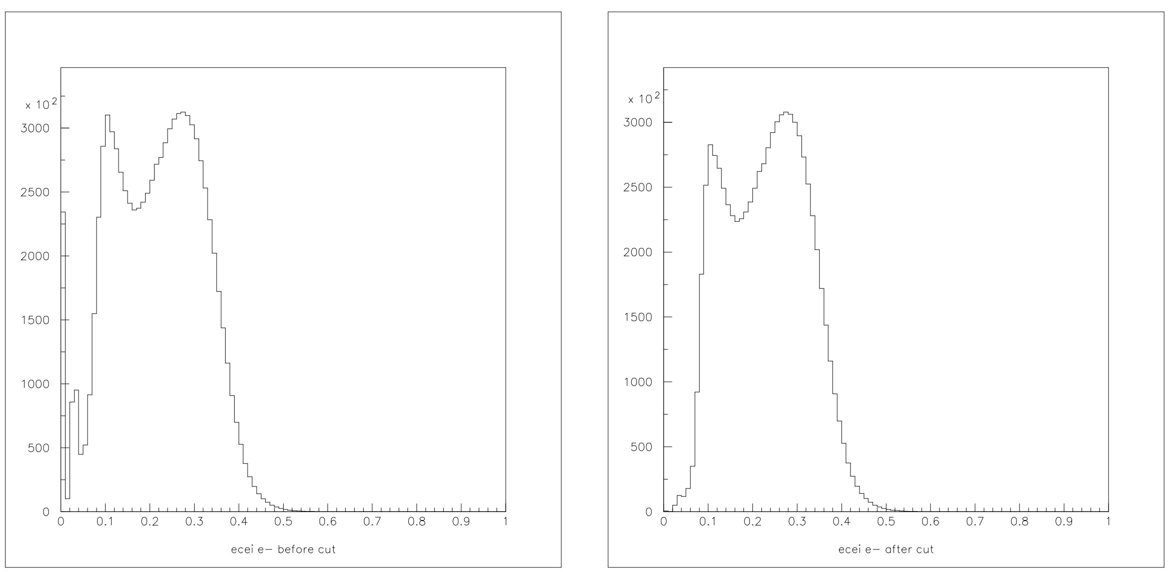

Figure 3.5: E_{in} after cuts

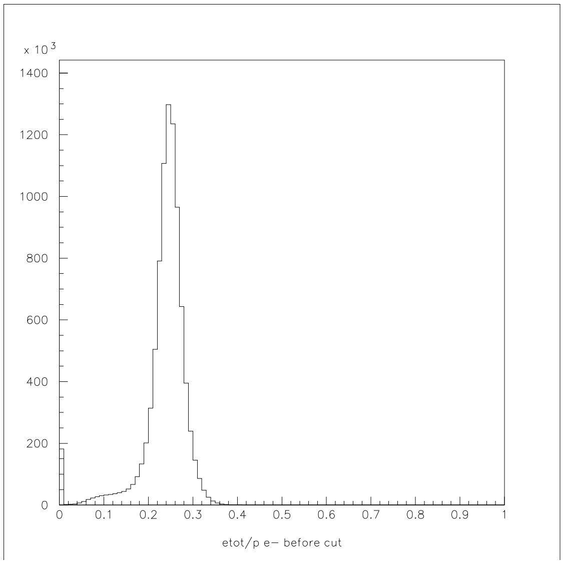

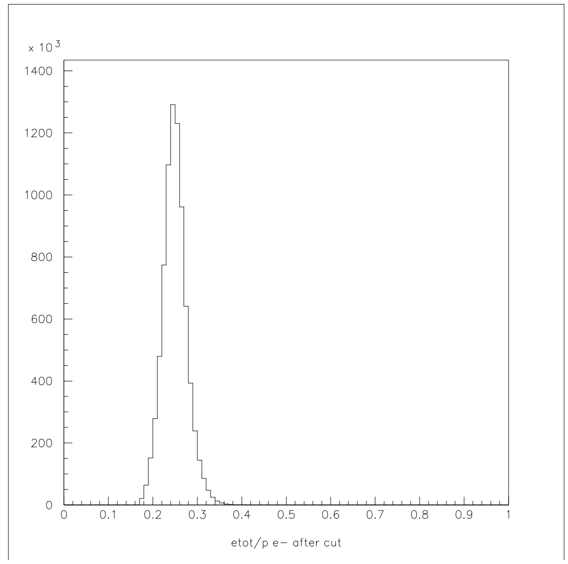

Figure 3.6: E_{tot}/p after cuts

Figure 3.5 and 3.6 shows the total energy divided by momentum and inside energy divided by momentum before and after the EC cuts. Pion contamination was successfully removed by the EC cuts.

3.8 CC Fiducial Cuts

The Cerenkov detector contains some regions of acceptance inefficiency. These inefficiencies are caused by problems in different parts of the detector. In order to avoid systematic offsets the contribution from the inefficient regions in the Cerenkov Counter needs to be excluded from our electron selection. There is a certain combination of polar and azimuthal angles for which Cerenkov PMTs do not receive light. If an electron hit in the calorimeter is close to one of those edges, part of the shower's

Line Color	Analytic Expression
Purple	$\varphi > 0, \theta > (\varphi/8)^2 + 15.8;$
	$\varphi < 0, \theta > (\varphi/7)^2 + 15.8$
Red	$\theta > 15.8$
Blue	$\varphi > 0, \theta > (\varphi/15.78)^2 + 15.8;$
	$\varphi < 0, \theta > (\varphi/10.95)^2 + 15.8$
Green	$0 < \varphi \leq 5, \theta > 15.8;$
	$\varphi > 5, \theta > (\varphi/15.78)^2 + 15.8;$
	$-3.5 < \varphi < 0, \theta > 15.8;$
	$\varphi < -3.5, \theta > (\varphi/10.95)^2 + 15.8$

Table 3.1: Different choices of fiducial efficiency regions.

energy can leak and will not be fully reconstructed.

The fiducial cuts are geometrical and the fiducial region is defined in terms of polar and azimuthal angles. Figure 3.7 and Table 3.1 illustrates different choices of fiducial efficiency regions. Figure 3.8 shows the Cerenkov Counter photo electron distribution in θ and φ before and after the fiducial cuts were applied. For Eg4 analysis the region represented by the red line is used as fiducial cuts.

3.9 Momentum Correction

The particle's momentum given by the reconstruction code is known to show deviations from the expected value. When we plot the W histogram of selected electron events, we can see that the central value of the peak is slightly shifted from its theoretical value $W_{ela} = m_p = 0.9382$. The peak is also broader than expected from the intrinsic resolution of CLAS. This systematic shift depends on both the azimuthal

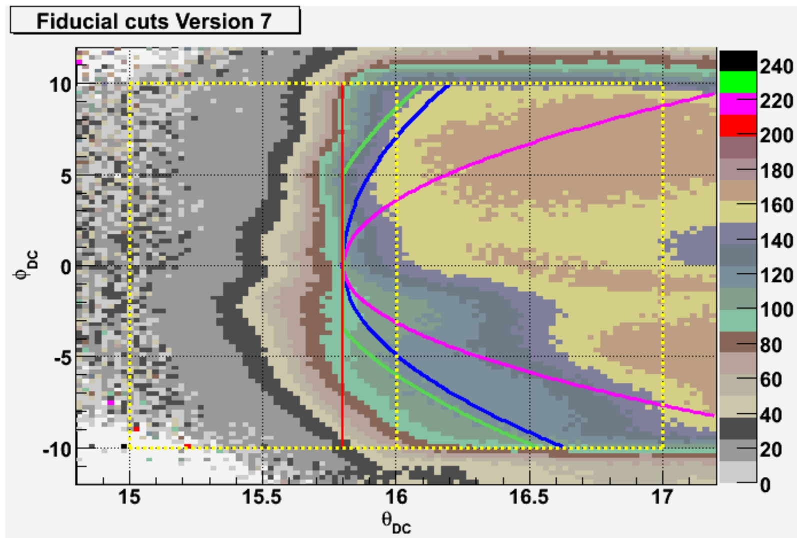

Figure 3.7: Fiducial region selection.

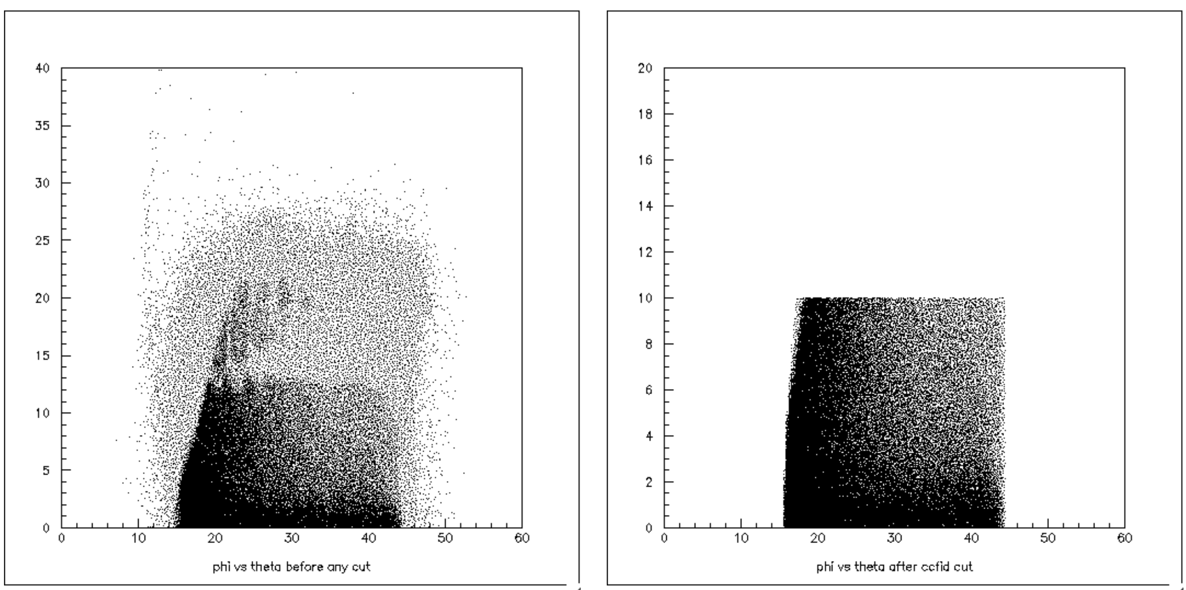

Figure 3.8: Photo electron distribution vs θ_{DC} and φ_{DC} (φ is the horizontal azimuthal angle measured on the XY plane and θ is the vertical azimuthal angle measured from the z axis) before and after fiducial cuts.

and polar angles, it is caused by the inaccurate or incomplete knowledge of the magnetic field and the drift chamber positions. A correction code is developed by S. Kuhn, X. Zheng and A. Krishna [37]. The authors assume that both momenta and the polar angles are systematically affected by the displacement of the drift chambers from their nominal positions and by the magnetic field deviation from the field map used in the reconstruction code.

As shown in the following euqations, eleven parameters are used to construct the corrected particle momenta:

$$\Delta p/p = ((B_1 + B_2\varphi)cos\theta/cos\varphi + (B_3 + B_4\varphi)sin\theta p/(qB_{torus})+$$
$$(B_5cos\theta + B_6sin\theta) + (B7cos\theta + B_8sin\theta))\varphi + 0.02 * (B_9 + (B_{10} + B_{11}\varphi/30) * (\tfrac{10}{\theta})^3);$$
$$p_{corr} = p + \delta p;$$
$$E_{corr} = \sqrt{p_{corr}^2 + m} + 0.0028;$$
$$p_{corr} = \sqrt{E^2 - m}$$

Where m is the electron mass and the energy correction constant 0.0028 accounts for the outgoing energy loss for specific incoming beam energies.

Figure 3.9 shows the effect of momentum correction on the invariant mass W distribution for a proton target run. From the histogram plot we can clearly see that the momentum correction slightly shifted the central peak value of W and improved the W peak resolution.

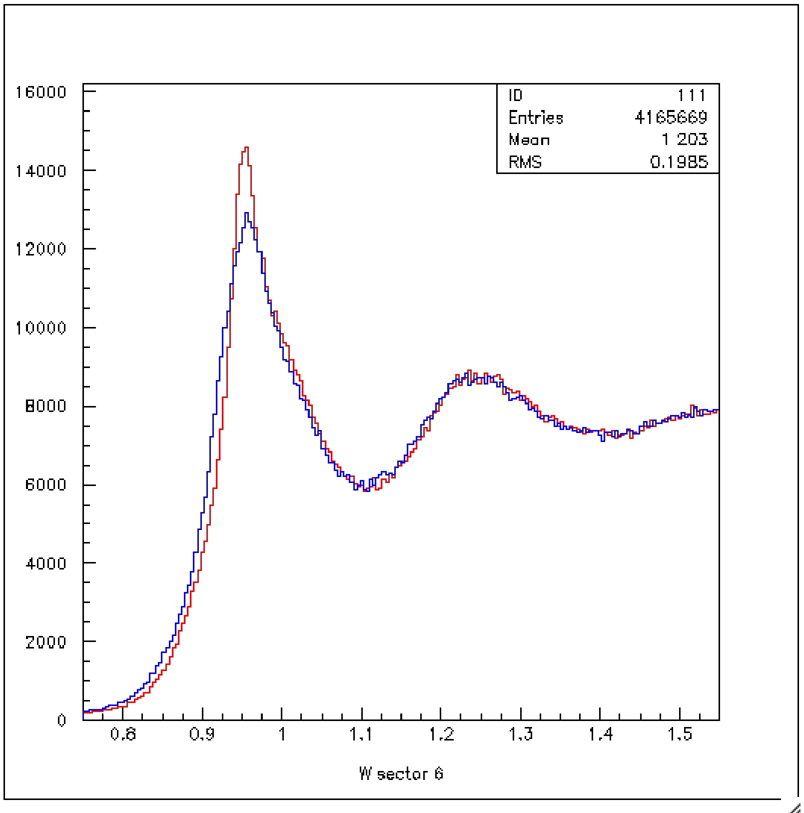

Figure 3.9: W histogram of a 3 GeV NH_3 golden run. The blue line represents W distribution before the momentum correction, while red line represents the distribution after the correction.

3.10 Raster Correction

During the experiment, the beam was rastered in a spiral pattern to avoid overheating and differential radiation damage of the local regions in the target. The raster is designed to sweep equal amount of area in the unit time. This was done using two magnets located upstream of the target. The values of the current going through the magnets are recorded by ADCs, and passed into the data stream. These ADC values are later translated into actual beam positions in (x,y).

Corrections are made to the tracking, which allows for better vertex reconstruction before the vertex cuts are applied. S. Kuhn, A. Krishna and X. Zheng developed the raster and vertex correction for the Eg4 experiment.

Figure 3.10 and 3.11 show the effect of raster and vertex correction on the z-vertex distribution for the cases of empty cell target with or without helium. The corrected z-vertex distribution has much better peak resolution than before.

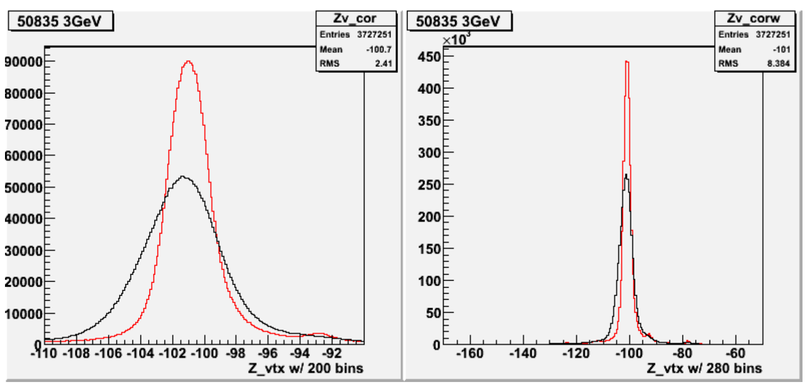

Figure 3.10: Raster and vertex correction on z-vertex distribution for empty target cell with helium. Red line represents vertex distribution after correction and the black line represents vertex distribution before the correction.

3.11 Faraday Cup Correction

Since we use measurements with different targets to determine the background, it is important that the Faraday Cup efficiency is independent of the target used. However, due to multiple scattering there was some loss of beam from the Faraday Cup,

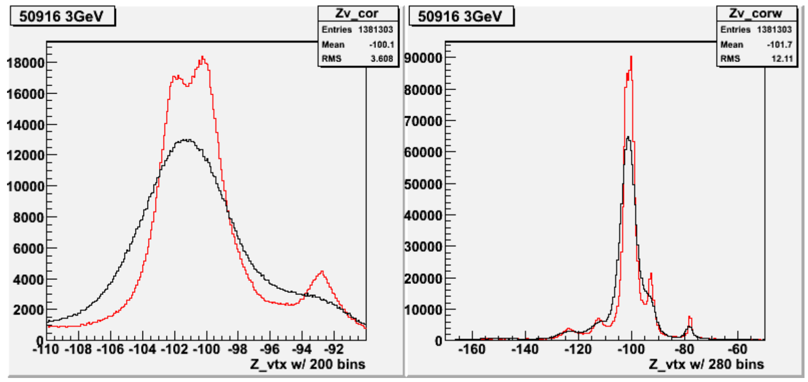

Figure 3.11: Raster and vertex correction on z-vertex distribution for empty target cell without helium. Red line represents vertex distribution after correction and the black line represents vertex distribution before the correction.

particularly at low beam energies. More beam is lost with the solid targets than with the empty ones. Therefore, a correction factor is needed to make the counts from different targets compatible.

During the EG4 experiment, the Faraday Cup and the three Beam Current Monitors (BCM) were used to measure the beam current. A combination of the multiple scattering between electrons and the target material and the electron trajectory shift caused by the target magnetic field led to a certain amount of beam loss on the Faraday Cup which was located behind the target section. Since the BCMs were located before the target cell, we can use the BCM readings to calibrate the Fcup readings in order to get a more accurate total charge for the cross section calculation.

A reconstruction code was developed to extract the ratio between the Fcup and the BCM readings for different target materials at various beam energies, thus calibrations for beam loss on Fcup were obtained for different target types and beam energies.

Table **??** shows the result of Fcup/BPM ratio for different target types at different incoming beam energies. The following table ?? shows the target type corresponding to the target index in Figure 3.12, 3.13, 3.14 and 3.15.

run number	fcup/c2c21a	fcup/c2c24a	fcup/c2h01a
50836(3Gev, empty/He)	0.990(0.01136)	1.003(0.01603)	0.9968(0.0058)
51046(2.3GeV,long NH3)	0.9842(0.027)	0.9795(0.027)	0.9777(0.095)
51049(2.3GeV,empty/no He)	0.9926(0.037)	1.004(0.042)	0.9867(0.038)
51073(2.3GeV,short NH3)	0.999(0.011)	1.003(0.016)	0.9968(0.058)
51081(2.3GeV, short C)	0.9904(0.0254)	0.9900(0.0223)	0.9767(0.071)
51180(1.3GeV,long NH3)	0.7435(0.1293)	0.7279(0.1262)	0.7255(0.1502)
51272(1.3GeV,long C)	0.8172(0.0208)	0.7921(0.022)	0.8088(0.0127)
51273(1.3GeV,empty/He)	0.9963(0.434)	0.9828(0.7626)	1.056(1.282)
51277(1.3GeV,long C/no He)	0.8430(0.022)	0.8357(0.021)	0.8391(0.013)

Table 3.2: Result of Fcup/BCM ratio for different target types at different incoming beam energies.

index	target type
1	empty target
2	empty target with helium
3	short carbon without helium
4	short carbon with helium
5	long carbon target
6	short NH_3 without helium
7	short NH_3 with helium
8	long NH_3 target

Table 3.3: target type index

Figure 3.12, 3.13, 3.14 and 3.15 shows the Fcup/BCM ratio from empty to solid target in different beam energies. We can see that the Faraday Cup beam loss was

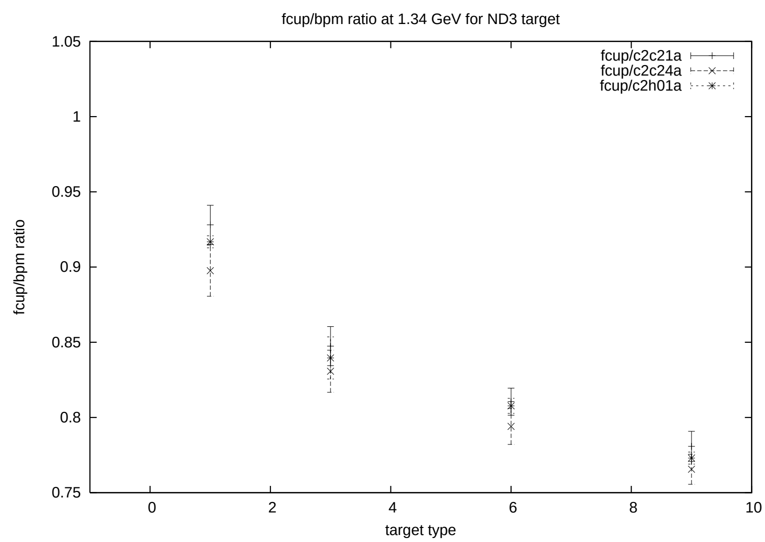

Figure 3.12: Fcup/BPM ratio for different target types. The x axis is the target index, which increases from empty to solid targets.1. empty target, 2. empty with helium, 3. short carbon without helium 4. carbon with helium, 5. long carbon target, 6. short NH_3 without helium, 7. short NH_3 target with helium, 8. long NH_3 target.

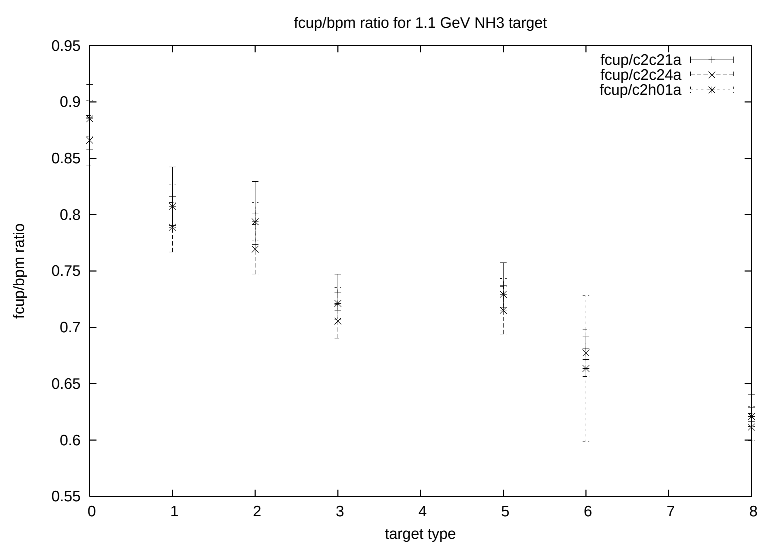

Figure 3.13: Fcup/BCM ratio for different target types. The x axis is the target index, which increases from empty to solid targets.

more significant for solid targets, and at lower beam energies.

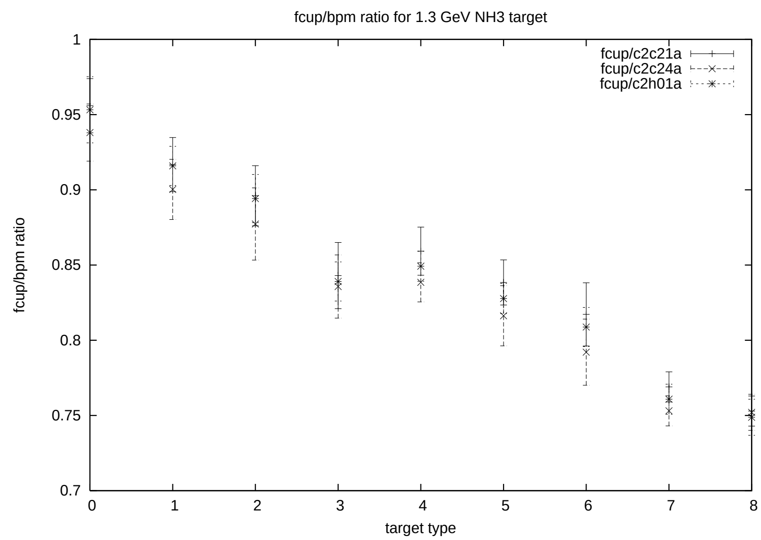

Figure 3.14: Fcup/BCM ratio for different target types. The x axis is the target index, which increases from empty to solid targets.

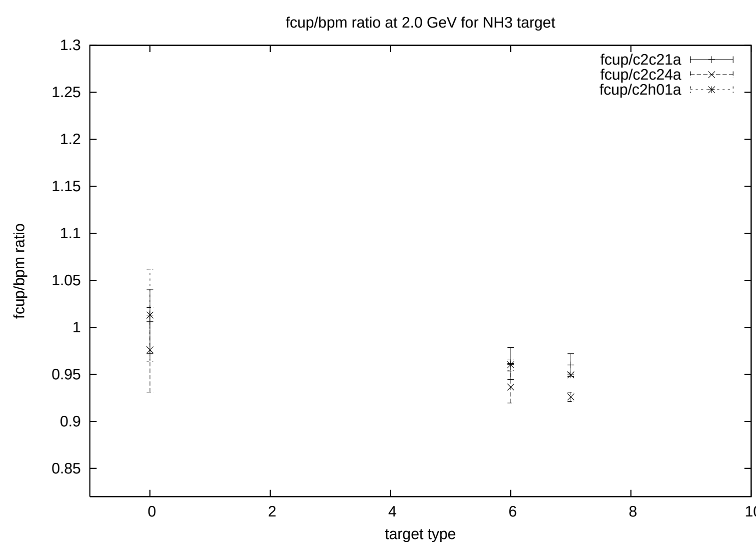

Figure 3.15: Fcup/BCM ratio for different target types. The x axis is the target index, which increases from empty to solid targets.

Chapter 4

Data Analysis

4.1 Beam and Target Polarization

The target polarization during the Eg4 experiment was monitored by a Nuclear Magnetic Resonance (NMR) system. The basic mechanism of an NMR system has been introduced in the chapter of Experimental Setup.

Since ND_3 is a spin 1 particle, in an external magnetic field it has 3 magnetic substates. The deuteron has a significant quadrupole moment which couples to the electric field gradient created from the atomic electrons in the ND_3 lattice to distort the Zeeman states. The energy spacing between the 3 states is therefore not uniform and there are two NMR transitions with two different frequencies. The two peaks correspond to these two frequencies as shown in Figure 4.1.

During the experiment, the target polarization was measured using the Q-meter technique. The Q-meter measures the voltage and corresponding power loss or gain due to the induced nuclear spin transitions. The technique makes use of the change in magnetic susceptibility of the material.

The Q-meter is designed to measure the voltage change across the circuit as a function of the input frequency. The circuit is powered by a generator which sweeps the rf-frequency through the Larmor frequency of the target. The complex output voltage $V(\omega, \chi)$ is read from the diode output of the circuitit. This output contains both dispersive and absorptive parts, so in order to isolate the absorptive part, the signal passes through a phase detector called the Balanced Ring Modulator(BRM). The phase detector compares the input rf signal and the output signal, and the phase between the two is set to zero by varying the length of an adjustable piece of cable from the generator to the BPM. After the real part of the voltage is selected, it contains $\chi'\prime$ and the so-called Q-curve, which is a background measurement of the Q-meter response to the input frequency away from the resonance. The background Q-curve is subtracted from the resonant signal.

The baseline subtraction can be inaccurate for various reasons. In order to correct for it, a polynomial fit is made to the edges of the signal and subtracted. The result of these two subtractions is a so-called poly-subtracted signal. In order to calibrate the system, the baseline was measured frequently during the target polarization measurements so that it is updated with the current situations of the target chamber(temperature, magnetic field, target annealing, etc.). Figure 4.1 shows the deuteron target NMR signal after the baseline subtraction.

Two methods are commonly used in measuring deuteron polarization: the area method and the ratio method.

In the area method, the dynamic polarization P was derived as the ratio of the enhanced absorption signal area to that of the thermal equilibrium signal

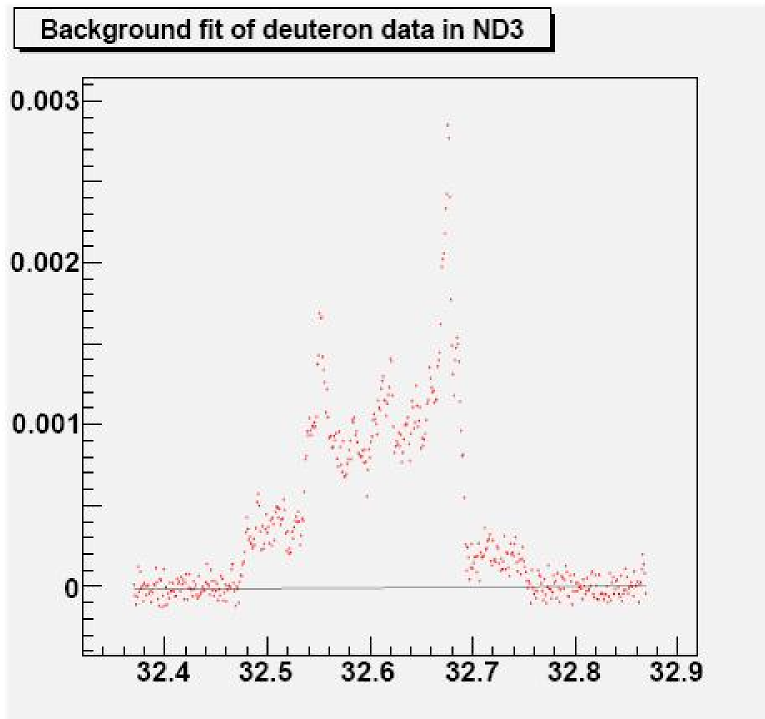

Figure 4.1: NMR signal for deuteron polarization. The X-axis is the frequency in MHz, while the Y-axis is an arbitrary scale proportional to the output voltage of the Q-meter, thus illustrating the target polarization.

$$P = \frac{\int S_{enh}(\omega)d\omega}{\int S_{TE}(\omega)d\omega} \cdot P_{TE} \tag{4.1.1}$$

where the TE polarization for a spin 1 particle at a given temperature and magnetic field can be calculated from the equation:

$$P_{TE} = \frac{4tanh(\frac{\hbar\omega_0}{2kT})}{3 + tanh^2(\frac{\hbar\omega_0}{2kT})} \tag{4.1.2}$$

where k is the Boltzmann constant and ω_0 the Larmor frequency.

However, in the Eg4 experiment, the TE signal for the deuteron target was not measurable due to the large background noise and comparatively too small of a polarization signal. Therefore, we adopted the ratio method to determine the deuteron polarization.

The approximate relation between the peak ratio r and the target polarization can be described as follows [38]:

$$P_r = \frac{r^2 - 1}{r^2 + r + 1} \tag{4.1.3}$$

When the quadrupolar coupling is weak, as is the case of Eg4 experiment, this equation is a good approximation of the relation between the deuteron polarization and the peak heights ratio. The meaning of r can be seen in Figure 4.3.

Using a program that fits the NMR signal from the theoretical deuteron target lineshape function, we can extract the peak ratio and calculate the polarization. Figure 4.2 is the fitting to the NMR signal and Figure 4.3 shows the process of extracting the peak ratio r. The y axis is the voltage change across the circuit of the Q-meter and the x axis is the frequency in the unit of MHz.

$r = h_1/h_2$, where h_1 and h_2 are the distance from each peak to the tangential line of its shoulder.

The experimental data I worked on are the NMR signals for ND_3 polarization during the time span of approximately one month: April 2006. In order to automate the calculation of the polarization values for all the runs during this time, we need a calibration constant, CC, which is defined to be the ratio between the polarization value, P_r, and the area, A, covered by the NMR signal line.

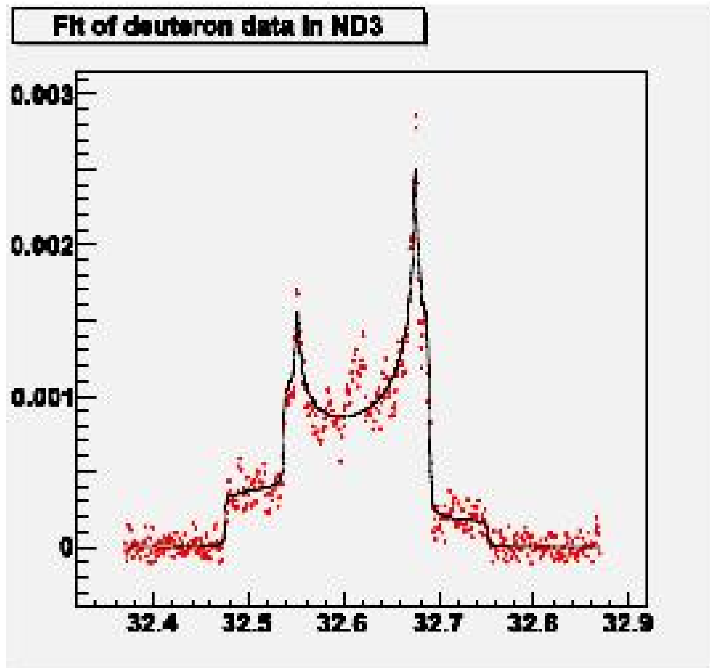

Figure 4.2: Fitting of the enhanced ND_3 NMR signal. The X-axis is the frequency in MHz, while the Y-axis is an arbitrary scale proportional to the output voltage of the Q-meter, thus illustrating the target polarimetry.

$$CC = P_r/A \tag{4.1.4}$$

Once we obtained this value, we could multiply CC by the area of each measurement and automate the results of P_r for each measurement during April 2006.

Theoretically, the value of CC should be a constant for all the runs during the month of April, but in practice it depends on various conditions of the target (size, position, radiation centers and etc.) All the runs in April were classified into two periods, the first one from April 5th to April 19th, the second one from April 20th

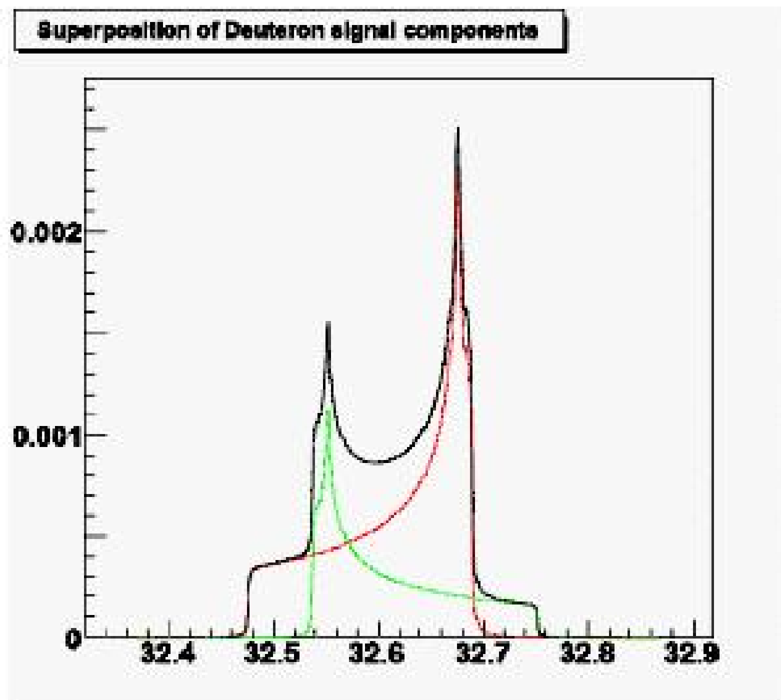

Figure 4.3: Extraction of the peak ratio r. $r = h_1/h_2$,where h_1 and h_2 are the distance from each peak to the tangential line of its shoulder. The X-axis is the frequency in MHz, while the Y-axis is an arbitrary scale proportional to the output voltage of the Q-meter.

to April 30th. Each polarization period has its own value of CC. The reason for this is because there was a helium liquifier outage between April 18-21 which resulted in the target material being removed and later replaced. We should expect some fluctuations in the value of CC associated with this change.

After a close study in the polarization history in April 2006 in Hall B, it appeared that the polarization on April 25th is most stable compared to other days. The ratio method program processed over 92 runs from the day of April 25th to obtain CC value for the latter period:

$CC = 219.874 \pm 10.78$. The CC value for the earlier period was obtained similarly; $CC = 193.245 \pm 9.56$

Figure 4.4 is the polarization timeline in April, automated using the ratio method and the two calibration constants above. It is known from past experiences that radiating and annealing gives a steady increase in the beginning part of the ND_3 target polarization. The big sharp drops in the plot corresponds to the annealing process while the small drops are due to the adjustment of the microwave frequency. We exposed the target to an intense electron beam to create the irradiation damage and then raised the temperature to $\sim$ 100K for the annealing process.

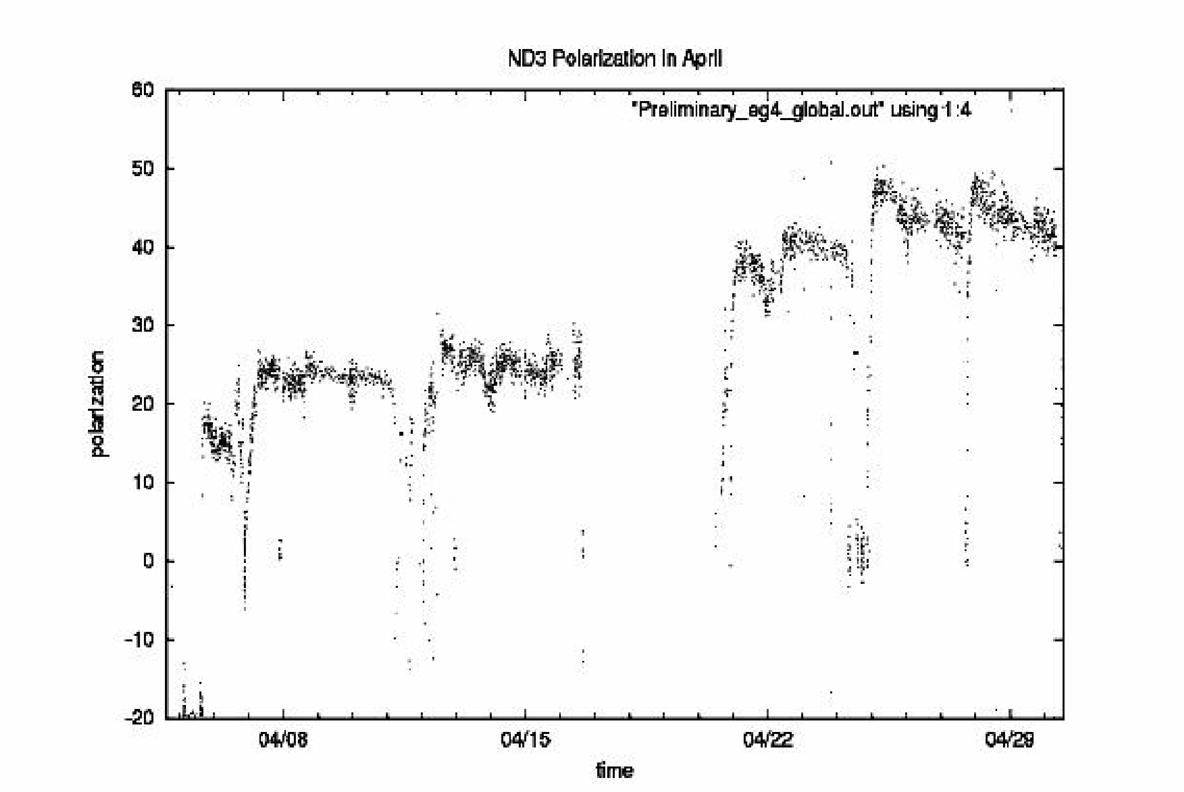

Figure 4.4: ND_3 Polarization as a function of time during April 2006 as obtained by ratio method.

In order to test the stability of the ratio method, we applied the polarization data from the G_E^n experiment (EG3026) that took place in 2001 in Hall C at the Jefferson Lab and compared our ratio results obtained by the area method to this experiment. Figure 4.5 show the comparison between the polarization measured by the ratio method and polarization measured by the area method.

As we can see, the ratio method has its limitation at the low polarization range. Polarization values calculated by the ratio method are always too high compared to that of the area method. This is due to the fact that in the polarizing process there is a difference in the transition rates driving the two peaks, therefore resulting in a false reading from the peak ratio method. But when the polarization gets above 25%, the two methods started to agree well with each other.

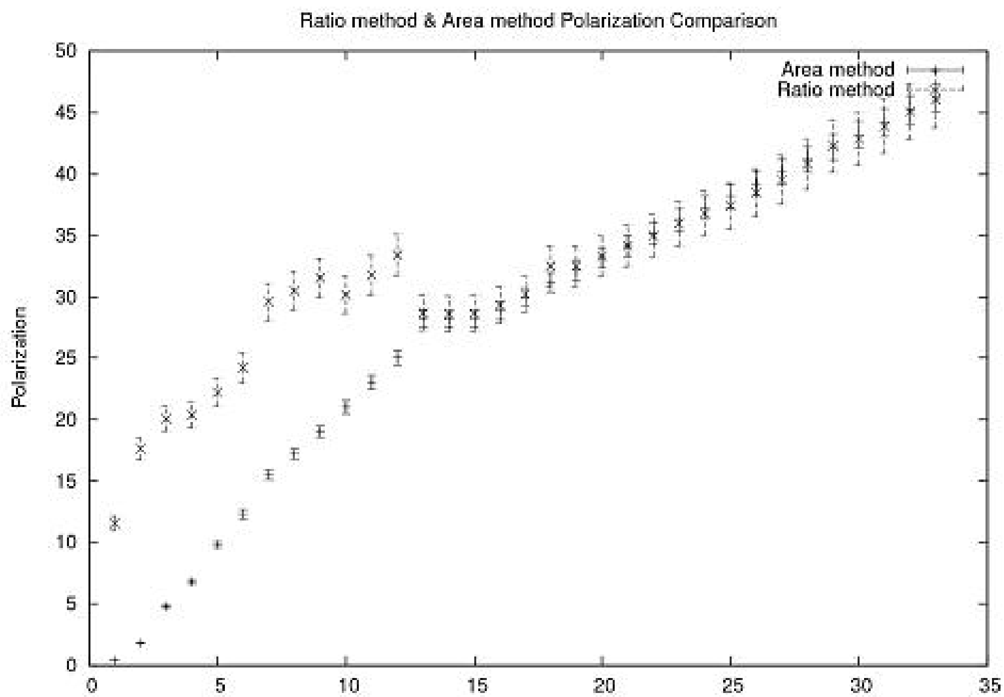

Figure 4.5: Results comparison between the area method and the peak ratio method using the G_E^n experimental data.

4.2 Electron Asymmetry

The raw electron scattering asymmetry can be expressed in terms of the number of counts:

$$A_{exp} = \frac{n\uparrow/fc\uparrow - n\downarrow/fc\downarrow}{n\uparrow/fc\uparrow + n\downarrow/fc\downarrow}, \tag{4.2.1}$$

where $n \uparrow /f_c \uparrow$ ($n \downarrow /f_c \downarrow$) is the number of number of electrons with the spin up(down), normalized to the number of incident electrons with the spin up(down), given by the Faraday cup readings.

$$A_{exp} = \frac{2}{(n\uparrow/fc\uparrow + n\downarrow/fc\downarrow)^2}\left[\frac{n\uparrow}{(fc\uparrow)^2}n\downarrow^2 + \frac{n\downarrow}{(fc\downarrow)^2}n\uparrow^2\right]^{\frac{1}{2}} \tag{4.2.2}$$

The resulting asymmetry is binned in Q^2 and W bins. Table 4.1 gives the list of the standard Q^2 bins.

Figure 4.7 to 4.15 shows the W distribution of the electron scattering asymmetry ($A_{\parallel}$ with approximated dilution factor) for various Q^2 bins at the incoming beam energy 1.99 GeV and 1.34 GeV. The plots show an elastic peak and a quasi-elastic delta peak, the positions of which are consistent with Figure 4.6, the W distribution of the helicity counts of the scattered electrons.

These plots are made with approximated dilution factors. In the following section, we will discuss the analysis of the dilution factor.

bin number	minimum value (GeV^2)	average value	maximum value
1	0.0092	0.0101	0.0110
2	0.0110	0.0120	0.0131
3	0.0131	0.0144	0.0156
4	0.0156	0.0171	0.0187
5	0.0187	0.0205	0.0223
6	0.0223	0.0244	0.0266
7	0.0266	0.0292	0.0317
8	0.0317	0.0348	0.0379
9	0.0379	0.0416	0.0452
10	0.0452	0.0496	0.0540
11	0.0540	0.0592	0.0645
12	0.0645	0.0707	0.0770
13	0.0770	0.0844	0.0919
14	0.0920	0.1010	0.1100
15	0.1100	0.1200	0.1310
16	0.1310	0.1440	0.1560
17	0.1560	0.1710	0.1870
18	0.1870	0.2050	0.2230
19	0.2230	0.2440	0.2660
20	0.2660	0.2920	0.3170
21	0.3170	0.3480	0.3790
22	0.3790	0.4160	0.4520
23	0.4520	0.4960	0.5400
24	0.5400	0.5920	0.6450
25	0.6450	0.7070	0.7700
26	0.7700	0.8440	0.9190
27	0.9200	1.0100	1.1000
28	1.1000	1.2000	1.3100
29	1.3100	1.4400	1.5600
30	1.5600	1.7100	1.8700
31	1.8700	2.0500	2.2300
32	2.2300	2.4400	2.6600
33	2.6600	2.9200	3.1700
34	3.1700	3.4800	3.7900
35	3.7900	4.1600	4.5200
36	4.5200	4.9600	5.4000
37	5.4000	5.9200	6.4500
38	6.4500	7.0700	7.7000
39	7.7000	8.4400	9.1900
40	9.1900	9.6400	10.100

Table 4.1: List of Q^2 bins used in Eg4.

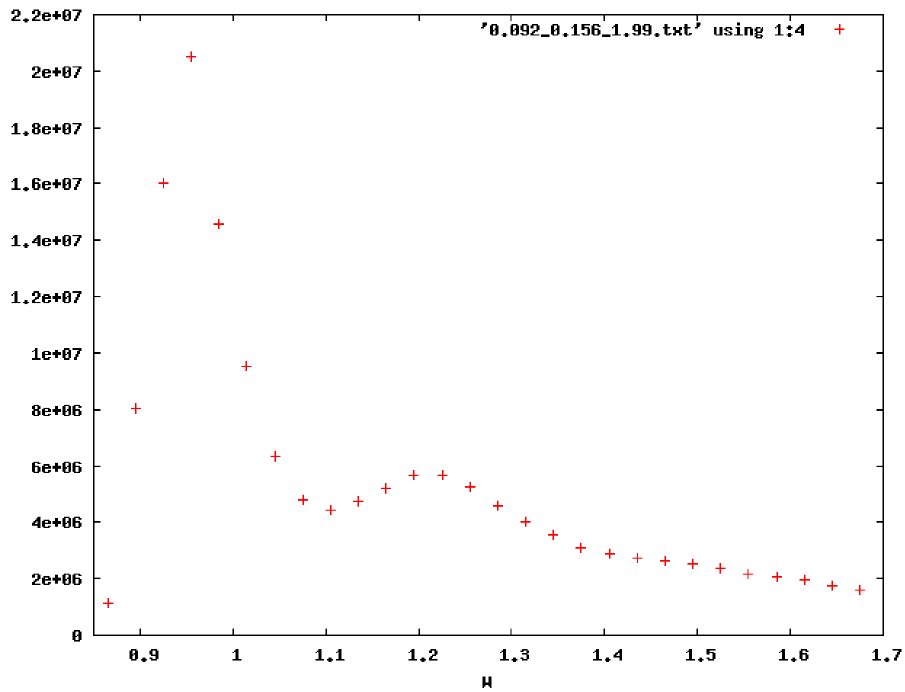

Figure 4.6: Counts vs W at $E_{in} = 1.99$ GeV, ND_3 target.

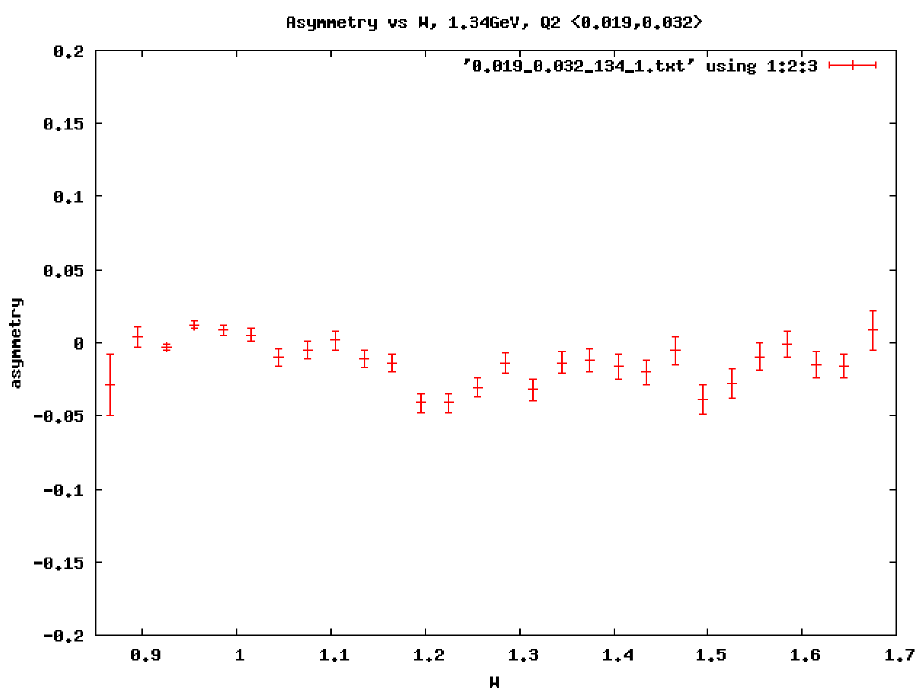

Figure 4.7: $A_{\parallel}$ vs W at $E_{in} = 1.34$ GeV, Q^2 $(0.019, 0.032) GeV^2$ ND_3 target.

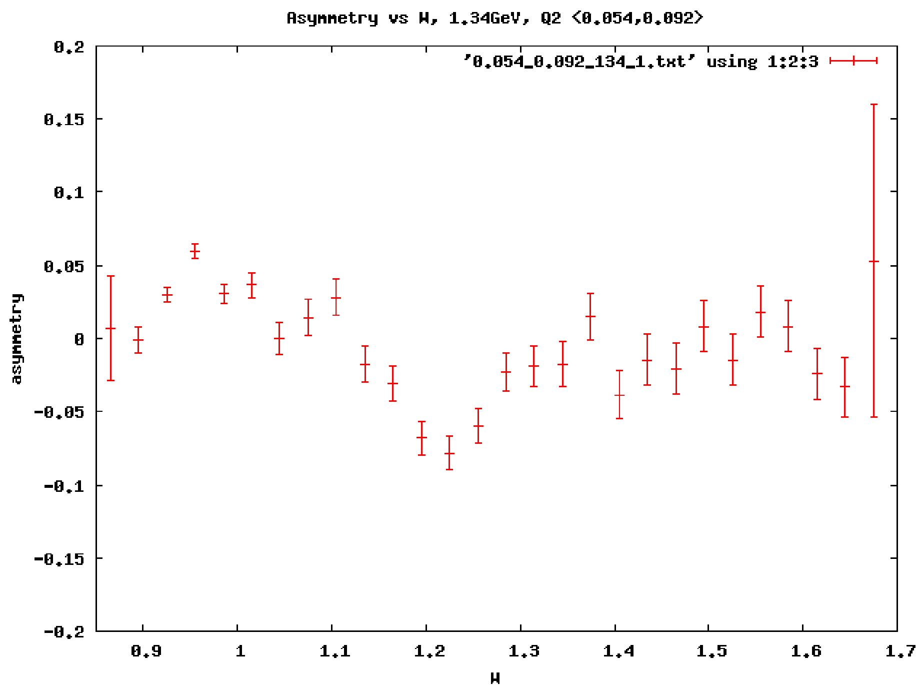

Figure 4.8: $A_{\shortparallel}$ vs W at E_{in} = 1.34 GeV, Q^2 $(0.054, 0.092)GeV^2$ ND_3 target.

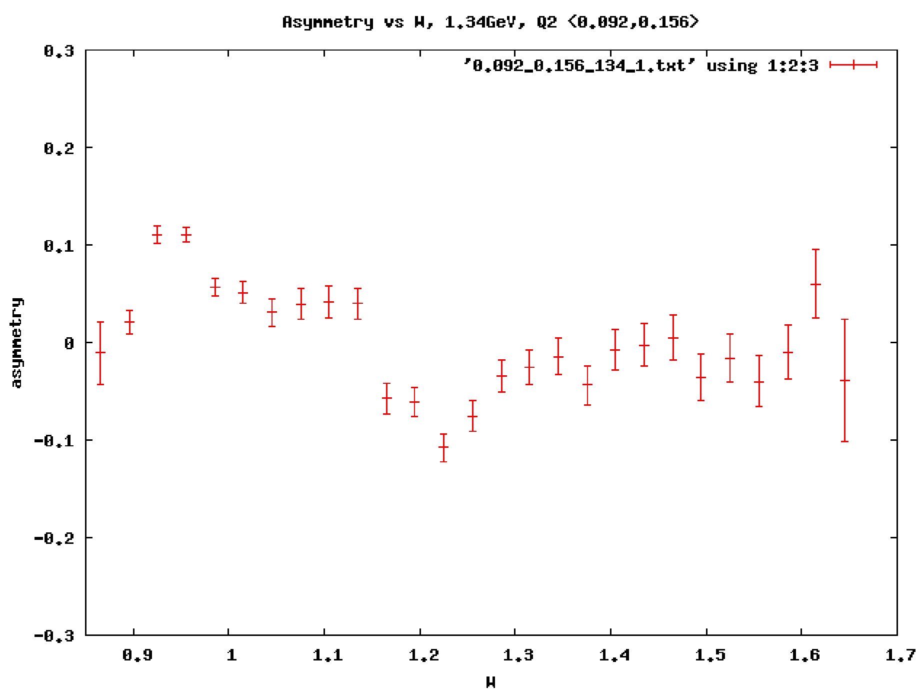

Figure 4.9: $A_{\shortparallel}$ vs W at E_{in} = 1.34 GeV, Q^2 $(0.092, 0.156)GeV^2$ ND_3 target.

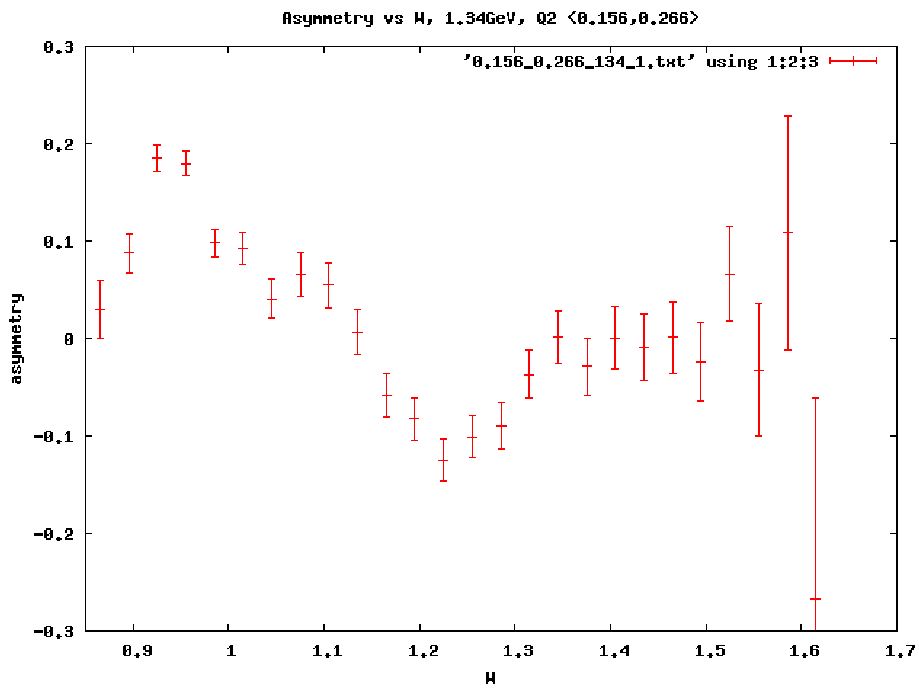

Figure 4.10: $A_{\shortparallel}$ vs W at $E_{in} = 1.34$ GeV, Q^2 $(0.156, 0.266) GeV^2$ ND_3 target.

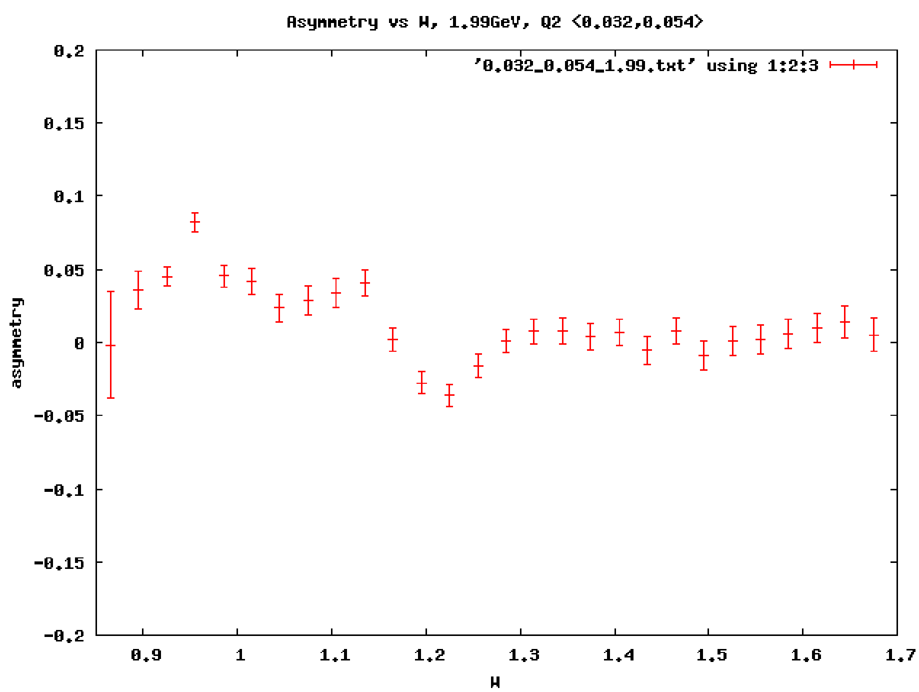

Figure 4.11: $A_{\shortparallel}$ vs W at $E_{in} = 1.99$ GeV, Q^2 $(0.032, 0.054) GeV^2$ ND_3 target.

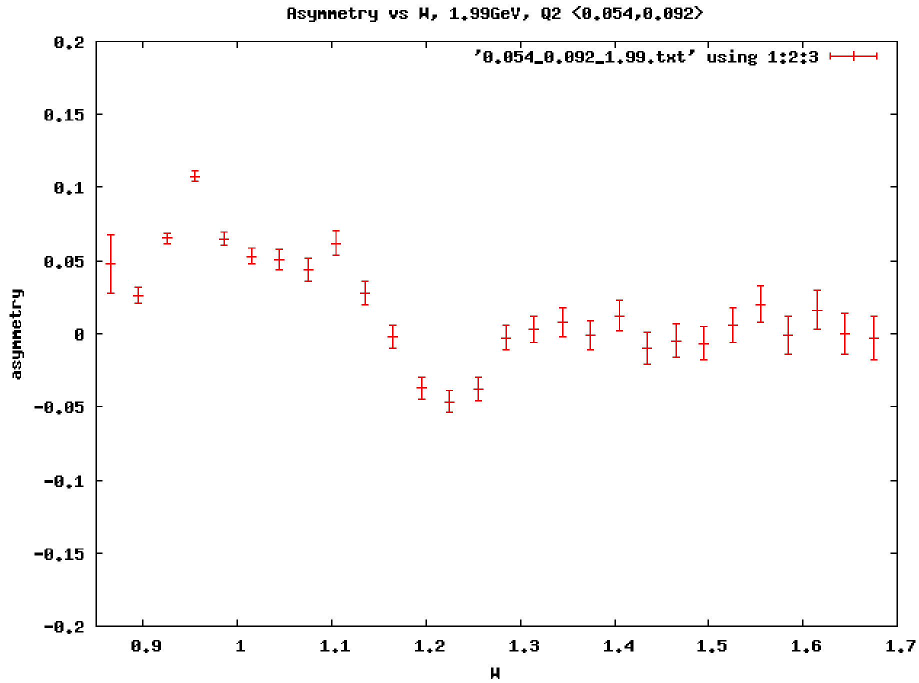

Figure 4.12: $A_{\parallel}$ vs W at $E_{in} = 1.99$ GeV, Q^2 $(0.054, 0.092) GeV^2$ ND_3 target.

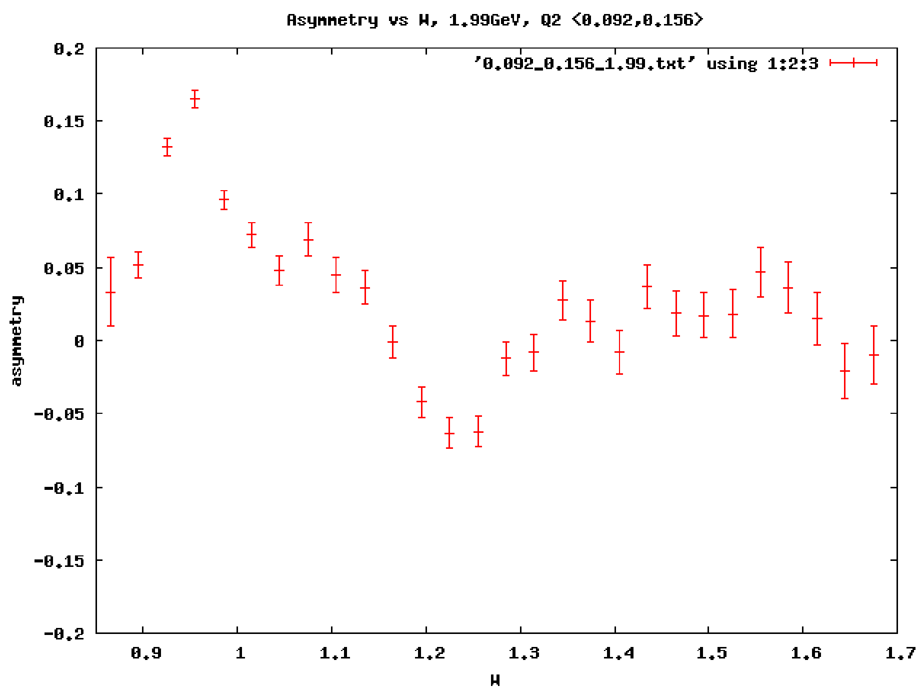

Figure 4.13: $A_{\parallel}$ vs W at $E_{in} = 1.99$ GeV, Q^2 $(0.092, 0.156) GeV^2$ ND_3 target.

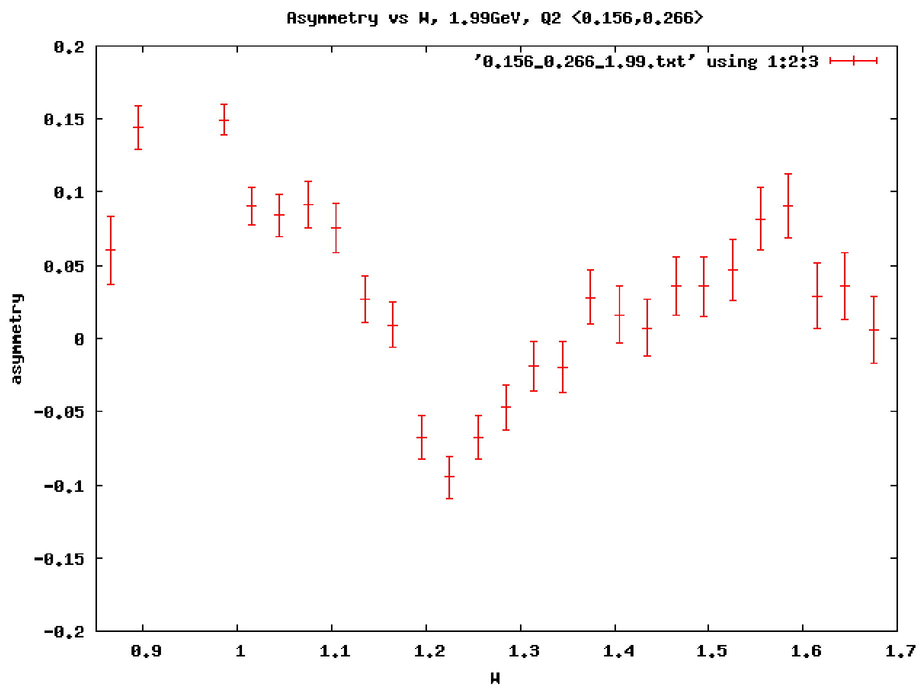

Figure 4.14: $A_{\parallel}$ vs W at E_{in} = 1.99 GeV, Q^2 $(0.156, 0.266)GeV^2$ ND_3 target.

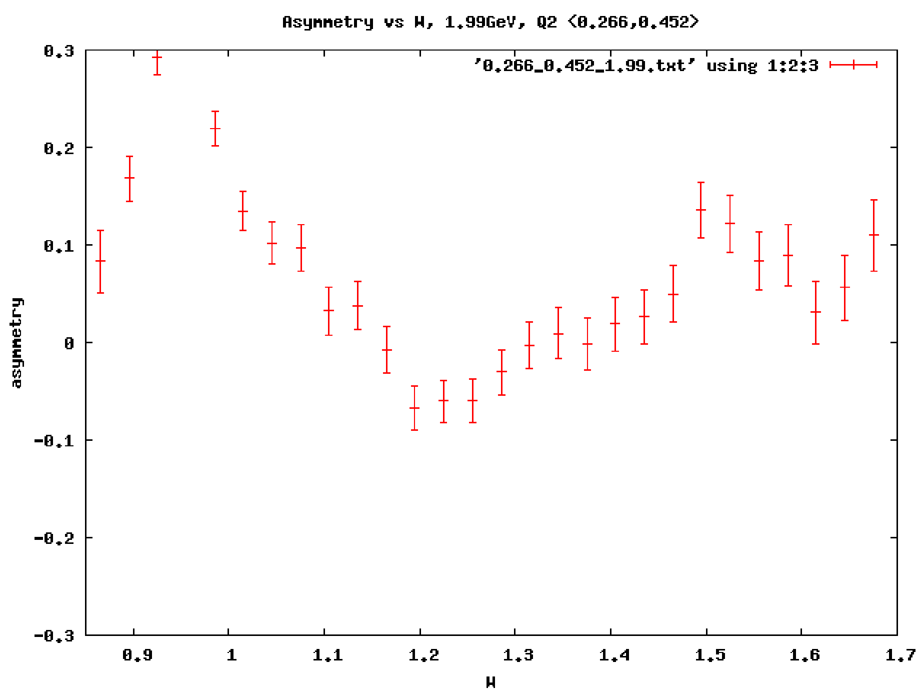

Figure 4.15: $A_{\parallel}$ vs W at E_{in} = 1.99 GeV, Q^2 $(0.266, 0.452)GeV^2$ ND_3 target.

4.3 Dilution Factor

The measured asymmetry is formed by electrons scattered off the polarized deuterons in ND_3, the N nucleus, liquid helium bath and target windows. To obtain asymmetry for polarized electrons scattering off polarized deuterons, all other contributions need to estimated and removed from the data. The unpolarized background contributes to the denominator of the asymmetry, thereby "diluting" it. The undiluted asymmetry can be expressed as:

$$\begin{aligned} A_{undiluted} &= \frac{N^+/fc^+ - N^-/fc^-}{N^+/fc^+ + N^-/fc^- - background} \\ &= \frac{N^+/fc^+ - N^-/fc^-}{N^+/fc^+ + N^-/fc^-} * \frac{N^+/fc^+ + N^-/fc^-}{N^+/fc^+ + N^-/fc^- - b.g.} \\ &= A_{measured} * \frac{1}{DF} \end{aligned} \quad (4.3.1)$$

Thus the dilution factor can be extracted as:

$$DF = \frac{N^+/fc^+ + N^-/fc^- - background}{N^+/fc^+ + N^-/fc^-} \quad (4.3.2)$$

The background contribution is consisted of ^{15}N, ^4He and other materials located along the beam path and at the target surroundings. We can express the background contribution numerically as:

$$\begin{aligned} n_b &= n_N + n_{He} + n_{foils} \\ &= \rho_N l_N \sigma_N + \rho_{He}(L - l_{ND_3})\sigma_{He} + \rho_f l_f \sigma_f \end{aligned} \quad (4.3.3)$$

Parameter	Value	Remarks
$\rho_f l_f$	$0.169 g/cm^2$	within 10 cm from vertex cut
ρ_C	$2.17 g/cm^3$	density of carbon
l_C	$Thick: 0.216cm$	thickness of carbon target
$\rho_C l_C$	$Thick: 0.468 g/cm^2$	thickness times density for carbon
ρ_{He}	$0.1452 g/cm^3$	density of helium
L	$2.14cm$	Distance to the exit of the target chamber
ρ_A	$1.056 g/cm^3$	A = Ammonia ND_3
ρ_N	$0.513 g/cm^3$	Extracted from ρ_A
l_A	0.6 cm	packing fraction

Table 4.2: Dilution factor parameters for various material.

Here the number of counts is expressed in terms of density $(\rho, g/cm^3)$, length (l, cm) and cross section (σ, cm^2). The values of these parameters can be found in table 4.2:

The dilution factor analysis starts from calculating the cross section ratio between ^{15}N and C. The radiated cross section is obtained from an extrapolation of the Born cross section using the radiation length of the various target materials and the surroundings. The code for this method was developed by Peter Bosted. The contribution of ^{15}N can be expressed as:

$$n_N = \frac{\rho_N l_N}{\rho_C l_C}(\frac{\rho_N}{\rho_C})n'_C \tag{4.3.4}$$

where $n'_C = \rho_C l_C \sigma_C, l_A = l_N$. n'_C can be expressed completely by these following experimental results:

$$n_C = \rho_C l_C \sigma_C + \rho_{He}(L - l_C)\sigma_{He} + \rho_f l_f \sigma_f \tag{4.3.5}$$

$$n_{emp} = \rho_{He} L \sigma_{He} + \rho_f l_f \sigma_f$$

$$n_{ee} = \rho_f l_f \sigma_f$$

where n_{emp} means the number of counts from the empty target with ^4He and n_{ee} is the number of counts from the empty target without helium. n_C can be expressed in terms of n'_C, n_{emp} and n_{ee}:

$$n'_C = n_C - (1 - \frac{l_C}{L})n_{emp} - \frac{l_C}{L}n_{ee}. \tag{4.3.6}$$

Thus the total background contribution can be written as:

$$n_b = \frac{\rho_N l_A}{\rho_C l_C}(\frac{\sigma_N}{\sigma_C})n'_C + (1 - \frac{l_A}{L})n_{emp} + \frac{l_A}{L}n_{ee} \tag{4.3.7}$$

The dilution factor can therefore be extracted:

$$DF = \frac{n_A - n_b}{n_A} = 1 - \frac{n_b}{n_A} \tag{4.3.8}$$

where n_A is the number of counts from the ND_3 target. Figure 4.16 shows the dilution factor vs W for a certain Q^2 range.

4.4 $A_\parallel$ Comparison with Model

As we have discussed earlier, $A_\parallel$ can be derived from the experimental value as follows:

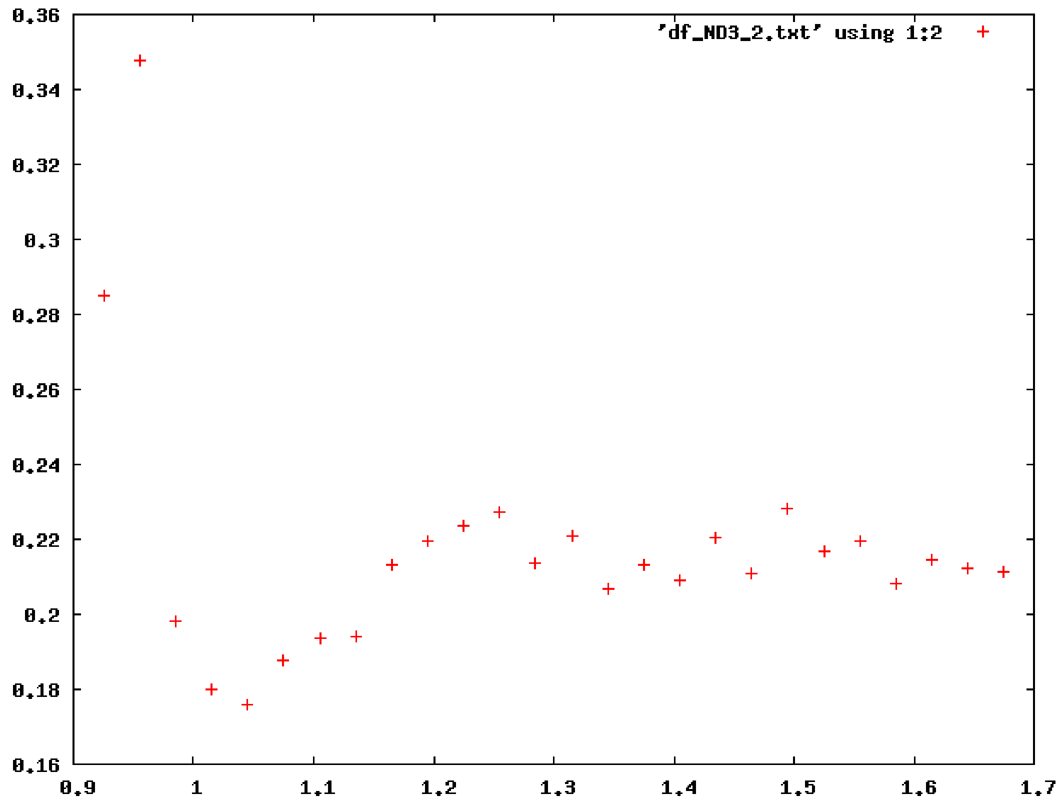

Figure 4.16: Distribution of dilution factor vs W for a certain Q^2 range, 1.99 GeV.

$$A_{\parallel} = \frac{A_{exp}}{P_b P_T * DF} \tag{4.4.1}$$

where P_b and P_T are the beam and target polarization and DF is the dilution factor.

Models for the desired virtual photon asymmetry A_1 and A_2 has been developed and fitted to world data from previous experiments. At the very low Q^2 region, we shall compare the $A_{\parallel}$ obtained from experimental data to that derived from the model. $A_{\parallel}$ can be expressed in terms of A_1 and A_2 as:

$$A_{\parallel} = D(A_1 + \eta A_2) \tag{4.4.2}$$

$$D = [1 - (1 - y)\epsilon]/(1 + \epsilon R) \tag{4.4.3}$$

$$y = \frac{\nu}{E} \tag{4.4.4}$$

$$R = \frac{\sigma_L}{\sigma_T} \tag{4.4.5}$$

$$\epsilon = [4(1 - y) - \gamma^2 y^2]/[2y^2 + 4(1 - y) + \gamma^2 y^2] \tag{4.4.6}$$

$$\eta = \epsilon\gamma y/[1 - \epsilon(1 - y)] \tag{4.4.7}$$

The comparison of $A_{\parallel}$ derived from the model and $A_{\parallel}$ calculated from experimental data will be shown and discussed in the final chapter.

4.5 Error Analysis

- Statistical Error

  The statistical error associated with the result of $A_{\parallel}$ is calculated from the number of electron counts detected in every Q^2 bin. The statistical error on the raw asymmetry A_{exp} is given by:

$$\Delta A_{exp} = \frac{2}{(n^+ + n^-)^2}\left[\frac{n^+}{fc^+}n^{-2} + \frac{n^-}{fc^-}n^{+2}\right]^{\frac{1}{2}} \tag{4.5.1}$$

where $n^+/fc^+(n^-/fc^-)$ is the number of electrons with spin up(down),normalized to the number of incident electrons with the spin up(down), given by the Faraday cup readings.

The dilution factor and target and beam polarization are considered to have only systematic errors. Thus the only source of statistical error comes from A_{exp}, and it propagates into the final $A_{\|}$ as:

$$\Delta A_{\|} = \Delta A_{exp} * \frac{1}{DF * P_b P_t} \tag{4.5.2}$$

- Systematic Error

  The systematic error of $A_{\|}$ consists of two parts, the dilution factor error ΔDF and the target polarization error P_t.

  The target polarization was obtained from the NMR signals. In order to measure the systematic error of the target polarization, we varied the baselines used in the NMR measurements and compared the difference in the result of calibration constant $CC = P_r/A$, where P_r is measured polarization from double peak method and A is the area covered by the NMR signal. Four different baselines taken on April 27, 2006 were selected. The result is shown by Table 4.3.

  As is shown the accuracy of the CC value decreased as the less recently updated baselines were used. Varying baselines that were taken around the time of most recent polarization signals provides a assessment of the stability of the fitting

Baseline	CC	difference
04-27-06T09:29AM	219.874	
04-27-06T11:26AM	218.984	0.4%
04-27-06T08:35PM	223.797	1.8%
04-27-06T03:59PM	213.773	2.7%

Table 4.3: Baselines used for NMR polarimetry.

program and the ratio method.

Chapter 5

Results and Conclusion

In the model for $A_{\parallel}$, the variables F_1,R and A_2 were not measured and had to be estimated from previous experiments. Thus a model outlined in Ref [39] is designed to provide quantities necessary for our analysis. The model parameterizes the measured world data, producing predictions for the unmeasured regions. The structure function $F_1(x, Q^2)$ is well known in DIS region and is extrapolated into the low Q^2 regime. The structure function $R(x, Q^2)$ is calculated using the SLAC/Whitlow fit, and is assumed to be constant below $Q^2 = 0.3$. In the resonance region, $F_1(x, Q^2)$ is obtained by using the most recent fit to the world data, and $R(x, Q^2)$ is obtained by using the Whitlow fit. [39] It is assumed to be zero in the resonance region.

The photon-nucleon asymmetry A_1 is fit to the world data in the DIS region as a function of variable ξ defined above. The fit uses data from E80, E130, E143, E155, EMC and SMC [5, 40] experiments. In the resonance region, A_1 is parametrized using two ingredients: an extrapolation of the DIS fit as function of x and Q^2, and the output from the analysis code. The second photon-nucleon asymmetry A_2 was not measured by the EG4 experiment. It is extrapolated from the DIS region using the Wandzura-Wilczek prediction [39].

Figure 5.1 to 5.8 show the distribution of deuteron spin asymmetry $A_{\|}$ derived from EG4 experimental data in different Q^2 bins compared with the spin asymmetry constructed from A_1 and A_2 from nucleon spin structure models. The latter is expressed in red line points.

We can see from these figures a clear structure at the elastic peak which occurs around the value of proton mass, $W \sim 0.9382GeV$. The asymmetry is negative for the Δ resonance ($\Delta(1232)P_{33}$), which is expected for A_1 for a pure magnetic dipole transition to the Δ resonance. As the value W increases, the asymmetry is closer to zero. At larger Q^2, the asymmetry at high W are positive, indicating that the amplitude corresponding to the absorption cross section $\sigma^T_{1/2}$ is the dominant one. The asymmetry at higher resonance regions ($N(1440)P_{11}$ at $W = 1.44GeV$, $N(1520)D_{13}$ at $W = 1.52GeV$ and $N(1535)S_{11}$ at $W = 1.535GeV$) shows only a little change with increasing Q^2. The data agrees with the prediction quite well.

Figure 5.9 shows the result of deuteron target first moment from the Eg1 experiment in comparison with the models mentioned in Chapter 1 and result from the SLAC experiment [41]. We can see that below the $Q^2 \approx 2GeV^2$ region, the data show a very strong Q^2 dependence. The integral is negative below $Q^2 \approx 0.5GeV^2$. which is due to the dominance of the $A_{3/2}$ amplitude at lower Q^2 values. At larger Q^2 $A_{1/2}$ becomes the dominant amplitude and the integral becomes positive as the negative contribution due to the Δ resonance starts to diminish. We can also clearly see the trend towards the GDH slope at low Q^2.

Further error analysis includes radiative correction, nuclear correction, pair-symmetric

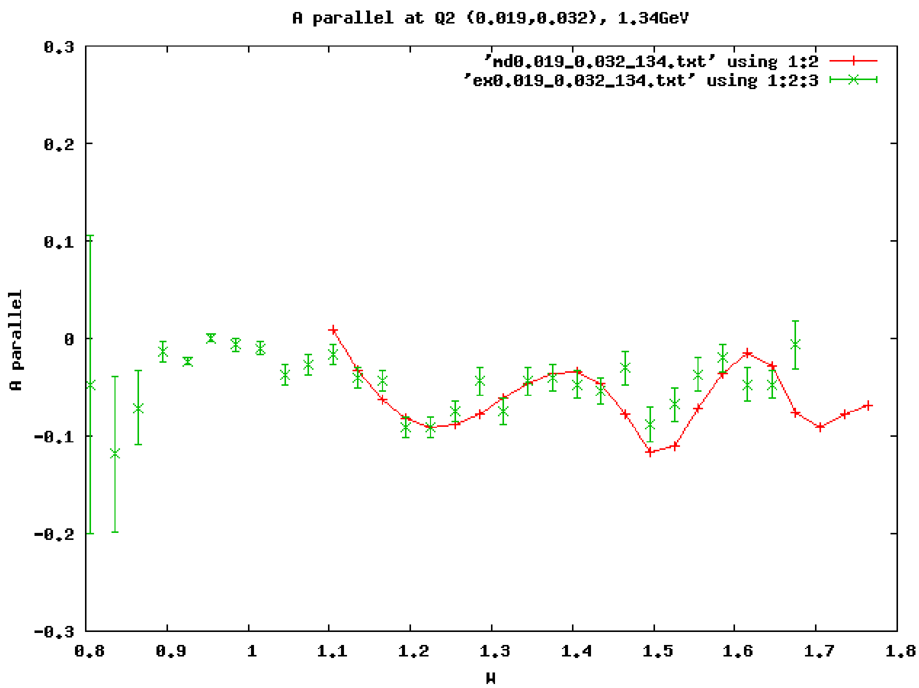

Figure 5.1: $A_{\parallel}$ vs W at Q^2 = (0.019,0.032), E_{in} = 1.34 GeV. The red line is $A_{parallel}$ constructed from spin structure functions and the green dots are ND_3 spin asymmetry extracted from experimental data.

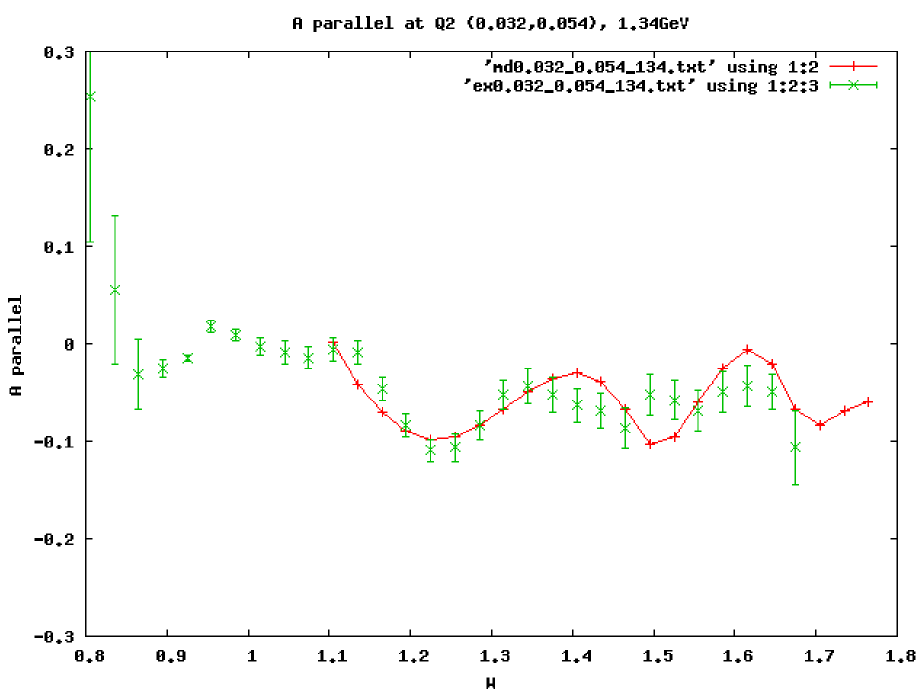

Figure 5.2: $A_{\parallel}$ vs W at Q^2 = (0.032,0.054), E_{in} = 1.34 GeV. The red line is $A_{parallel}$ constructed from spin structure functions and the green dots are ND_3 spin asymmetry extracted from experimental data.

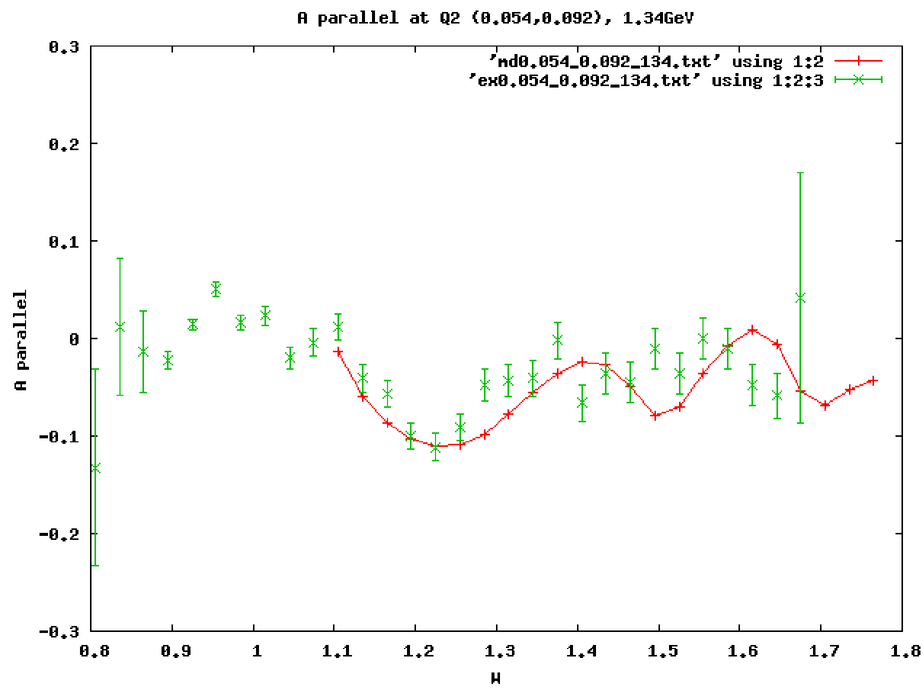

Figure 5.3: $A_{\|}$ vs W at Q^2 = (0.054,0.092), E_{in} = 1.34 GeV. The red line is $A_{parallel}$ constructed from spin structure functions and the green dots are ND_3 spin asymmetry extracted from experimental data.

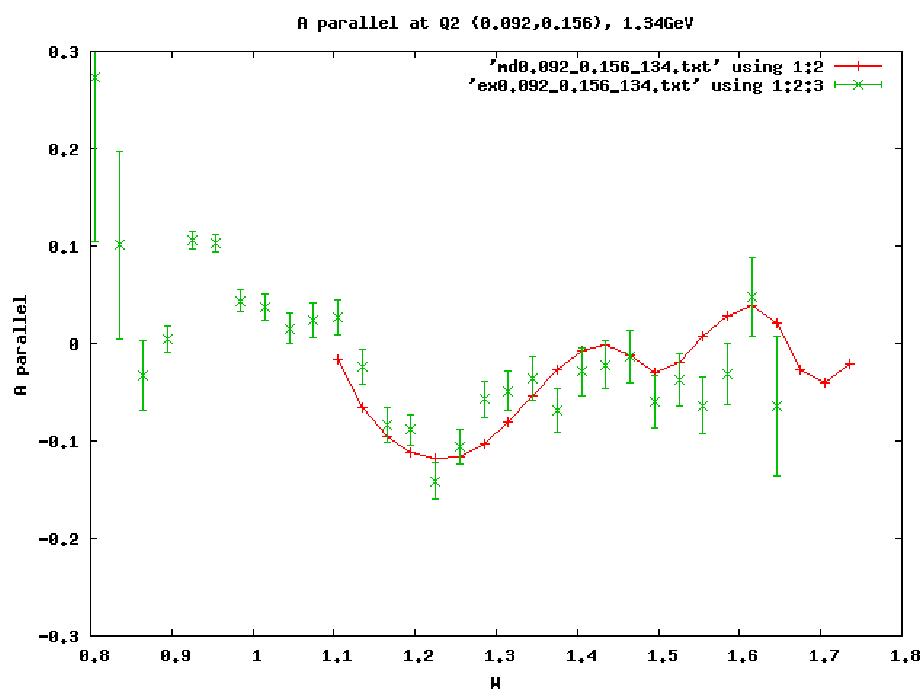

Figure 5.4: $A_{\|}$ vs W at Q^2 = (0.092,0.156), E_{in} = 1.34 GeV. The red line is $A_{parallel}$ constructed from spin structure functions and the green dots are ND_3 spin asymmetry extracted from experimental data.

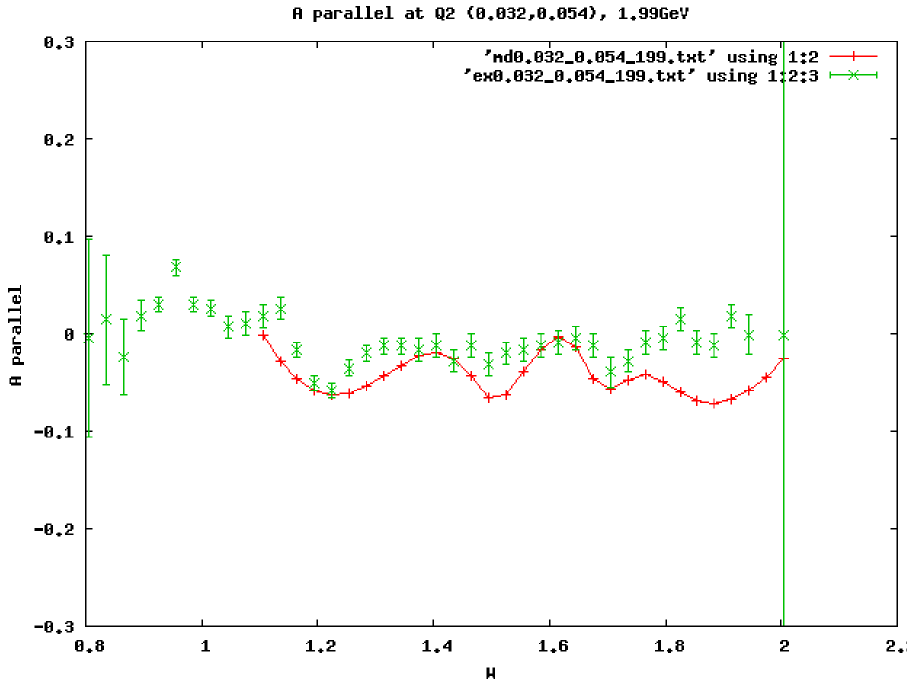

Figure 5.5: $A_{\|}$ vs W at $Q^2 = (0.032{,}0.054)$, $E_{in} = 1.99$ GeV. The red line is $A_{parallel}$ constructed from spin structure functions and the green dots are ND_3 spin asymmetry extracted from experimental data.

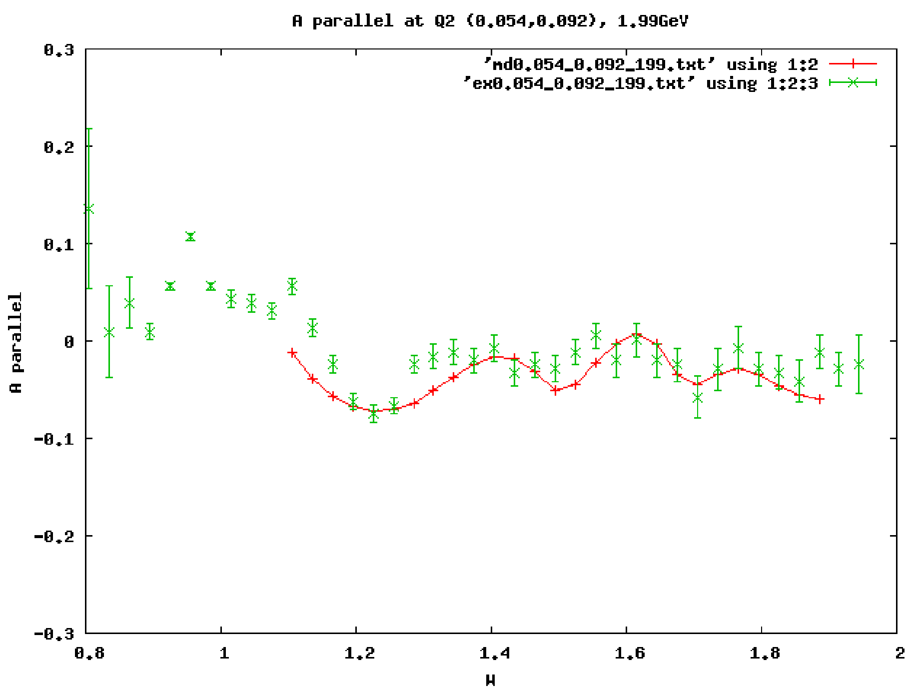

Figure 5.6: $A_{\|}$ vs W at $Q^2 = (0.054{,}0.092)$, $E_{in} = 1.99$ GeV. The red line is $A_{parallel}$ constructed from spin structure functions and the green dots are ND_3 spin asymmetry extracted from experimental data.

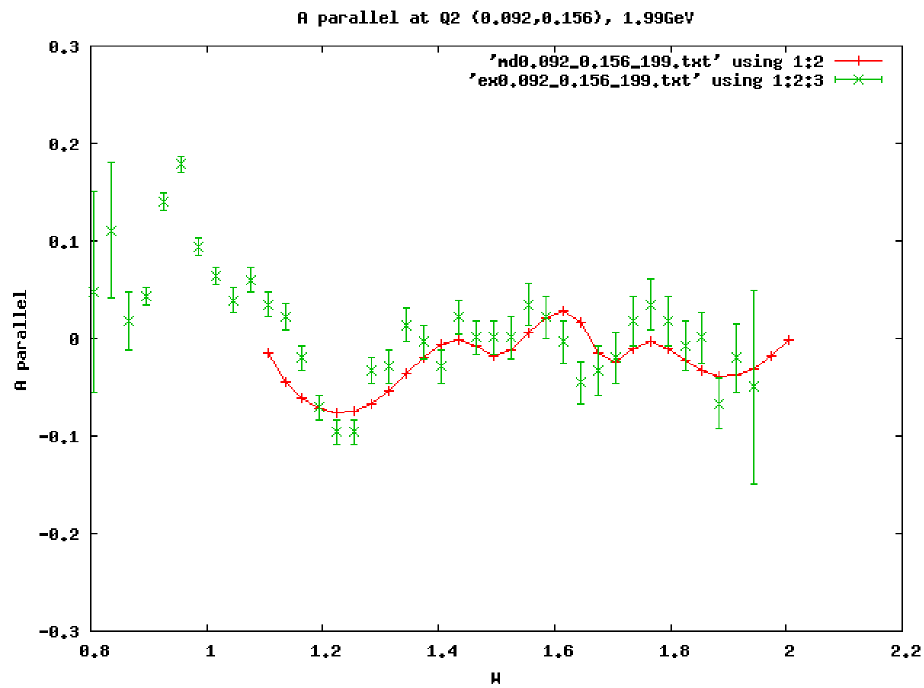

Figure 5.7: $A_{\parallel}$ vs W at Q^2 = (0.092,0.156), E_{in} = 1.99 GeV. The red line is $A_{parallel}$ constructed from spin structure functions and the green dots are ND_3 spin asymmetry extracted from experimental data.

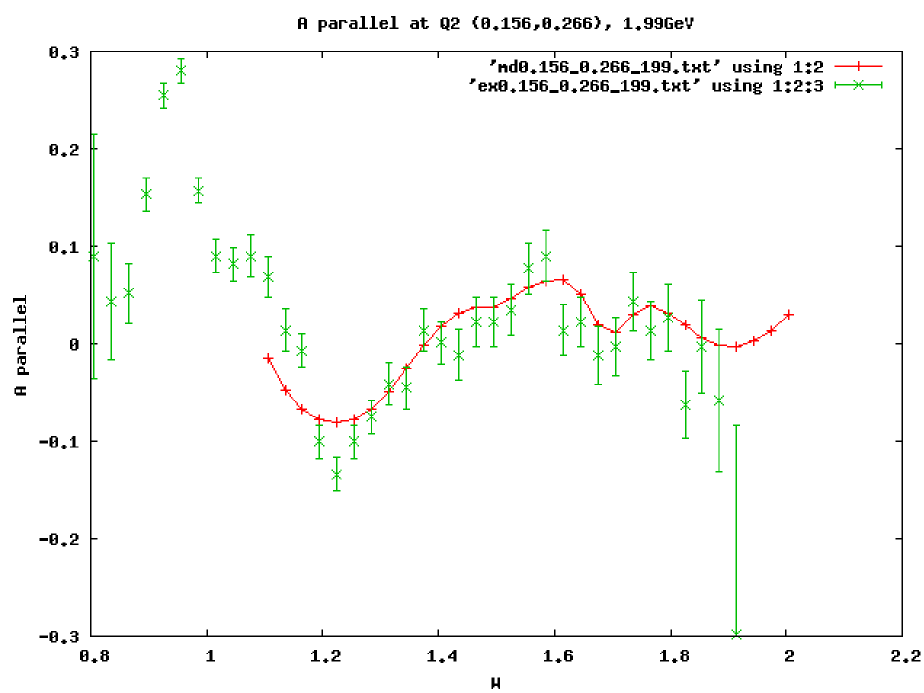

Figure 5.8: $A_{\parallel}$ vs W at Q^2 = (0.156,0.266), E_{in} = 1.99 GeV. The red line is $A_{parallel}$ constructed from spin structure functions and the green dots are ND_3 spin asymmetry extracted from experimental data.

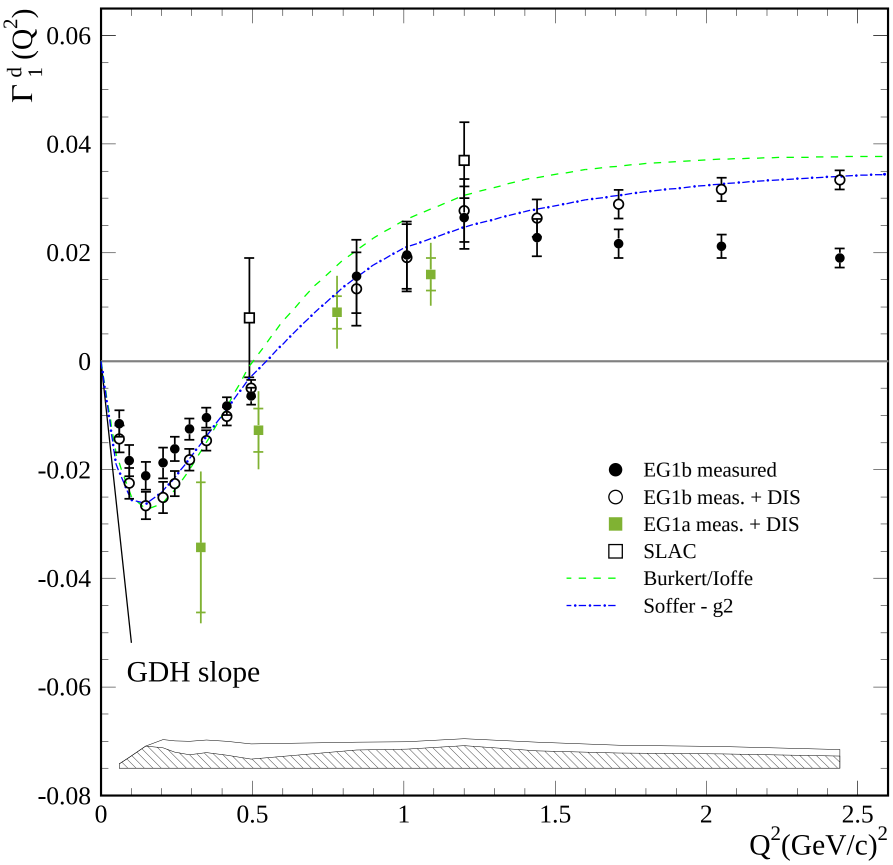

Figure 5.9: Comparison of the Eg1 Γ_1 to various models [5, 40, 39, 13] by Vipuli [41]. The error bars show statistical uncertainties. The shaded region and the line above the shaded region at the bottom of the plot indicate the systematic uncertainties for the measured points and for the integral respectively.

correction and the study of pion contamination. A more detailed systematic error for the electron scattering asymmetry will be constructed based on these analysis.

Future data analysis on the spin structure function $g_1^d(x, Q^2)$ can be developed from the longitudinal asymmetry as shown in this equation:

$$g_1 = \frac{F_1}{1+\gamma^2}[A_{\parallel}/D + (\gamma - \eta)A_2] \tag{5.0.1}$$

where $\eta = \frac{Q}{\nu}$, $A_{\parallel}$ is the longitudinal asymmetry. In general, g_1^d evolves logarithmically with Q^2, and is expected to grow with Q^2 at low x and decrease with Q^2 at high x. This pattern is also predicted and observed for the spin-averaged structure function $F_1(x, Q^2)$.

The first moment can be evaluated by integrating the structure function $g_1(x, Q^2)$ over the entire range of x:

$$\Gamma_1^d(Q^2) = \int_0^1 g_1^d(x, Q^2)dx \tag{5.0.2}$$

The analysis of Γ_1^d at low Q^2 serves as key to the measurement of the GDH slope. The results will put stringent constraints on different approaches in Chiral Perturbation Theory, and provide the data for an improved understanding of hadronic spin processes in the domain of confinement.

Chapter 6

Appendix

The following tables are a collection of run information. The first column is the run index, "1" represents good runs. The third column is the target index number, in which 2 =long ND_3, 3=empty cup, 4= long C, 6=short C, 7= long C no He, 8=empty cup.

index	run number	target	$E_in(GeV)$	Torrus current	P_t	P_{beam}
1	51587	2	2.000	-2250	0.00	86.9
1	51588	2	2.000	-2250	0.00	86.9
1	51589	2	2.000	-2250	0.00	86.9
1	51590	2	2.000	-2250	0.00	86.9
1	51591	2	2.000	-2250	0.00	86.9
1	51592	2	2.000	-2250	0.00	86.9
1	51593	2	2.000	-2250	0.00	-86.9
1	51594	2	2.000	-2250	0.00	-86.9
1	51595	2	2.000	-2250	17.1	-86.9
1	51596	2	2.000	-2250	23.2	-86.9
1	51597	2	2.000	-2250	24.3	-86.9
1	51598	2	2.000	-2250	23.1	-86.9
1	51599	2	2.000	-2250	23.4	-86.9
1	51600	4	2.000	-2250	0.00	-86.9
1	51601	4	2.000	-2250	0.00	86.9
1	51602	2	2.000	-2250	21.3	86.9
1	51603	2	2.000	-2250	21.4	86.9
1	51604	2	2.000	-2250	22.6	86.9
1	51605	2	2.000	-2250	21.9	86.9
1	51606	2	2.000	-2250	21.6	86.9
1	51608	2	2.000	-2250	22.0	86.9
1	51609	2	2.000	-2250	18.6	-86.9
1	51610	2	2.000	-2250	20.8	-86.9
1	51611	2	2.000	-2250	21.9	-86.9
1	51615	2	2.000	-2250	14.6	-86.9
1	51616	2	2.000	-2250	17.4	-86.9
1	51617	2	2.000	-2250	22.0	-86.9
1	51618	2	2.000	-2250	23.3	-86.9
1	51619	2	2.000	-2250	25.0	-86.9
1	51620	2	2.000	-2250	24.8	86.9
1	51621	2	2.000	-2250	23.9	86.9
1	51622	2	2.000	-2250	24.6	86.9
1	51623	2	2.000	-2250	25.7	86.9
1	51624	2	2.000	-2250	24.8	86.9
1	51625	2	2.000	-2250	24.0	86.9
1	51626	2	2.000	-2250	24.0	86.9
1	51627	3	2.000	-2250	0.00	86.9
1	51628	4	2.000	-2250	0.00	86.9

index	run number	target	$E_i n(GeV)$	Torrus current	P_t	P_{beam}
1	51629	2	2.000	-2250	22.1	86.9
1	51630	2	2.000	-2250	23.6	86.9
1	51631	2	2.000	-2250	23.0	86.9
1	51632	2	2.000	-2250	23.0	-86.9
1	51633	2	2.000	-2250	23.1	-86.9
1	51634	2	2.000	-2250	23.4	-86.9
1	51635	2	2.000	-2250	22.8	-86.9
1	51636	2	2.000	-2250	22.5	-86.9
1	51637	2	2.000	-2250	22.2	-86.9
1	51638	2	2.000	-2250	23.1	-86.9
1	51639	2	2.000	-2250	25.8	-86.9
1	51640	2	2.000	-2250	25.0	-86.9
1	51641	2	2.000	-2250	25.2	86.9
1	51642	2	2.000	-2250	24.5	86.9
1	51643	2	2.000	-2250	24.3	86.9
1	51645	2	2.000	-2250	0.00	86.9
1	51646	2	2.000	-2250	24.9	86.9
1	51647	2	2.000	-2250	24.1	86.9
1	51648	2	2.000	-2250	24.5	86.9
1	51649	2	2.000	-2250	24.2	86.9
1	51650	2	2.000	-2250	24.4	86.9
1	51652	2	2.000	-2250	24.0	86.9
1	51653	2	2.000	-2250	23.6	86.9
1	51654	2	2.000	-2250	23.8	86.9
1	51655	2	2.000	-2250	24.1	-86.9
1	51656	2	2.000	-2250	23.2	-86.9
1	51657	2	2.000	-2250	23.8	-86.9
1	51658	2	2.000	-2250	0.00	-86.9
1	51659	2	2.000	-2250	22.4	-86.9
1	51660	2	2.000	-2250	22.6	-86.9
1	51661	2	2.000	-2250	23.9	-86.9
1	51662	2	2.000	-2250	23.0	-86.9
1	51663	2	2.000	-2250	23.0	-86.9
1	51664	2	2.000	-2250	23.9	-86.9
1	51665	2	2.000	-2250	23.7	-86.9

index	run number	target	$E_in(GeV)$	Torrus current	P_t	P_{beam}
1	51666	2	2	-2250	23.2	86.9
1	51667	2	2	-2250	23.9	86.9
1	51668	2	2	-2250	24.3	86.9
1	51669	2	2	-2250	23.8	86.9
1	51670	2	2	-2250	23.3	86.9
1	51671	2	2	-2250	0	86.9
1	51673	2	2	-2250	23.7	86.9
1	51675	2	2	-2250	22.8	86.9
1	51676	2	2	-2250	22	86.9
1	51677	2	2	-2250	23.5	86.9
1	51678	2	2	-2250	0	86.9
1	51679	2	2	-2250	23	86.9
1	51680	2	2	-2250	22.5	86.9
1	51681	2	2	-2250	22.4	86.9
1	51696	2	2	-2250	0	-85.5
1	51697	2	2	-2250	0	-85.5
1	51698	2	2	-2250	0	-85.5
1	51699	2	2	-2250	0	-85.5
1	51700	2	2	-2250	0	-85.5
1	51702	2	2	-2250	0	-85.5
1	51703	2	2	-2250	0	-85.5
1	51704	2	2	-2250	0	-85.5
1	51705	2	2	-2250	29.9	-85.5
1	51706	2	2	-2250	27.3	-85.5
1	51707	2	2	-2250	25.7	-85.5
1	51708	2	2	-2250	26.6	-85.5
1	51709	2	2	-2250	26.1	-85.5
1	51710	2	2	-2250	26.1	-85.5
1	51711	2	2	-2250	25.4	-85.5
1	51712	2	2	-2250	25.1	-85.5
1	51713	2	2	-2250	25.3	-85.5
1	51714	2	2	-2250	25	-85.5
1	51716	3	2	-2250	0	-85.5
1	51717	4	2	-2250	0	-85.5
1	51718	2	2	-2250	24.3	-85.5
1	51719	2	2	-2250	24.1	85.5
1	51720	2	2	-2250	24.2	85.5

index	run number	target	$E_in(GeV)$	Torrus current	P_t	P_{beam}
1	51721	2	2	-2250	22.2	85.5
1	51722	2	2	-2250	23.6	85.5
1	51723	2	2	-2250	23.5	85.5
1	51724	2	2	-2250	24.1	85.5
1	51725	2	2	-2250	23.5	85.5
1	51726	2	2	-2250	23.1	85.5
1	51727	2	2	-2250	23.9	85.5
1	51728	2	2	-2250	24.6	85.5
1	51729	2	2	-2250	22.9	85.5
1	51730	2	2	-2250	23.5	85.5
1	51731	2	2	-2250	21.3	85.5
1	51732	2	2	-2250	19.7	85.5
1	51734	2	2	-2250	20	85.5
1	51735	2	2	-2250	21.5	85.5
1	51736	2	2	-2250	20.2	85.5
1	51737	2	2	-2250	21.2	-85.5
1	51738	2	2	-2250	22.4	-85.5
1	51739	2	2	-2250	23.7	-85.5
1	51740	2	2	-2250	24	-85.5
1	51741	2	2	-2250	23.7	-85.5
1	51742	2	2	-2250	23.9	-85.5
1	51743	2	2	-2250	23.5	-85.5
1	51744	2	2	-2250	24	-85.5
1	51745	2	2	-2250	23.8	-85.5
1	51746	2	2	-2250	0	-85.5
1	51747	2	2	-2250	0	-85.5
1	51748	2	2	-2250	23.6	-85.5
1	51749	2	2	-2250	23.6	-85.5
1	51750	2	2	-2250	23.4	-85.5
1	51751	2	2	-2250	23.3	-85.5
1	51752	2	2	-2250	22.6	85.5
1	51753	2	2	-2250	22.6	85.5
1	51754	2	2	-2250	0	85.5
1	51755	2	2	-2250	0	85.5
1	51756	2	2	-2250	22.6	85.5
1	51757	2	2	-2250	22.6	85.5
1	51758	2	2	-2250	22.6	85.5
1	51760	2	2	-2250	22.9	85.5

index	run number	target	$E_in(GeV)$	Torrus current	P_t	P_{beam}
1	51761	2	2	-2250	22.1	85.5
1	51762	2	2	-2250	22.2	85.5
1	51763	2	2	-2250	22.9	85.5
1	51764	2	2	-2250	21.8	85.5
1	51765	2	2	-2250	22.1	85.5
1	51766	2	2	-2250	21.7	85.5
1	51767	2	2	-2250	21.1	85.5
1	51768	2	2	-2250	21.8	85.5
1	51770	2	2	-2250	23.6	85.5
1	51771	2	2	-2250	24.5	85.5
1	51772	2	2	-2250	23.6	-85.5
1	51773	2	2	-2250	23.2	-85.5
1	51774	2	2	-2250	23.2	-85.5
1	51775	2	2	-2250	23.9	-85.5
1	51776	2	2	-2250	24.1	-85.5
1	51777	2	2	-2250	25.1	-85.5
1	51778	2	2	-2250	24.5	-85.5
1	51779	2	2	-2250	0	-85.5
1	51780	2	2	-2250	0	-85.5
1	51781	2	2	-2250	0	-85.5
1	51782	2	2	-2250	0	-85.5
1	51783	2	2	-2250	0	-85.5
1	51784	2	2	-2250	0	-85.5
1	51785	2	2	-2250	0	-85.5
1	51787	2	2	-2250	22.2	85.5
1	51788	2	2	-2250	24.1	85.5
1	51789	2	2	-2250	22.5	85.5
1	51790	2	2	-2250	23	85.5
1	51794	7	2	-2250	0	-87.6
1	51796	4	2	-2250	0	-87.6
1	51799	2	2	-2250	35.3	-87.6
1	51800	2	2	-2250	35.5	-87.6
1	51801	2	2	-2250	37.1	-87.6
1	51802	2	2	-2250	37.3	-87.6
1	51803	2	2	-2250	36.1	-87.6
1	51804	2	2	-2250	36.2	-87.6
1	51805	2	2	-2250	37.6	-87.6
1	51806	2	2	-2250	40.1	-87.6
1	51807	2	2	-2250	35.8	87.6
1	51808	2	2	-2250	0	87.6

index	run number	target	$E_in(GeV)$	Torrus current	P_t	P_{beam}
1	51810	2	2	-2250	36.6	87.6
1	51811	2	2	-2250	36.2	87.6
1	51812	2	2	-2250	35.6	87.6
1	51813	2	2	-2250	35.2	87.6
1	51814	2	2	-2250	35.4	87.6
1	51815	2	2	-2250	34.2	87.6
1	51816	2	2	-2250	33.8	87.6
1	51817	2	2	-2250	34.5	87.6
1	51818	2	2	-2250	32.1	87.6
1	51819	2	2	-2250	30.1	87.6
1	51820	2	2	-2250	31.3	-87.6
1	51821	2	2	-2250	32.7	-87.6
1	51822	2	2	-2250	34.2	-87.6
1	51823	2	2	-2250	34.5	-87.6
1	51824	2	2	-2250	0	-87.6
1	51825	2	2	-2250	34	-87.6
1	51826	2	2	-2250	0	-87.6
1	51827	2	2	-2250	0	-87.6
1	51828	2	2	-2250	33.3	-87.6
1	51829	2	2	-2250	36.9	-87.6
1	51830	2	2	-2250	39.6	-87.6
1	51831	2	2	-2250	39.9	87.6
1	51832	2	2	-2250	38.4	87.6
1	51833	2	2	-2250	38.6	87.6
1	51834	2	2	-2250	38.3	87.6
1	51835	2	2	-2250	39.9	87.6
1	51836	2	2	-2250	38.3	87.6
1	51837	2	2	-2250	40.1	87.6
1	51838	2	2	-2250	39.7	87.6
1	51839	2	2	-2250	38.6	87.6
1	51840	2	2	-2250	39.2	87.6
1	51841	2	2	-2250	0	87.6
1	51842	2	2	-2250	26.4	-87.6
1	51843	2	2	-2250	39.3	-87.6
1	51844	2	2	-2250	39.2	-87.6
1	51845	2	2	-2250	39.7	-87.6
1	51847	2	2	-2250	38.7	-87.6

index	run number	target	$E_in(GeV)$	Torrus current	P_t	P_{beam}
1	51848	2	2	-2250	39.3	-87.6
1	51849	2	2	-2250	38.5	-87.6
1	51850	2	2	-2250	38.5	-87.6
1	51851	2	2	-2250	39	-87.6
1	51852	2	2	-2250	39.2	-87.6
1	51853	2	2	-2250	38.1	-87.6
1	51854	2	2	-2250	37.6	-87.6
1	51855	2	2	-2250	38.6	-87.6
1	51856	2	2	-2250	38	87.6
1	51857	2	2	-2250	0	87.6
1	51858	2	2	-2250	24.8	87.6
1	51859	2	2	-2250	38.3	87.6
1	51860	2	2	-2250	37.5	87.6
1	51861	2	2	-2250	38.8	87.6
1	51862	2	2	-2250	37.4	87.6
1	51863	2	2	-2250	38.3	87.6
1	51864	2	2	-2250	37.6	87.6
1	51865	2	2	-2250	37.9	87.6
1	51866	2	2	-2250	36.6	87.6
1	51867	2	2	-2250	0	87.6
1	51868	4	2	-2250	0	87.6
1	51869	3	2	-2250	0	87.6
1	51870	4	2	-2250	0	87.6
1	51887	7	1.34	-1500	0	-68.2
1	51889	4	1.34	-1500	0	-68.2
1	51890	3	1.34	-1500	0	-68.2
1	51896	2	1.34	-1500	44.2	-68.2
1	51897	2	1.34	-1500	43.8	-68.2
1	51898	2	1.34	-1500	44.6	-68.2
1	51899	2	1.34	-1500	45.6	-68.2
1	51900	2	1.34	-1500	45.1	-68.2
1	51906	2	1.34	-1500	45.3	-68.2
1	51907	2	1.34	-1500	45.1	-68.2
1	51908	2	1.34	-1500	45.5	-68.2
1	51909	2	1.34	-1500	0	-68.2

index	run number	target	$E_in(GeV)$	Torrus current	P_t	P_{beam}
1	51911	2	1.34	-1500	42.8	-68.2
1	51913	2	1.34	-1500	43.4	-68.2
1	51915	2	1.34	-1500	42.9	-68.2
1	51916	2	1.34	-1500	43	-68.2
1	51917	2	1.34	-1500	42.1	-68.2
1	51918	2	1.34	-1500	43.1	-68.2
1	51919	2	1.34	-1500	39.4	-68.2
1	51920	2	1.34	-1500	41.6	-68.2
1	51921	2	1.34	-1500	43.2	-68.2
1	51922	2	1.34	-1500	42.4	-68.2
1	51928	2	1.34	-1500	41.7	-68.2
1	51930	2	1.34	-1500	41.9	-68.2
1	51931	2	1.34	-1500	42	-68.2
1	51932	2	1.34	-1500	0	-68.2
1	51933	2	1.34	-1500	0	-68.2
1	51934	2	1.34	-1500	0	-68.2
1	51935	2	1.34	-1500	0	-68.2
1	51936	2	1.34	-1500	0	-68.2
1	51938	2	1.34	-1500	42.6	-68.2
1	51939	2	1.34	-1500	42.2	-68.2
1	51940	2	1.34	-1500	41.2	-68.2
1	51941	2	1.34	-1500	41.7	-68.2
1	51942	2	1.34	-1500	43.7	-68.2
1	51943	2	1.34	-1500	41.8	-68.2
1	51944	2	1.34	-1500	42.2	-68.2
1	51945	2	1.34	-1500	41.5	-68.2
1	51946	2	1.34	-1500	42.1	-68.2
1	51947	2	1.34	-1500	41.7	-68.2
1	51948	2	1.34	-1500	40.5	-68.2
1	51949	2	1.34	-1500	0	68.2
1	51950	2	1.34	-1500	39	68.2
1	51951	2	1.34	-1500	40.5	68.2
1	51952	2	1.34	-1500	38.8	68.2
1	51953	2	1.34	-1500	38.9	68.2
1	51954	2	1.34	-1500	41.6	68.2
1	51957	4	1.34	-1500	0	68.2
1	51958	6	1.34	-1500	0	68.2
1	51959	2	1.34	-1500	38.2	68.2
1	51960	2	1.34	-1500	43.2	68.2
1	51961	2	1.34	-1500	45.1	68.2

index	run number	target	$E_i n(GeV)$	Torrus current	P_t	P_{beam}
1	51964	2	1.34	-1500	45	68.2
1	51965	2	1.34	-1500	45.7	68.2
1	51967	2	1.34	-1500	45.2	-68.2
1	51968	2	1.34	-1500	45.5	-68.2
1	51969	2	1.34	-1500	45.2	-68.2
1	51970	2	1.34	-1500	45.4	-68.2
1	51971	2	1.34	-1500	44.1	-68.2
1	51973	2	1.34	-1500	44.7	-68.2
1	51974	2	1.34	-1500	44.1	-68.2
1	51975	2	1.34	-1500	43.8	68.2
1	51976	2	1.34	-1500	43.3	68.2
1	51977	2	1.34	-1500	42.2	68.2
1	51978	2	1.34	-1500	42.7	68.2
1	51979	2	1.34	-1500	0	68.2
1	51980	2	1.34	-1500	41.3	68.2
1	52033	2	1.34	-1500	43.1	68.2
1	52034	2	1.34	-1500	42.4	68.2
1	52035	2	1.34	-1500	41.5	68.2
1	52036	2	1.34	-1500	42.4	68.2
1	52037	2	1.34	-1500	42.2	68.2
1	52038	2	1.34	-1500	41	68.2
1	52039	2	1.34	-1500	42.1	68.2
1	52040	2	1.34	-1500	43.1	68.2

Bibliography

[1] W. Greiner and A. Schafer. *Quantum Chromodynamics*. Springer, 1994.

[2] R. P. Feynman. Partons. Prepared for symposium on the past decade in Particle Theory, Austin, Tex., 14-17 Apr 1970.

[3] John R. Ellis and Robert L. Jaffe. A sum rule for deep inelastic electroproduction from polarized protons. *Phys. Rev.*, D9:1444, 1974.

[4] Elliot Leader and Mauro Anselmino. A crisis in the parton model: Where, oh where is the proton's spin? *Z. Phys.*, C41:239, 1988.

[5] J. Ashman and others [EMC Collaboration]. An investigation of the spin structure of the proton in deep inelastic scattering of polarized muons on polarized protons. *Nucl. Phys.*, B328:1, 1989.

[6] M. J. Alguard et al. Deep inelastic e p asymmetry measurements and comparison with the Bjorken Sum Rule and models of the proton spin structure. *Phys. Rev. Lett.*, 41:70, 1978.

[7] S. D. Drell and Anthony C. Hearn. Exact sum rule for nucleon magnetic moments. *Phys. Rev. Lett.*, 16:908–911, 1966.

[8] M. Anselmino, A. Efremov, and E. Leader. The theory and phenomenology of polarized deep inelastic scattering. *Phys. Rept.*, 261:1–124, 1995.

[9] Guenter Baum and others [SLAC E130 Collaboration]. A new measurement of deep inelastic e p asymmetries. *Phys. Rev. Lett.*, 51:1135, 1983.

[10] K. Abe and others [E143 Collaboration]. Measurements of the proton and deuteron spin structure functions g_1 and g_2. *Phys. Rev.*, D58:112003, 1998.

[11] P. L. Anthony and others [E155 Collaboration]. Measurement of the deuteron spin structure function $g_1^d(x)$ for $1(GeV/c)^2 < Q^2 < 40(GeV/c)^2$. *Phys. Lett.*, B463:339–345, 1999.

[12] B.W.Filippone and X. Ji. *Adv.Nucl.Phys.*, 26:1, 2001.

[13] S. E. Kuhn, J. P. Chen, and E. Leader. Spin Structure of the Nucleon - Status and Recent Results. *Prog. Part. Nucl. Phys.*, 63:1–50, 2009.

[14] S. A. Larin and J. A. M. Vermaseren. The α_s^3 corrections to the Bjorken Sum Rule for polarized electroproduction and to the Gross-Llewellyn Smith Sum Rule. *Phys. Lett.*, B259:345–352, 1991.

[15] Anthony William Thomas and Wolfram Weise. The Structure of the Nucleon. Berlin, Germany: Wiley-VCH (2001) 389 p.

[16] S. B. Gerasimov. A sum rule for magnetic moments and the damping of the nucleon magnetic moment in nuclei. *Sov. J. Nucl. Phys.*, 2:430–433, 1966.

[17] D. Drechsel, S. S. Kamalov, and L. Tiator. The GDH Sum Rule and related integrals. *Phys. Rev.*, D63:114010, 2001.

[18] V. D. Burkert and B. L. Ioffe. On the Q^2 variation of spin dependent deep inelastic electron - proton scattering. *Phys. Lett.*, B296:223–226, 1992.

[19] Jacques Soffer and O. V. Teryaev. On the g_2 manifestation for longitudinally polarized particles. *Phys. Rev.*, D51:25–31, 1995.

[20] Y.Prok. Measurement of the spin structure function $g_1(x, q^2)$ of the proton measured in the resonance region. *Ph.D. diss., University of Virginia*, 2004.

[21] H.A.Grunder. The Continuous Electron Beam Accelerator Facility, CEBAF-PR-87-017, 1987.

[22] I.Kominis. Measurement of the Neutron (^3He) Spin Structure at low Q^2 and the Extended GDH Sum Rule. *Ph.D. diss. Princeton University*, 2001.

[23] M. Steigerward. MeV Mott polarimetry at Jefferson Lab. *Kyoto Japan 14th International Spin Physics Symposium, AIP Conference Proceedings 570, 945, Melville, NewYork*. Eds: Hatanaka, Nakano, Imai, Ejiri, 2001.

[24] C.K. Sinclair. Electron beam polarimetry. TJNAF Report, JLAB-ACC-98-04, 1998.

[25] S. Goertz, W. Meyer, and G. Reicherz. Polarized H, D and ^3He targets for particle physics experiments. *Prog. Part. Nucl. Phys.*, 49:403–489, 2002.

[26] D. G. Crabb. Deuteron and proton polarizations in irradiated materials. Prepared for 3rd International Symposium on the Gerasimov- Drell-Hearn Sum Rule and its Extensions (GDH 2004), Norfolk, Virginia, 2-5 Jun 2004.

[27] S. Goertz. Polarized solid targets and techniques. Proceedings, 9th International Workshop, Bad Honnef, Germany: October, 2003. *Nucl. Instr and Meth. in Phys. Res.*, A526, 2004.

[28] Abragram. Principles of nuclear magnetism. *Cleradon Press, Oxford*, 1961.

[29] J.D.Jackson. *Classical Electrodynamics*. 1975.

[30] W. de Boer. Dynamic orientation of nuclei at low temperatures, CERN Yellow Report 74-11 (1974). *J. of Low-Temp. Phys.*, 22,185, 1976.

[31] W. Kielhorn. A technique for measurement of vector and tensor polarization in solid spin one polarized targets. Los Alamos National Lab. Report LA-12116-T, 1991.

[32] M.H.Cohen and F. Reif. Nuclear quadrupole effects in solids. *Solid State Physics, Academic Inc., NewYork*, 1957.

[33] J. Pumplin et al. New generation of parton distributions with uncertainties from global QCD analysis. *JHEP*, 07:012, 2002.

[34] D. G. Crabb et al. Observation of a 96-percent proton polarization in irradiated ammonia. *Phys. Rev. Lett.*, 64:2627–2629, 1990.

[35] B. A. Mecking et al. The CEBAF Large Acceptance Spectrometer (CLAS). *Nucl. Instrum. Meth.*, A503:513–553, 2003.

[36] M. Amarian et al. The CLAS forward electromagnetic calorimeter. *Nucl. Instrum. Meth.*, A460:239–265, 2001.

[37] See link: *http://clasweb.jlab.org/rungroups/eg4/wiki/index.php/.*

[38] C. Dulya et al. A line-shape analysis for spin-1 NMR signals. *Nuclear Instruments and Methods in Physics Research*, A398, 1997.

[39] S. Wandzura and Frank Wilczek. Sum rules for spin dependent electroproduction: Test of relativistic constituent quarks. *Phys. Lett.*, B72:195, 1977.

[40] B. Adeva and others [SMC Collaboration]. Spin asymmetries A_1 and structure functions g_1 of the proton and the deuteron from polarized high energy muon scattering. *Phys. Rev.*, D58:112001, 1998.

[41] K.G.Vipuli. Spin structure functions of the Deuteron measured with CLAS in and above the resonance region. *Ph.D. diss., Old Dominion University*, 1996.